

BOSTON UNIVERSITY  
GRADUATE SCHOOL OF ARTS AND SCIENCES

Dissertation

**A SEARCH FOR DINUCLEON DECAY INTO KAONS  
USING THE SUPER-KAMIOKANDE  
WATER CHERENKOV DETECTOR**

by

**MICHAEL D. LITOS**

B.S., Michigan State University, 2003

Submitted in partial fulfillment of the  
requirements for the degree of  
Doctor of Philosophy

2010

Approved by

First Reader

---

Edward T. Kearns, Ph.D.  
Professor of Physics

Second Reader

---

Martin Schmaltz, Ph.D.  
Associate Professor of Physics

# Acknowledgements

It has been a long and winding road to my PhD, and I certainly couldn't have made it all the way to the end without the support of my family, friends, and mentor figures.

First and foremost, I must thank the kind folks who made me in the first place: Thank you, Mom and Dad! You provided me with the opportunities that made it possible for me to even follow a path toward a PhD in the first place. Without your love and encouragement throughout my life, I would have never gotten this far.

Next, I must thank my siblings: Doug, Nick, Brian, Melody and Sarah. Especial thanks to Doug for always being there to put things in perspective with a little dose of the "Doog truth." It has been an indispensable tool for survival in graduate school and in life.

I want to thank my step-parents, Marta and Bill, who have been nothing but supportive of me throughout the years.

I'd like to thank my B.U. Super-K colleagues and the other fine folks who have shared workspace with me on the second floor of the PRB over the years: Jen Raaf, Dan Gastler, Fanny DuFour, Wei Wang, Scott Clark, Shantanu Desai, Scott Stackley, Claire Thomas, Brian Henning, Johnny Penwell, Aaron Herfurth, Betsy Dusingberre, Jason St. John, Hide Tomita, Luis Ibanez, Kevin Lynch, and Nigel Nation. You guys were always a big part of why I loved my job.

A huge thank you to all of the great friends I've made over the years here at B.U., who are simply too numerous to name, though they each and every one deserve far more than a simple listing in my acknowledgements section, anyway.

I want to thank my Super-K friends from other institutions: Maxim Fechner, Naho Tanimoto, Parker Cravens, Fumi Kato, Chris Regis, Ittoku Ikeda, Piotr Mijakowski, Chizue Ishihara, Josh Albert, Gaku Mitsuka, Ryan Terri, Shoei Nakayama, Eric Thrane, Yumiko Takenaga, Kevin Connolly, and Haruki Nishino.

Thank you to the top tier of the tireless custodial staff of the B.U. Physics Department: Maria and Bart, who always put a shine on our floors and a smile on our faces.

I want to thank Bob Kingsland in the B.U. machine shop, for teaching me the ways of the machine and for just being awesome.

Thanks to Eric Hazen, Chris Lawlor, and Paul Bohn of the B.U. Electronics Design Facility for helping me in the design and construction of the amazing VORTEX Monitor System.

Thanks to the fine B.U. Physics front office staff: First, Winna Somers for always dealing with my messed up travel reimbursement forms. And of course I must thank our own Wonder Woman incarnate, Mirtha Cabello, upon whom the operation of the entire Physics Department depends.

I would like to thank the terrific Super-K faculty for their guidance and tutelage throughout the years: Jim Stone, Takaaki Kajita, Larry Sulak, Masato Shiozawa, Hank Sobel, Kenji Kaneyuki, Kate Scholberg, Makoto Miura, Yoshinari Hayato, Shunichi Mine, and Yusuke Koshio.

A huge thanks to my thesis committee: Claudio Chamon, John Butler, Rob Carey, and especially Martin Schmaltz for helping me grapple with the theory behind my analysis.

I want to extend a special thanks to Chris Walter for mentoring me during my first few years as a graduate student and for all of the continued support throughout my time on Super-K.

I offer a very large thank you to my advisor, Ed Kearns, who has spent so much time, effort, money, and probably hair on my education over the past seven years. You are responsible for making me the scientist I am today, and for that I thank you.

Finally, I thank my eternal source of motivation and passion: Leah Angstman, my fiance and my best friend. I'd be aimless without you. And now that I'm a doctor, I promise I'll make an honest woman out of you!

Oh, and of course this entire thesis would simply be incomplete if I forgot to thank my best pal Roger Wendell... 's mom. Thanks, Mrs. Wendell!

**A SEARCH FOR DINUCLEON DECAY INTO KAONS  
USING THE SUPER-KAMIOKANDE  
WATER CHERENKOV DETECTOR**

(Order No.                   )

**MICHAEL LITOS**

Boston University Graduate School of Arts and Sciences, 2010

Major Professor: Edward T. Kearns, Professor of Physics

**ABSTRACT**

Dinucleon decay is the simultaneous decay of two nucleons bound within the same nucleus. This dissertation describes a search for dinucleon decay into kaons via  $^{16}\text{O}(pp) \rightarrow ^{14}\text{C} K^+ K^+$  using the first 91.7 kiloton · years of data collected by the Super-Kamiokande water Cherenkov detector. This is an interesting alternative to single proton decay because the process violates only baryon number, not lepton number; single proton decay violates both. In a supersymmetric framework, dinucleon decay into kaons is predicted to be the most sensitive experimental search that can probe the magnitude of the R-parity violating parameter  $\lambda''_{uds}$ .

The complex signature of the signal required the creation of several new event reconstruction techniques, including tools for fitting Cherenkov rings produced by charged kaons, a multiple vertex fitter for assigning a unique vertex to each ring, and a ring classification algorithm that incorporated the overall event topology. Another technique new to the Super-Kamiokande collaboration was the use of a boosted decision tree, which was utilized in the final stage of the analysis.

No signal event candidates were found in the data. Monte Carlo studies predicted a background of  $0.28 \pm 0.19$  events induced by atmospheric neutrino interactions, and a signal detection efficiency of  $12.6\% \pm 3.2\%$ . Based on these results, the first

experimental lower limit on the dinucleon partial lifetime for the decay mode  $pp \rightarrow K^+ K^+$  has been placed at  $1.7 \times 10^{32}$  years at 90% confidence level. This is about two orders of magnitude better than the only other dinucleon lifetime limits on record, made by the Frejus experiment, which include only decays with final state pions or leptons.

The lifetime limit may be interpreted as an upper limit of  $7.8 \times 10^{-9}$  on  $\lambda''_{uds}$ . This new experimental limit is more restrictive than the limit of  $\sim 10^{-7}$  estimated by J.L. Goity and M. Sher in their paper “Bounds on  $\Delta B = 1$  couplings in the supersymmetric standard model” (*Phys. Lett. B* **343**:1-2, 1995), which was based on typical nucleon and dinucleon lifetime limits of  $\sim 10^{30}$  years.

# Contents

Acknowledgements	iii
Abstract	vi
Table of Contents	viii
List of Tables	xiv
List of Figures	xvi
List of Abbreviations	xx
<b>1 Introduction</b>	<b>1</b>
<b>2 Motivation and Theory</b>	<b>6</b>
<b>3 Experimental Apparatus</b>	<b>14</b>
3.1 Super-Kamiokande Detector Overview . . . . .	14
3.2 Structure . . . . .	15
3.2.1 Inner Detector (ID) . . . . .	16
3.2.2 Outer Detector (OD) . . . . .	17
3.3 Cherenkov Radiation . . . . .	17

3.4	Photomultiplier Tubes . . . . .	21
3.4.1	Inner Detector Photomultiplier Tubes . . . . .	21
3.4.2	Outer Detector Photomultiplier Tubes . . . . .	23
3.5	Data Acquisition (DAQ) System . . . . .	24
3.5.1	Inner Detector DAQ . . . . .	24
3.5.2	Outer Detector DAQ . . . . .	27
3.5.3	Event Trigger System . . . . .	28
3.6	Water Purification System . . . . .	29
3.7	Calibration . . . . .	31
3.7.1	Relative Gain Calibration . . . . .	31
3.7.2	Absolute Gain Calibration . . . . .	32
3.7.3	Energy Scale Calibration . . . . .	33
3.7.4	Relative Timing Calibration . . . . .	36
3.7.5	Water Transparency Measurement . . . . .	38
<b>4</b>	<b>Atmospheric Neutrino Monte Carlo</b>	<b>44</b>
4.1	Atmospheric Neutrino Flux . . . . .	45
4.2	Neutrino Interactions . . . . .	46
4.2.1	Elastic and Quasi-Elastic Scattering . . . . .	47
4.2.2	Single Meson Production . . . . .	48
4.2.3	Coherent Pion Production . . . . .	50
4.2.4	Deep Inelastic Scattering . . . . .	50
4.3	Nuclear Effects . . . . .	52
4.4	Detector Simulation . . . . .	53
<b>5</b>	<b>Dinucleon Decay Monte Carlo</b>	<b>55</b>
5.1	Intra-Nuclear Simulation . . . . .	55

5.2	Extra-Nuclear Simulation . . . . .	58
<b>6</b>	<b>Data Reduction Process</b>	<b>60</b>
6.1	First Reduction . . . . .	60
6.2	Second Reduction . . . . .	61
6.3	Third Reduction . . . . .	62
6.3.1	Through-Going Muon Cut . . . . .	62
6.3.2	Stopping Muon Cut . . . . .	63
6.3.3	Cable Hole Muon Cut . . . . .	63
6.3.4	Flasher Cut . . . . .	64
6.3.5	Accidental Muon Cut . . . . .	64
6.3.6	Low Energy Muon Cut . . . . .	65
6.4	Fourth Reduction . . . . .	65
6.5	Fifth Reduction . . . . .	66
6.5.1	Final Stopping Muon Cut . . . . .	66
6.5.2	Invisible Muon Cut . . . . .	66
6.5.3	Final Accidental Muon Cut . . . . .	67
6.5.4	Long Tail Flasher Cut . . . . .	67
6.6	Final Reduced Data Sample . . . . .	68
<b>7</b>	<b>Physics Reconstruction</b>	<b>70</b>
7.1	Standard Reconstruction Algorithm . . . . .	70
7.1.1	Vertex Position and Ring Direction . . . . .	72
7.1.2	Ring Counting . . . . .	75
7.1.3	Showering Likelihood . . . . .	79
7.1.4	Ring Momentum . . . . .	84
7.1.5	Ring Number Correction . . . . .	88

7.1.6	Decay Electron Finding . . . . .	88
7.2	Multiple Vertex Fitter . . . . .	89
7.3	Reconstructed Ring Variables . . . . .	91
<b>8</b>	<b>Dinucleon Decay Signal</b>	<b>92</b>
8.1	Choice of Dinucleon Decay Mode . . . . .	92
8.2	Choice of Kaon Decay Modes . . . . .	94
8.3	Cherenkov Ring Combinations . . . . .	96
8.3.1	Ring Counting Inefficiencies . . . . .	96
8.3.2	True Particle Type Frequency . . . . .	98
8.3.3	Final List of Ring Combinations . . . . .	100
8.4	Signal Characteristics . . . . .	100
8.4.1	Multiple Vertices . . . . .	102
8.4.2	Kaon Rings . . . . .	103
8.4.3	Back-to-Back Kaons . . . . .	104
8.4.4	Features of Kaon Decay Modes . . . . .	104
<b>9</b>	<b>Dinucleon Decay Search</b>	<b>108</b>
9.1	Ring Classification . . . . .	109
9.1.1	Two Kaon Ring Classification . . . . .	111
9.1.2	Kaon Decay Product Ring Classification . . . . .	112
9.1.3	Pion Classification . . . . .	115
9.1.4	Low Gamma Momentum Correction . . . . .	116
9.1.5	Single Kaon Ring Classification . . . . .	117
9.2	Event Categorization . . . . .	119
9.3	Precuts . . . . .	120
9.4	Multi-Variate Analysis . . . . .	122

9.4.1	Input Variables . . . . .	125
9.4.2	Training and Testing of the Boosted Decision Tree . . . . .	139
9.4.3	Final Cut Placement for Boosted Decision Tree Output . . . . .	142
9.4.4	Boosted Decision Tree Monte Carlo Results . . . . .	144
9.4.5	Final Background Characteristics . . . . .	145
9.4.6	Final Signal Characteristics . . . . .	147
9.5	Systematic Uncertainties . . . . .	148
9.5.1	Monte Carlo Simulation Uncertainties . . . . .	149
9.5.2	Detector Related Uncertainties . . . . .	150
9.5.3	Reconstruction Uncertainties . . . . .	151
9.5.4	Search Method Uncertainties . . . . .	151
9.5.5	Total Systematic Uncertainty . . . . .	152
<b>10</b>	<b>Results and Conclusions</b>	<b>154</b>
<b>A</b>	<b>MVFIT Resolutions</b>	<b>157</b>
A.1	Charged Kaon Ring Resolutions . . . . .	159
A.2	Muon Ring Resolutions . . . . .	161
A.3	Gamma Ring Resolutions . . . . .	163
<b>B</b>	<b>Boosted Decision Tree</b>	<b>165</b>
B.1	Final Output . . . . .	166
B.2	Separation Index . . . . .	166
B.3	Adaptive Boost Method . . . . .	167
B.4	Pruning . . . . .	168
B.5	Training Distributions . . . . .	168
B.6	Variable Ranking . . . . .	171

<b>C Limit Calculations</b>	<b>174</b>
C.1 Lower Lifetime Limit on Decay Mode . . . . .	174
C.2 Upper Limit on $R$ -Parity Violating Parameter . . . . .	177
<b>Bibliography</b>	<b>180</b>
<b>Curriculum Vitae</b>	<b>185</b>

# List of Tables

3.1	Specifications for the 20-inch ID PMT [1]. . . . .	24
3.2	Specifications for the ATM module [1]. . . . .	25
4.1	Simulated physics processes. . . . .	54
6.1	Data reduction process event rates. . . . .	69
8.1	Dinucleon decay final state branching ratios. . . . .	94
8.2	Final state branching ratios for $^{16}\text{O}(pp) \rightarrow ^{14}\text{C} K^+ K^+$ . . . . .	95
8.3	Hadronic inefficiencies for $K^+$ detection. . . . .	95
8.4	Frequency of found ring count by final decay state. . . . .	97
8.5	True particle type frequency. . . . .	98
8.6	Ring combinations by true particle type. . . . .	99
9.1	Frequency of rings produced by kaons. . . . .	110
9.2	Frequency of rings produced by muons. . . . .	110
9.3	Frequency of rings produced by gammas. . . . .	110
9.4	Signal, background, and data after applying precuts. . . . .	122
9.5	Background after precuts by neutrino mode. . . . .	123
9.6	Background after precuts by interaction type. . . . .	123
9.7	Division of the Monte Carlo. . . . .	125

9.8	Configuration of the boosted decision tree. . . . .	141
9.9	Signal and background for different cut placements. . . . .	144
9.10	Signal and background after applying the boosted decision tree cut. . . . .	146
9.11	Final background by neutrino mode. . . . .	146
9.12	Final background by interaction type. . . . .	147
9.13	True PID of all rings in final background sample. . . . .	147
9.14	True PID of all rings in final signal sample. . . . .	148
9.15	Event categorization purity for the final signal sample. . . . .	149
9.16	Systematic uncertainties in event reconstruction variables. . . . .	151
9.17	Systematic uncertainty of boosted decision tree performance. . . . .	152
9.18	Systematic uncertainties in event reconstruction variables. . . . .	153
A.1	MVFIT reconstructed resolutions for true charged kaon rings. . . . .	159
A.2	MVFIT reconstructed resolutions for true muon rings. . . . .	161
A.3	MVFIT reconstructed resolutions for true gamma and electron rings. . . . .	163
B.1	Input variables for the boosted decision tree. . . . .	173

# List of Figures

2.1	Feynman diagram for fast proton decay via $p \rightarrow e^+\pi^0$ . . . . .	10
2.2	Feynman diagram for dinucleon decay via $pp \rightarrow K^+K^+$ . . . . .	11
3.1	The Super-Kamiokande detector [1]. . . . .	15
3.2	Support structure for mounting photomultiplier tubes [1]. . . . .	16
3.3	An illustration of Cherenkov radiation. . . . .	18
3.4	Cherenkov light spectrum. . . . .	19
3.5	SK event display. . . . .	20
3.6	The 20-inch ID PMT [1]. . . . .	22
3.7	Single p.e. distribution for the 20inch PMTs. . . . .	22
3.8	Quantum efficiency of the 20-inch ID PMT [1]. . . . .	22
3.9	Timing resolution for the 20-inch PMTs. . . . .	23
3.10	The ID DAQ system [1]. . . . .	26
3.11	The OD DAQ system [1]. . . . .	27
3.12	Overview of the trigger system [1]. . . . .	29
3.13	The water purification system [1]. . . . .	30
3.14	The relative gain calibration system [1]. . . . .	32
3.15	The LINAC calibration system [1]. . . . .	34

3.16	Decay electron spectrum from stopping muons used for calibration. The points represent the data and the histogram represents the Monte Carlo [1]. . . . .	35
3.17	Left: Calibration using lower energy stopping muons. The double ratio of Monte Carlo over data for the ratio $R_p$ , of measured momentum to inferred momentum from Cherenkov angle with the Monte Carlo prediction [1]. Right: Calibration using high energy stopping muons. The ratio of the momentum loss to the range. [1] . . . . .	36
3.18	$\pi^0$ mass calibration [1]. . . . .	37
3.19	Summary of energy scale calibration [1]. . . . .	37
3.20	TQ map for a 20-inch PMT. . . . .	38
3.21	Water transparency laser system [1]. . . . .	39
3.22	Attenuation length as a function of time. . . . .	41
3.23	Light scattering laser system [1]. . . . .	42
3.24	Attenuation coefficient as a function of wavelength. . . . .	43
4.1	Honda flux model for primary cosmic rays. . . . .	45
4.2	Predicted atmospheric neutrino flux at Super-Kamiokande. . . . .	46
4.3	Cross sections for quasi-elastic scattering. . . . .	48
4.4	Single pion production cross sections. . . . .	49
4.5	Deep inelastic charged current cross sections. . . . .	52
5.1	Fermi momentum distribution. . . . .	56
5.2	Kinematics of decay protons. . . . .	57
5.3	Kinematics of outgoing kaons. . . . .	57
5.4	Kaon - nucleon interaction cross-section. . . . .	59

7.1	TDC fit vertex resolution. . . . .	76
7.2	Illustration of the Hough Transformation. . . . .	77
7.3	Example of a Hough Transformed charge distribution. . . . .	78
7.4	Example of a showering ring. . . . .	80
7.5	Example of a non-showering ring. . . . .	80
7.6	<i>RTOT</i> - momentum look-up table. . . . .	86
8.1	Illustration of an ideal $pp \rightarrow K^+ K^+$ event. . . . .	101
8.2	Kaon flight distances. . . . .	102
8.3	True momentum distribution for dinucleon decay kaons. . . . .	103
8.4	Opening angle between kaon directions. . . . .	105
8.5	True momentum distribution for dinucleon decay muons. . . . .	106
8.6	True momentum distribution for dinucleon decay gammas. . . . .	107
9.1	Variables used in two-kaon classification process. . . . .	113
9.2	Illustration of the impact parameter classification variable. . . . .	114
9.3	Impact parameter using muon-like and gamma-like vertices. . . . .	114
9.4	Difference between incorrect and correct impact parameter. . . . .	115
9.5	Variables used in the kaon decay product classification process. . . . .	116
9.6	Kaon-like Cherenkov angles for dinucleon decay rings. . . . .	117
9.7	Illustration of the linearity variable. . . . .	118
9.8	Difference in linearity between kaons and other rings. . . . .	119
9.9	Reconstructed variables used in the precuts. . . . .	121
9.10	Boosted decision tree input variables for final analysis. . . . .	131
9.11	A single decision tree. . . . .	140
9.12	Training, testing, and analysis boosted decision tree output. . . . .	142
9.13	Significance curve for the boosted decision tree output. . . . .	143

9.14	Boosted decision tree output for the Monte Carlo. . . . .	145
9.15	Boosted decision tree output near the final cut. . . . .	145
10.1	Final output of boosted decision tree. . . . .	155
A.1	MVFIT resolutions for charged kaons. . . . .	160
A.2	MVFIT resolutions for muons. . . . .	162
A.3	MVFIT resolutions for gammas and electrons. . . . .	164
B.1	Input variables used to train the boosted decision tree. . . . .	169

# List of Abbreviations

ADC	.....	Analog to Digital Converter
ATM	.....	Analog Timing Module
ATM $\nu$	.....	Atmospheric Neutrino
BKG	.....	Background
CC	.....	Charged Current
CCD	.....	Charge-Coupled Device
CCQE	.....	Charged Current Quasi-Elastic
CL	.....	Confidence Level
DAQ	.....	Data Acquisition
DIS	.....	Deep Inelastic Scattering
DNDK	.....	Dinucleon Decay
EM	.....	Electromagnetism
FRP	.....	Fiber-Reinforced Plastic
GONG	.....	GO-NoGo
GUT	.....	Grand Unified Theory
ID	.....	Inner Detector
IMB	.....	Irvine Michigan Brookhaven
KAMLAND	.....	Kamioka Liquid Scintillator Anti-Neutrino Detector
LHC	.....	Large Hadron Collider
LINAC	.....	Linear Accelerator
MC	.....	Monte Carlo
MSFIT	.....	Muon-Shower Fitter
MVFIT	.....	Multiple Vertex Fitter
NC	.....	Neutral Current

OD .....	Outer Detector
PDF .....	Probability Density Function
PE .....	Photoelectrons
PID .....	Particle identification
PMT .....	Photomultiplier tube
QAC .....	Charge-to-Analog Converter
QE .....	Quasi-Elastic
QTC .....	Charge-to-Time Converter
SIG .....	Signal
SK .....	Super-Kamiokande
SK-I .....	Super-Kamiokande I
SK-II .....	Super-Kamiokande II
SK-III .....	Super-Kamiokande III
SM .....	Standard Model
SNO .....	Sudbury Neutrino Observatory
Super-K .....	Super-Kamiokande
SUSY .....	Supersymmetry
TAC .....	Time-to-Analog Converter
TDC .....	Time-to-Digital Converter
TKO .....	Tristan KEK Online
VME .....	Versa Module Europa

## Chapter 1

# Introduction

*On a long enough timeline, the survival rate for everyone drops to zero.*

–Chuck Palahniuk

Though Mr. Palahniuk's words certainly hold true for people, it remains a mystery as to whether or not his maxim can be applied equally well to protons. Protons have never been observed to decay. So far.

The age of the Universe and the very existence of life on Earth say that the proton must be stable up to at least cosmological time scales in order for the complex structure that is observed in the Universe to have arisen and continue to exist to this day. This begs the question: If the proton lifetime is (at least) cosmologically long, how can it possibly be measured experimentally? The answer lies in the fact that protons are indistinguishable from one another, thus statistically identical. So the measured lifetime will scale with the product of the number of target protons and the amount of time that they are observed. Thus one need not observe a single proton for an inhumanly long time, one need only observe a large collection of protons for an experimentally reasonable amount of time. This principle is the crux of the basic

methodology employed by large-scale detectors such as Super-Kamiokande.

The Super-Kamiokande water Cherenkov detector and its direct predecessors, Kamiokande [2] and IMB [3], have a long history of probing for physics beyond the Standard Model through searches for various modes of nucleon decay [4–7]. The target volume of water, or fiducial volume, in the center of the Super-Kamiokande tank contains 22.5 kilotons of ultra-pure water, which corresponds to about  $7.4 \times 10^{33}$  protons. As suggested previously, it is important that this number be as large as possible, because the sensitivity to the lifetime of the proton scales directly with the number of protons under observation. The detector is also used for studies of neutrino oscillations, for which it is also important to have a large target volume in order to increase the neutrino interaction rate.

One of the most impressive feats accomplished by large-scale water Cherenkov detectors was to decisively rule out one of the earliest and simplest GUTs, minimal SU(5), proposed by Georgi and Glashow [8] in 1974. IMB [3] and Kamiokande [2] accomplished this by searching for evidence of single proton decay via the mode  $p \rightarrow e^+\pi^0$ . That reaction is predicted by minimal SU(5) to occur at a rate that would yield a proton lifetime of  $10^{31\pm 1}$  years [9, 10]. IMB and Kamiokande were able to set a lower limit on the proton lifetime that was greater than the SU(5) prediction. Super-Kamiokande has since set even longer limits on the lifetime of this decay. The current limit set by Super-Kamiokande is in excess of  $10^{34}$  years [11]. This limit is two orders of magnitude larger than the upper bound predicted by SU(5).

This dissertation describes a search for evidence of dinucleon decay, which is the simultaneous decay of two nucleons bound within the same nucleus. One could imagine such a reaction being mediated by the inter-nucleon exchange of a heavy, non-standard particle. Only a few experiments have previously searched for dinucleon decay: Frejus, DAMA, and the BOREXINO Counting Test Facility (CTF).

The Frejus detector is a 900 ton tracking iron calorimeter located beneath the alps in France near the town of Frejus. The Frejus collaboration searched for dinucleon decay modes involving final state pions or leptons (*e.g.*,  $pp \rightarrow \pi^+\pi^+$ ,  $pp \rightarrow e^+e^+$ ). They did not, however, search for modes involving final state kaons. Their limits for pion and lepton dinucleon decay modes are the only such limits on record, and are on the order of  $10^{30}$  years [12].

DAMA [13] and the BOREXINO CTF [14] are both liquid scintillator detectors located in Gran Sasso, Italy. Both experiments have searched for dinucleon decay into neutrinos or invisible modes by looking for the radioactive decay of an excited nucleus that would be left behind after the disappearance of two nucleons. Frejus [15] was also able to search for the neutrino modes by using the Earth as a target volume and looking for neutrino interactions in their detector at the correct energy. All three experiments had comparable limits, and the current neutrino and invisible dinucleon decay mode limits are on the order of  $10^{25}$  years [12].

In this dissertation, the first 91.7 kiloton  $\cdot$  years of data taken by the Super-Kamiokande water Cherenkov detector are analyzed in the first experimental attempt to find evidence for dinucleon decay into kaons.

If dinucleon decay into kaons were discovered, it would provide the first evidence for baryon number violation. This would be very interesting because baryon number is a conserved quantity in the Standard Model. Thus dinucleon decay into kaons would provide clear evidence for physics beyond the Standard Model. Another reason that it would be interesting is that baryon number violation is one of the three Sakharov conditions required to explain the matter/anti-matter asymmetry of the Universe [18]

Dinucleon decay into kaon modes is also interesting in the context of supersymmetry, in that the corresponding diagram for the decay requires the presence of baryon number violating interaction vertices, characterized by the coupling parameters  $\lambda''_{ijk}$

(where  $i$ ,  $j$ , and  $k$  are generation indices) which are forbidden under  $R$ -Parity. Thus, the positive detection of dinucleon decay into kaons could provide evidence for  $R$ -Parity violation. If one of the  $\lambda''_{ijk}$  were shown to be non-zero, it could have important implications in certain supersymmetric models, potentially reducing the required amount of fine tuning by allowing a lighter bound on the Higgs mass [19]. It has been suggested that a search for dinucleon decay into kaons via  $pp \rightarrow K^+ K^+$  (the mode studied in this analysis) would be the most sensitive experimental probe of the magnitude of one of the  $\lambda''_{ijk}$  parameters,  $\lambda''_{112}$  [20–22].

There are several key differences between this particular search and the more conventional single nucleon decay searches, such as  $p \rightarrow e^+ \pi^0$ . The first is that the  $pp \rightarrow K^+ K^+$  signal included Cherenkov ring patterns created by charged kaons, which were ejected from the parent nucleus at momenta above Cherenkov threshold. The second difference is that the signal events all had multiple secondary vertices due to the subsequent decay of the kaons, separated by distances resolvable by the detector. These first two distinct features necessitated the development of a new Cherenkov ring reconstruction method able to fit a unique vertex to each ring in an event. This multiple vertex fitter is described in detail in Section 7.2.

The next key difference is that this search incorporated event topology in the particle type classification process, which is a technique that has never been incorporated in a Super-Kamiokande analysis before. Typically, a likelihood analysis predicting whether a given ring was produced by an electromagnetic showering particle (*i.e.*,  $e^\pm$  or  $\gamma$ ) or non-showering particle (*e.g.*,  $p$ ,  $K^\pm$ ,  $\pi^\pm$ ,  $\mu^\pm$ ) is sufficient for particle identification. However, in the case of the  $pp \rightarrow K^+ K^+$  signal, this method alone would not allow one to distinguish charged kaon rings from muon rings produced by the decay of the kaons via the highest branching ratio decay mode  $K^+ \rightarrow \mu^+ \nu$ . Thus the unique event topology of the signal was exploited and compared side-by-side with other ring-

specific reconstructed variables, such as the reconstructed momentum, reconstructed Cherenkov angle, etc., in order to classify the rings in an event.

The final key difference between this search and searches for single nucleon decay is that this search scanned over a very large number of discriminating variables, spanning several event categories by incorporating multivariate analysis techniques. Unlike single nucleon decay, a reasonable signal efficiency to background ratio could not be achieved by simply looking at a few variables alone, such as the invariant mass and total momentum of the original (di)nucleon decay products. While these two variables were taken into consideration, many other useful discriminatory variables were also considered, such as variables describing the event geometry, the overall symmetry of the event, the kaon decay products, and the goodness (or badness, as it were) of fitting the event using a single vertex hypothesis. Though this was not the first study from Super-Kamiokande to use multivariate analysis techniques (artificial neural networks have been used before [23]), this was the first study to utilize a boosted decision tree to analyze Super-Kamiokande data.

## Chapter 2

# Motivation and Theory

There are several motivations behind this search for dinucleon decay into kaons. One motivation is simply that such reactions are allowed by the conservation of energy, momentum, angular momentum, and charge, and have never been searched for before. A more interesting motivation is that the observation of dinucleon decay would provide evidence for baryon number violation. Baryon number (along with lepton number) is a conserved quantity in the Standard Model <sup>1</sup>, and has never been observed before.

To give this some context, other discrete symmetries once thought to be inviolate have been found not to hold in certain sectors, such as the symmetry of parity. Following the suggestions of Lee and Yang [16], Wu (amongst others) found evidence for parity violation in an experiment that measured the direction of electrons emitted by the beta decay of <sup>60</sup>Co relative to the direction of spin of the polarized cobalt atoms [17]. The results of the experiment showed that parity is violated through the weak interaction, and this discovery brought about a veritable paradigm shift in the world of physics.

---

<sup>1</sup>An exception to baryon and lepton number conservation arises in non-perturbative electroweak effects at very high energies [24].

Such historical precedents make it seem plausible that baryon number may also not constitute an exact symmetry. This would be fascinating to discover in and of itself, but it could also provide insight into the matter-antimatter asymmetry of the Universe. Sakharov proposed three conditions that, if satisfied, could explain the matter-antimatter asymmetry, one of which is the non-conservation of baryon number [18].

Though no evidence has ever been found for  $\Delta B = 1$  baryon number violation through nucleon decay modes studied at Super-Kamiokande or elsewhere (*e.g.*,  $p \rightarrow e^+\pi^0$ , or  $p \rightarrow K^+\nu$ ), this does not preclude that a  $\Delta B = 2$  interaction could not take place. Hence, a search for dinucleon decay into kaons is in fact complimentary to searches for single proton decay in terms of seeking evidence for baryon number violation.

Another motivating factor is that searches for dinucleon decay into any purely mesonic state, such as kaons, provides an interesting experimental alternative to searches for single nucleon decay, in that the former does not violate lepton number, yet the latter must in order to conserve angular momentum.

Protons are fermions, which means that they have odd spin. If they decay, they must decay into at least two lighter particles in order to conserve energy and momentum. The only known particles that are lighter than the proton are the leptons (with the exception of  $\tau$ ,  $m_\tau = 1.8 \text{ GeV}/c^2$ ) and certain mesons, such as pions. Leptons are fermions (odd spin), and mesons are bosons, which have even spin. This means that any viable proton decay mode must include an odd number of leptons in order to conserve angular momentum. Typical experimental searches focus on decay modes such as  $p \rightarrow e^+\pi^0$ . A two-nucleon system has even spin, however, and therefore does not require any leptons in the final state (though an even number of leptons would be conceivable). From the perspective of angular momentum conservation, it is perfectly

reasonable to imagine a two-nucleon system decaying purely mesonically.

Additionally, observation of dinucleon decay into kaons could have interesting implications in a supersymmetric framework. Supersymmetry (SUSY) represents a large family of Grand Unified Theories (GUTs) that attempt to unify the strong, weak, and electromagnetic forces. One distinguishing characteristic of SUSY is the introduction of superpartners to the known particles of the Standard Model (SM). The superpartners have the same quantum numbers as their corresponding SM partners (*e.g.*, color, electric charge, and hypercharge), but have the opposite spin state.

Under supersymmetry, SM fermions have bosonic superpartners, and SM bosons have fermionic superpartners. The nomenclature for the superpartners adds an ‘s’ to the beginning of the name of the particle’s corresponding SM partner. The superpartners are symbolically denoted with a tilde placed over the corresponding SM partner symbol. For example, a Standard Model fermion such as the up quark,  $u$ , is given a scalar superpartner called the sup, denoted as  $\tilde{u}$ .

In the minimal supersymmetric Model (MSSM), the number of superpartners produced or annihilated in a given reaction must conserve a symmetry called  $R$ -Parity. SM particles are assigned an  $R$ -Parity of  $+1$ , and their superpartners are assigned an  $R$ -Parity of  $-1$ . The  $R$ -Parity value of a particle,  $P_R$ , is calculated as:

$$P_R = (-1)^{2S}(-1)^{3B+L}, \quad (2.1)$$

where  $S$  is its spin,  $B$  is its baryon number, and  $L$  is its lepton number.

$R$ -Parity is a symmetry introduced to the MSSM in order to remove a select group of operators from the superpotential that is allowed by all gauge symmetries. The terms in the superpotential,  $W$ , prohibited under  $R$ -Parity are:

$$W \supset \mu_i L_i \bar{H} + \lambda_{ijk} L_i L_j E_k^C + \lambda'_{ijk} L_i Q_j D_k^C + \lambda''_{ijk} U_i^C D_j^C D_k^C, \quad (2.2)$$

where  $L$ ,  $E^C$ ,  $\bar{H}$ ,  $Q$ ,  $U^C$ , and  $D^C$  are lepton doublet, lepton singlet, up-type Higgs, quark doublet, up-type quark singlet, and down-type quark singlet superfields.  $\mu$ ,  $\lambda$ ,  $\lambda'$ , and  $\lambda''$  are the coupling strengths. The  $ijk$  indices are generation indices, and gauge indices have been suppressed. The first three terms violate lepton number, and the final term violates baryon number.

Without their removal through the introduction of  $R$ -Parity, the terms in Equation 2.2 would allow fast proton decay to occur via the diagram shown in Fig. 2.1, or one very similar. The lifetime of the proton would scale as:

$$\frac{\tau}{B.R. p \rightarrow e^+ \pi^+} \sim \frac{1}{m_p^5} \sum_{i=2,3} m_{\tilde{d}_i}^4 / |\lambda'_{11i} \lambda''_{11i}| < 1 \text{ sec} \quad (2.3)$$

where  $m_p$  is the proton mass,  $\lambda'$  and  $\lambda''$  are the  $R$ -Parity violating couplings, assumed to be of order unity, and  $m_{\tilde{d}_i}$ , are the squark masses, assumed to be of order 1 TeV [25]. Such a disastrously small prediction for the proton lifetime would ruin the relevance of the model.

It should be noted here that the diagram shown in Fig. 2.1 does not provide the motivation behind the experimental searches for  $p \rightarrow e^+ \pi^0$  at experiments like Super-Kamiokande. Such searches are primarily motivated by different decay mechanisms allowed by different models, such as SU(5).

Now, if *either* the baryon number violating term *or* the lepton number violating terms barred by  $R$ -Parity were allowed to exist in the model, the proton lifetime would still be protected. A decay channel like that of Fig. 2.1, for example, would not be permitted. Any proton decay mode must violate baryon number, as protons are the lightest baryons, but recall that an odd number of leptons are required in the

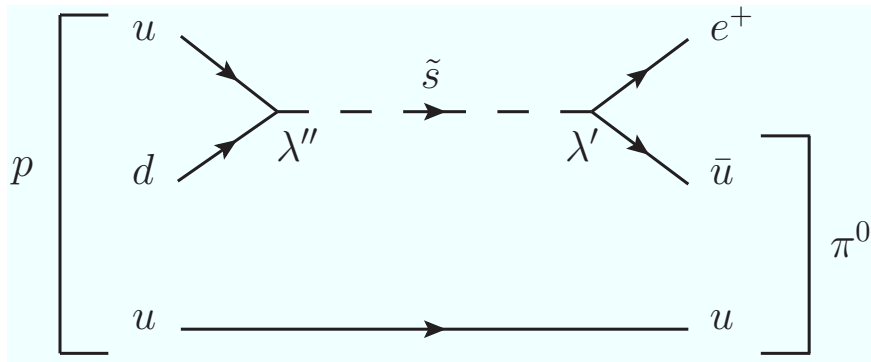


**Figure 2.1:** Feynman diagram for fast proton decay via  $p \rightarrow e^+ \pi^0$  in a supersymmetric framework without  $R$ -Parity. There is one lepton number violating interaction vertex,  $\lambda'$ , and one baryon number violating interaction vertex,  $\lambda''$ , in the diagram.

final state in order to preserve angular momentum, thus lepton number must also be violated. Therefore a model which does not provide both a mechanism to violate baryon number and a mechanism to violate lepton number will not allow single proton decay to occur.

It has been noted by Carpenter, Kaplan and Rhee that in certain supersymmetric models which allow either baryon number violation or lepton number violation through the  $R$ -Parity violating couplings (but not both baryon number and lepton number violation) a lighter bound on the Higgs mass could be allowed, which in turn could reduce the amount of fine tuning required in the model [19]. This study is concerned with the models in which the baryon number violating coupling,  $\lambda''_{ijk}$ , is allowed to be non-zero. If such were the case, one would expect dinucleon decay into kaon modes to arise through a channel such as that shown in Fig. 2.2. In this diagram, the  $\lambda''_{112} = \lambda''_{uds}$  coupling appears twice. Analogous diagrams exist for  $pn \rightarrow K^+ K^0$  and  $nn \rightarrow K^0 K^0$ . And because dinucleon decay into kaons does not say anything about lepton number violation, evidence for the signal could potentially be consistent with—and perhaps even hint at the existence of—one of these  $R$ -Parity violating,

reduced fine tuning SUSY models.

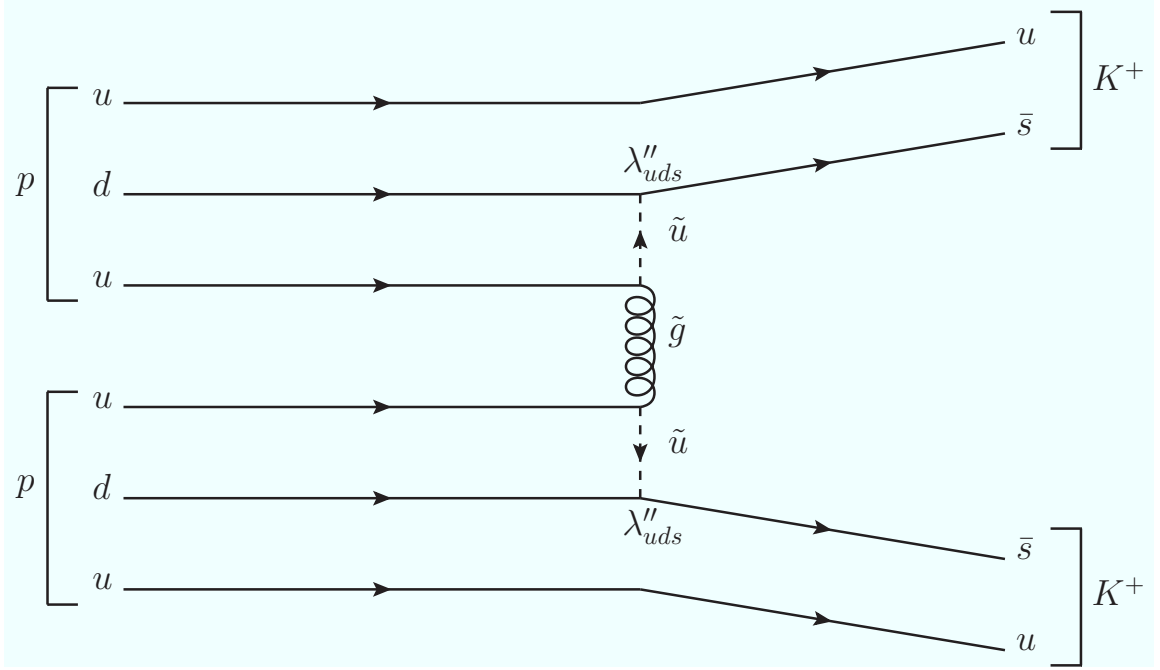


**Figure 2.2:** Feynman diagram for  $pp \rightarrow K^+K^+$  in a supersymmetric framework. There are two  $\lambda''_{uds}$  interaction vertices in the diagram.

Yukawa terms in the Lagrangian,  $\mathcal{L}$ , are derived from the superpotential,  $W$ , by the relation:

$$\mathcal{L} = -\frac{1}{2} \left( \frac{\delta^2 W}{\delta A_i \delta A_j} \bar{\Psi}_i \bar{\Psi}_j + H.C. \right), \quad (2.4)$$

where  $A_{i,j}$  are scalar fields,  $\bar{\Psi}_{i,j}$  are fermion fields, and  $H.C.$  represents the Hermitian conjugate [26]. This gives a Lagrangian term for the  $\Delta B = 1$   $R$ -Parity violating term:

$$\mathcal{L}_{U_i^C D_j^C D_k^C} = -\frac{1}{2} \lambda''_{ijk} (\tilde{u}_{iR}^* \bar{d}_{jR} d_{kL}^C + \tilde{d}_{kR}^* \bar{u}_{iR} d_{jL}^C + \tilde{d}_{jR}^* \bar{u}_{iR} d_{kL}^C) + H.C., \quad (2.5)$$

where  $ijk$  again represent generation indices,  $\bar{u}$  and  $\bar{d}$  are anti-up and anti-down-type quark fields,  $\tilde{u}$  and  $\tilde{d}$  are superpartner up and down-type fields, and  $d^C$  is a down-type

singlet field [27].

The coupling  $\lambda''_{ijk} U_i^C D_j^C D_k^C$  requires that the last two fields,  $D_j^C$  and  $D_k^C$ , have different generations (*i.e.*,  $j \neq k$ ). This happens because the suppressed color indices are combined anti-symmetrically, but the superfields themselves commute. Thus if  $D_j^C$  and  $D_k^C$  were swapped and  $j$  were equal to  $k$ , then the coupling would have to be equal to  $-1$  times itself, which would be impossible unless it were 0. Thus the introduction of a second generation field is necessary, explaining why the coupling violates strangeness by one unit.

For this reason a search for final state kaon dinucleon decay modes, such as  $pp \rightarrow K^+ K^+$  are sensitive to the  $R$ -Parity violating SUSY parameters  $\lambda''_{ijk}$ , but final state pion modes, such as  $pp \rightarrow \pi^+ \pi^+$ , are not. A similar argument explains why minimal SUSY SU(5) favors the single proton decay mode  $p \rightarrow K^+ \bar{\nu}$ , but not  $p \rightarrow \pi^+ \bar{\nu}$  (though in that case  $R$ -Parity violation is not required).

Many limits on the  $R$ -Parity violating  $\lambda''_{ijk}$  coupling constants come from experiments that can only measure a limit on a product of at least two different  $\lambda''_{ijk}$ , or a product of one  $\lambda''_{ijk}$  with one of the other  $R$ -Parity violating coupling constants. A summary of experimental constraints on these parameters is given in [27, 28]. Dinucleon decay into kaons, however, would be sensitive to a single coupling alone,  $\lambda''_{uds}$ , and has been reasoned to be the most sensitive means of experimentally probing the magnitude of the coupling  $\lambda''_{uds}$  [20–22].

An upper limit on  $\lambda''_{uds}$  has been estimated based on typical experimental limits on nuclear lifetimes from single nucleon decay experiments and the Frejus limits on lepton pion dinucleon decay modes. Goity and Sher used an approximate figure of  $\sim 10^{30}$  years as the lower lifetime limit for dinucleon decay into kaons, and calculated an upper limit on the magnitude of  $\lambda''_{uds}$  to be  $10^{-7}$ . Appendix C.2 explains the calculation of the upper limit on  $\lambda''_{uds}$  as obtained by a lower limit on the  $pp \rightarrow$

$K^+ K^+$  partial lifetime. It is the goal of this dissertation to conduct a more sensitive, direct search for dinucleon decay into kaons in order to provide evidence for dinucleon decay, or to set a more authoritative experimental bound on the  $R$ -Parity violating parameter  $\lambda''_{uds}$ .

## Chapter 3

# Experimental Apparatus

### 3.1 Super-Kamiokande Detector Overview

Super-Kamiokande is a large water Cherenkov detector located about 1 km beneath the peak of Mt. Ikenoyama in the Mozumi zinc mine near the town of Kamioka in the Gifu prefecture of Japan. Figure 3.1 shows a schematic drawing of the detector and its surrounds.

The overburden of rock is roughly equivalent to 2700 m of water shielding, lowering the flux of cosmic ray muons to about  $6 \times 10^8 \text{ cm}^{-2} \text{ s}^{-1} \text{ sr}^{-1}$ . The resultant muon event rate is five orders of magnitude lower than at that the surface of the earth. Super-Kamiokande is filled with 50 kilotons of ultra-pure water, making it the largest detector of its kind in the world.

Data taking began at Super-Kamiokande in April 1996 and continued for five years until a scheduled shutdown for maintenance and upgrading in July 2001. This initial five year period of data taking is referred to as Super-Kamiokande I, or simply SK-I. Regrettably, during the shutdown an accident occurred which required a significant alteration of the detector for the next data taking period, SK-II, reducing the number

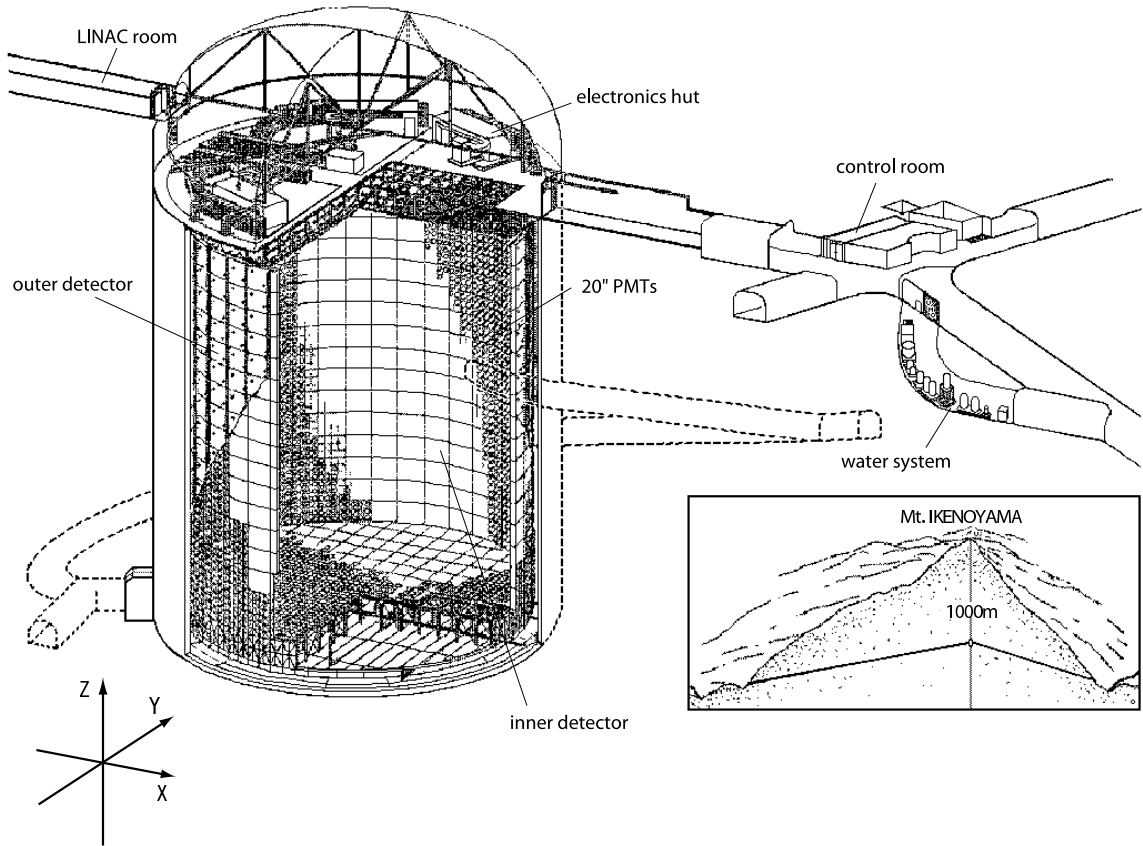


**Figure 3.1:** The Super-Kamiokande detector [1].

of ID PMTs to about half that of original design. The SK-II data taking period began in October 2002 and lasted for three years, ending in October 2005. The detector has since been restored to full PMT capacity beginning with the SK-III data taking period, which began in July 2006. This thesis is concerned only with data taken during the SK-I period, corresponding to 1489.2 days of livetime and 91.5 kiloton · years of exposure.

## 3.2 Structure

The water containment structure of Super-Kamiokande is a stainless steel, cylindrical water tank oriented in an upright position. It has a full diameter of 39.3 m and a

height of 41.4 m. The tank is optically segmented into two separate regions: a smaller concentric cylinder called the Inner Detector and the region between the outer walls of the tank itself and the outside of the support structure, called the Outer Detector. These regions are physically separated from one another by a 55 cm thick stainless steel support structure on which the photomultiplier tubes are mounted. The two regions have been optically isolated from one another by covering the support structure with a plastic black sheet. Figure 3.2 illustrates how the photomultiplier tubes are arranged on the support structure.

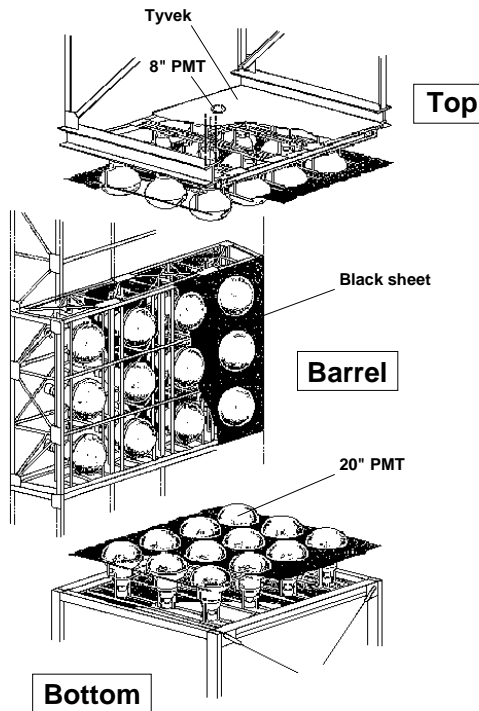


**Figure 3.2:** Support structure for mounting photomultiplier tubes [1].

### 3.2.1 Inner Detector (ID)

The Inner Detector (ID) is a cylinder 33.8 m in diameter and 36.2 m tall, concentric to the full Super-Kamiokande tank. It contains 32 kilotons of ultra-pure water. For

SK-I, the ID is instrumented with 11,146 inward facing 20-inch photomultiplier tubes arranged in a uniform grid-like pattern. Roughly 40% of the ID wall surface is thus photosensitive.

### 3.2.2 Outer Detector (OD)

The Outer Detector (OD) is a 2 m thick region surrounding the Inner Detector on all sides. It is instrumented with 1,885 outward facing 8-inch photomultiplier tubes. Each of the OD PMTs is embedded in the center of a  $60 \times 60 \text{ cm}^2$  wavelength shifting plate to increase the effective photosensitive area. The OD is used to veto cosmic ray muon events and tag partially contained physics events. It also acts as a shield against radioactivity in the rock surrounding the detector. White Tyvek lines the walls of the OD to maximize reflection, thus increasing efficiency in detecting and identifying cosmic rays and partially contained events.

## 3.3 Cherenkov Radiation

The process by which Super-Kamiokande observes and reconstructs particle physics events is through the detection and interpretation of Cherenkov radiation. Cherenkov radiation is the light emitted by a relativistic charged particle as it travels through a medium while its speed remains above that of light in the given medium.

In the case of Super-Kamiokande the medium is pure water, which has an index of refraction  $n = 1.33$ . The requirement for a charged particle to produce Cherenkov radiation in Super-Kamiokande is:

$$\beta > \frac{1}{n} = 0.75, \quad (3.1)$$

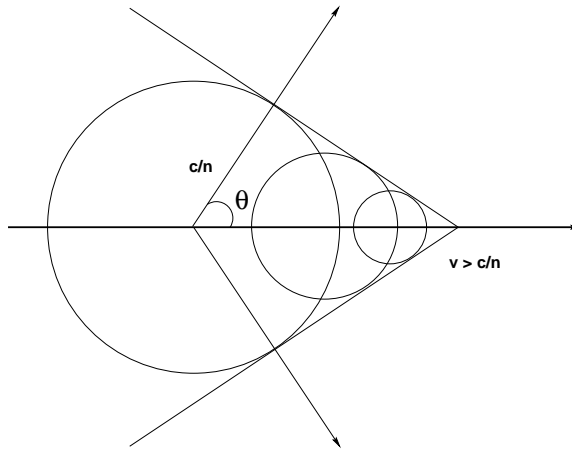


**Figure 3.3:** An illustration of Cherenkov radiation.

where  $\beta = v/c$ ,  $v$  being the magnitude of the particle's velocity and  $c$  being the speed of light in vacuum. This can be re-expressed in terms of more practical quantities as:

$$p > 1.14 \times m/c, \quad (3.2)$$

where  $p$  is the particle's momentum,  $m$  is the particle's mass, and  $c$  is the speed of light in vacuum.

The Cherenkov light is emitted at an acute angle relative to the particle's momentum vector. This produces a cone-like projection forward along the particle's direction of travel, as illustrated in Fig. 3.3. The cone's half-opening angle, referred to as the Cherenkov angle  $\theta_C$ , is dependent upon the particle's relativistic speed,  $\beta$ , as such:

$$\cos(\theta_C) = \frac{1}{n\beta}. \quad (3.3)$$

If a particle is highly relativistic such that  $\beta \simeq 1$ , then its Cherenkov angle will be maximal,  $\theta_C \simeq 42^\circ$ . This is almost always the case for extremely light particles (*i.e.*, electrons and positrons) produced in particle physics events of the type studied

at Super-Kamiokande. More massive particles (*e.g.*, charged kaons) tend to produce “collapsed” cones with smaller Cherenkov angles at typical Super-Kamiokande energy scales.

The spectrum of light emitted by a Cherenkov radiating particle is given by the following formula:

$$\frac{d^2N}{dx d\lambda} = \frac{2\pi\alpha}{\lambda^2} \left( 1 - \frac{1}{n^2\beta^2} \right), \quad (3.4)$$

where  $\lambda$  is the wavelength of light,  $x$  is the distance traveled by the particle, and  $\alpha$  is the fine structure constant. In the sensitive region of the photomultiplier tubes used in the Super-Kamiokande detector (300–600 nm), roughly 340 photons are emitted per centimeter traversed by the particle. Figure 3.4 shows the relative spectrum of Cherenkov light in pure water is covered well by the sensitive range of Super-Kamiokande’s photomultiplier tubes.

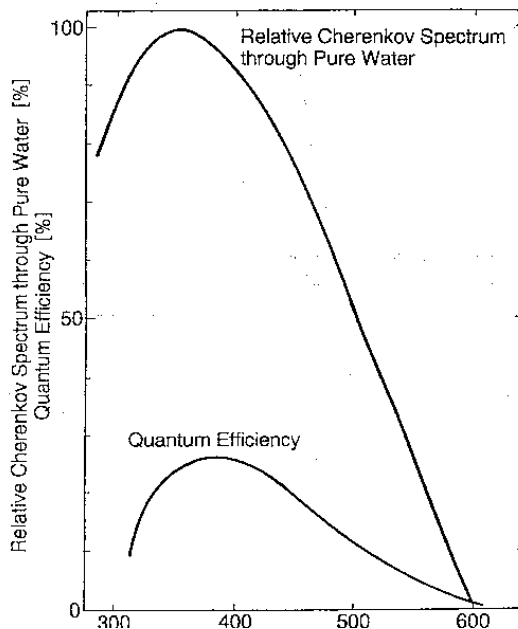


**Figure 3.4:** Relative spectrum of Cherenkov light in pure water and quantum efficiency of the 20-inch ID photomultiplier tubes [29].

The Cherenkov light that is produced by charged particles in an event at Super-Kamiokande travels through the water with little attenuation until it finally reaches the wall of the ID. There the photomultiplier tubes collect the light and convert it into an electronic signal which is interpreted as a “hit”. The Cherenkov light cones produce ring-shaped hit patterns when projected onto the wall, and from these ring patterns one is able to count the number of charged particles produced in an event, as well as discern some other crucial information about each of those particles. Figure 3.5 shows an example of a Super-Kamiokande event display.

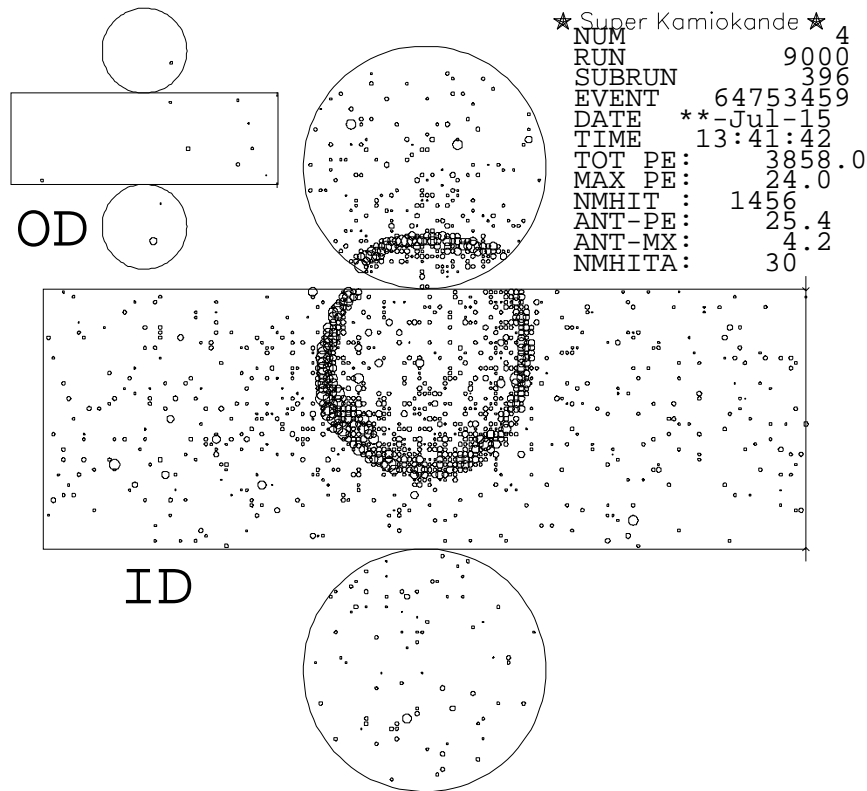


**Figure 3.5:** Example of an event at Super-Kamiokande using an “unrolled” event display. The circular regions at the top and bottom represent the top and bottom endcaps, respectively. The horizontal rectangle in the middle represents the unrolled side walls of the barrel. Each tiny circle represents a hit PMT, where the size of the PMTs circle is proportional to the amount of charge observed by that PMT. The smaller display in the corner shows the activity in the OD. Here, a single ring has been produced by a muon. The hits outside of the ring are from scattered and reflected light.

The momentum of the particle is roughly proportional to the total amount of light in the ring it produced. One may distinguish between an electromagnetic showering type particle (*i.e.*, an electron, positron, or gamma) and a more massive particle (*e.g.*, a charged kaon or a muon) by taking note of the relative sharpness of the outer edge of the ring. A showering type particle will produce a fuzzier ring pattern than a non-showering type. Particle vertex positions may also be reconstructed by taking note of the timing of each of the PMT hits as well as their position relative to one another and relative to the fixed geometry of the tank.

## 3.4 Photomultiplier Tubes

### 3.4.1 Inner Detector Photomultiplier Tubes

The 20 inch diameter photomultiplier tubes (PMTs) used in the ID during the SK-I experimental period were originally developed specifically for Super-Kamiokande by the Hamamatsu Corporation. Figure 3.6 shows a schematic drawing of the ID PMT. These PMTs were designed to have a large photosensitive area, a good timing resolution, the ability to detect a single photo-electron, and long term stability. The “Venetian blind” dynode was adjusted to improve timing resolution and photon collection efficiency, ultimately achieving a timing resolution of about 2.5 ns. Single photo-electron peaks can clearly be distinguished from dark noise in the PMT signal. Figure 3.7 shows the single photo-electron (p.e.) distribution.

The quantum efficiency of the ID PMTs is shown in Fig. 3.8. The PMTs have a significant quantum efficiency over the range of roughly 300–600 nm with a maximum efficiency of 20% at 390 nm wavelength. This range of wavelengths covers the spectrum of Cherenkov light emitted in pure water quite well. The photocathode of

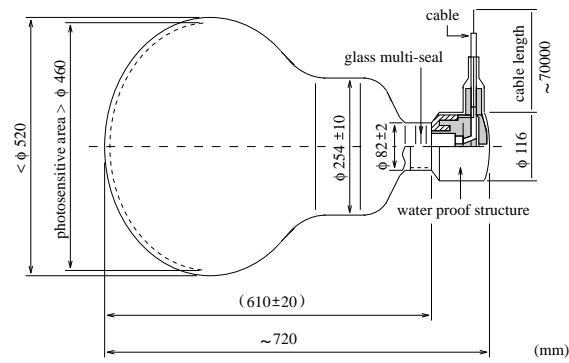


**Figure 3.6:** The 20-inch ID PMT [1].

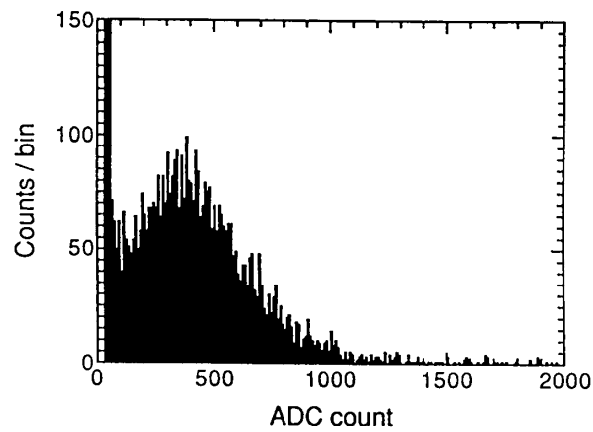


**Figure 3.7:** Single p.e. distribution for the 20-inch ID PMT. A single p.e. is equivalent to about 2 pC at  $10^7$  gain. The peak near 0 corresponds to the dark current [1].

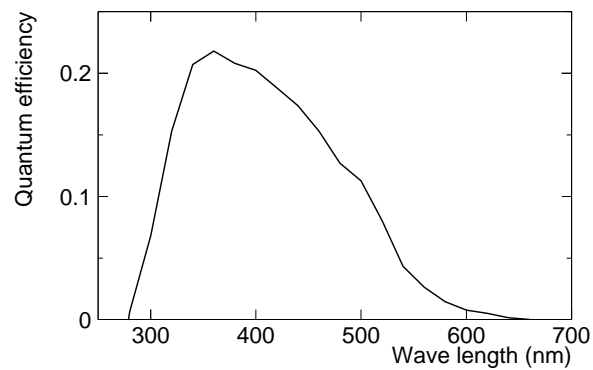


**Figure 3.8:** Quantum efficiency of the 20-inch ID PMT [1].

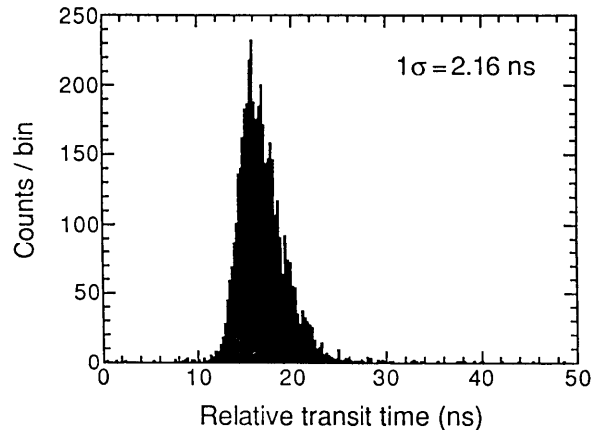


**Figure 3.9:** Transit time spread for single p.e. equivalent signals in the 20-inch ID PMT. The spread is interpreted as the timing resolution of the PMT [1].

the PMTs is Bialkali (Sb-K-Cs) for its high sensitivity to Cherenkov light and low thermionic emissivity. The transit time spread for a 1 p.e. signal is about 2.2 ns, as shown in Fig. 3.9. The average dark noise rate is around 3 kHz at the threshold of 1/4 photo-electrons, which is the threshold value used during normal operational conditions at Super-Kamiokande. A more complete list of specifications for the ID PMTs is shown in Table 3.1.

The response of the ID PMTs is sensitive to magnetic fields, so it is critical that the 450 mG produced by the geomagnetic field at Super-Kamiokande be reduced. This is achieved by a system of 26 Helmholtz coils arranged around the detector, reducing the net magnetic field to approximately 50 mG.

### 3.4.2 Outer Detector Photomultiplier Tubes

The 8 inch diameter PMTs used in the OD during the SK-I experimental period were model R1408 Hamamatsu PMTs procured from the decommissioned IMB experiment. The photocathodes of the OD PMTs are each fitted with a 60 cm × 60 cm × 1.3 cm acrylic wavelength shifter plate, increasing the total OD light collection ef-

Product Name	R3600
Shape	Hemispherical
Photocathode area	50 cm (20 in) diameter
Window material	Pyrex glass (4 ~ 5 mm)
Photocathode material	Bialkali (Sb-K-Cs)
Quantum efficiency	22 % at $\lambda = 390$ nm
Dynodes	11 stage Venetian blind type
Gain	$10^7$ at $\sim 2000$ V
Dark current	200 nA at $10^7$ gain
Dark pulse rate	3 kHz at $10^7$ gain (1/4 p.e threshold)
Cathode non-uniformity	< 10 %
Anode non-uniformity	< 40 %
Transit time	90 nsec at $10^7$ gain
Transit time spread	2.2 nsec ( $1\sigma$ ) for 1 p.e. equivalent signals
Weight	13 kg
Pressure tolerance	6 kg/cm <sup>2</sup> water proof

**Table 3.1:** Specifications for the 20-inch ID PMT [1].

iciency by about 50%. The presence of the wavelength shifter plates degrades the timing resolution of the OD PMTs from 11 ns to 15 ns, but this is still sufficient to allow the OD to function well as a cosmic ray veto counter.

## 3.5 Data Acquisition (DAQ) System

### 3.5.1 Inner Detector DAQ

The front end electronics of the ID DAQ are comprised of custom built Analog Timing Modules (ATMs), into which are fed the analog signals of the ID PMTs. The ATMs are housed in Tristan KEK Online (TKO) crates located in the four outer electronics huts sitting on top of the Super-Kamiokande tank. The ATMs are responsible for recording and digitizing the arrival time and integrated charge information of each PMT signal via a 12-bit Analog to Digital Converter (ADC).

The ATMs each have two separate channels, allowing them to store two successive PMT pulses when required. This function makes it possible to detect muon-decay electrons produced by muon decays, and also allows the front end electronics to handle high rate events that could be generated by nearby supernovae or possibly other rare phenomena.

Both channels in an ATM consist of a time to amplitude converter (TAC) for recording the timing information of a PMT pulse, and a charge to analog converter (QAC) for recording the integrated charge of the pulse. The full time range is  $1.6 \mu\text{s}$  with a resolution of  $0.3 \text{ ns}$ . The charge saturation level is  $600 \text{ pC}$ , which corresponds to approximately 300 p.e., and the charge resolution is  $0.2 \text{ pC}$ . Table 3.2 contains a more complete list of specifications for the ATM.

Number of channels	12 ch/board
One hit processing time	$\sim 5.5 \mu\text{sec}$
Charge dynamic range	$\sim 400 \sim 600 \text{ pC}$ (12-bit)
Timing dynamic range	$\sim 1300 \text{ nsec}$ (12-bit)
Charge resolution (LSB)	$0.2 \text{ pC/LSB}$
Charge resolution (RMS)	$0.2 \text{ pC (RMS)}$
Timing resolution (LSB)	$0.3 \sim 0.4 \text{ nsec/LSB}$
Timing resolution (RMS)	$0.4 \text{ nsec (RMS)}$
Temperature dependence (QAC)	$3 \text{ Count/deg.} \leftrightarrow 0.6 \text{ pC/deg.}$
Temperature dependence (TAC)	$2 \text{ Count/deg.} \leftrightarrow 0.8 \text{ nsec/deg.}$
Event number	8 bit
Data size of one hit	6 Byte
FIFO	2 kByte ( $\sim 340 \text{ hits}$ )

**Table 3.2:** Specifications for the ATM module [1].

Each ATM typically handles 12 PMTs, and there are (with rare exception) 20 ATMs slotted into each TKO crate. Each of the four outer electronics huts is home to 12 TKO crates. Along with the ATMs, there is a go/no-go (GONG) trigger control module and a super control header (SCH) in every TKO crate. The SCH



### 3.5.2 Outer Detector DAQ

Unlike the ID PMTs, the signals from the OD PMTs are taken from the high voltage lines which provide them power. The high voltage to an OD PMT is distributed by a “paddle card” through a coaxial cable, and the signal is picked off by a capacitor located on the paddle card.

The signals are fed from the paddle cards into custom built Charge to Time Converter (QTC) modules, which consist of LeCroy MQT200 chips and comparators and comprise the heart of the OD DAQ’s front end electronics. There the signals are converted into a rectangular pulses each having a width proportional to the input signal’s charge. There are 5 QTCs distributed over 2 TKO crates within each of the outer electronics huts shared by the ID DAQ electronics. Each QTC reads in signals from 48 PMTs served by 4 paddle cards (12 PMTs per paddle card).

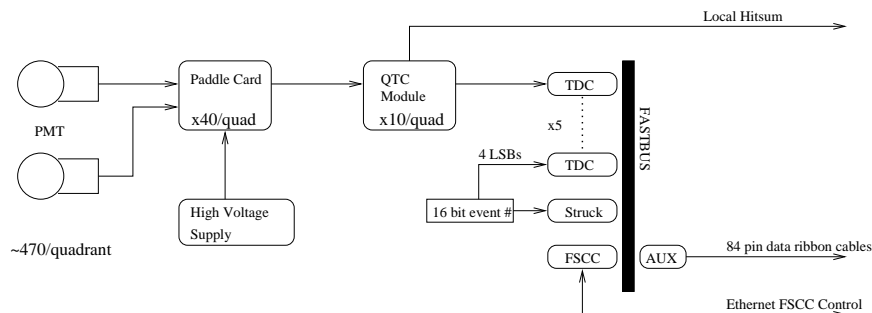


**Figure 3.11:** The OD DAQ system [1].

When the QTC receives a PMT signal, it simultaneously generates a rectangular HITSUM signal (see Section 3.5.3) that is sent to the global trigger system, which has a threshold set to  $1/4$  p.e. If a global trigger signal is received by the OD electronics, the leading edge and width of the rectangular pulse are converted to the corresponding time and charge information by a LeCroy 1877 multi-hit TDC module. The TDC module can record up to 8 QTC output pulses at a resolution of 0.5 ns. The dynamic range of the TDC module is set to  $16 \mu\text{s}$  before the global trigger time. The digitized

data stored in the TDC modules are read by a slave computer through a VME memory module called the dual port memory (DPM) and are then sent to the online host computer where they are added to the overall event information. Figure 3.11 shows a schematic of the OD DAQ system.

### 3.5.3 Event Trigger System

The global event trigger system looks for a large number of hit PMTs within a 200 ns window. It does this by checking the added HITSUM pulses from all of the detector's ATMs (or QTCs in the case of the OD). The HITSUM pulses are 200 ns wide signals with a height of  $15 \text{ mV} \times$  the number of hit PMTs belonging to a given ATM (QTC). Thus, the pulse height of the global HITSUM signal is proportional to the number of hit PMTs throughout the detector within a 200 ns window.

If the global HITSUM signal for the ID (OD) exceeds 29 (19) hit PMTs, then a global trigger signal is issued to the hardware trigger (TRG) module. The TRG module records the trigger type and trigger generation time using a 50 MHz clock, counts an event number with a 16-bit counter, and generates a global trigger signal that gets sent to the detector electronics, causing the data to be read out and processed. Figure 3.12 shows an overview of the global trigger generation scheme.

The trigger system also includes an "Intelligent Trigger" designed specifically for low energy events, but such events are not considered in this study and thus this trigger's description is irrelevant for the purposes of this thesis and will be omitted here.

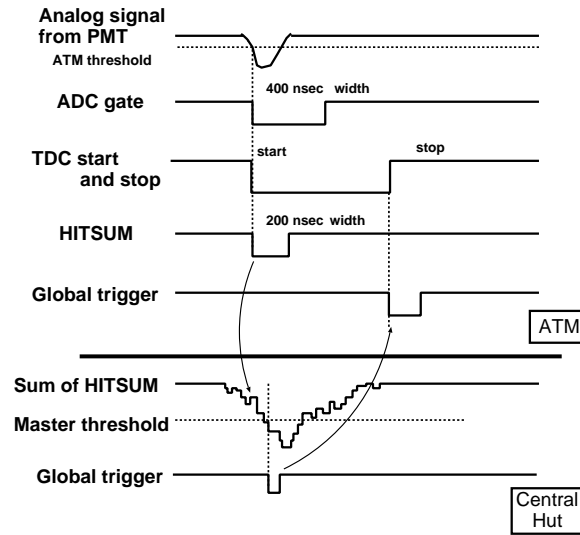


Figure 3.12: Overview of the trigger system [1].

## 3.6 Water Purification System

The water in Super-Kamiokande is continuously cycled through a sophisticated purification system (see Fig. 3.13) at a rate of about 35 tons per hour, completely recirculating all of the water in the tank over a period of about 70 days. The purpose of the purification system is to minimize light attenuation and to keep out radioactive impurities, such as radon, which substantiate much of the background in low energy ( $<10$  MeV) solar neutrino studies.

Maintaining a high level of water purity is critical to one's ability to accurately reconstruct physics events, as it increases the collection efficiency of the photomultiplier tubes, thus increasing the amount of data available in any given event. Temporal stability in the water purity level is also a crucial requirement for accurate modelling of the Cherenkov radiating process in the physics event reconstruction algorithms.

The purification cycle begins with a filter to remove dust larger than  $\sim 1 \mu\text{m}$ , followed by a heat exchanger which cools the water to  $13^\circ \text{C}$ . The water is then passed along to a cartridge polisher to remove any heavy ions. From there, it is passed to

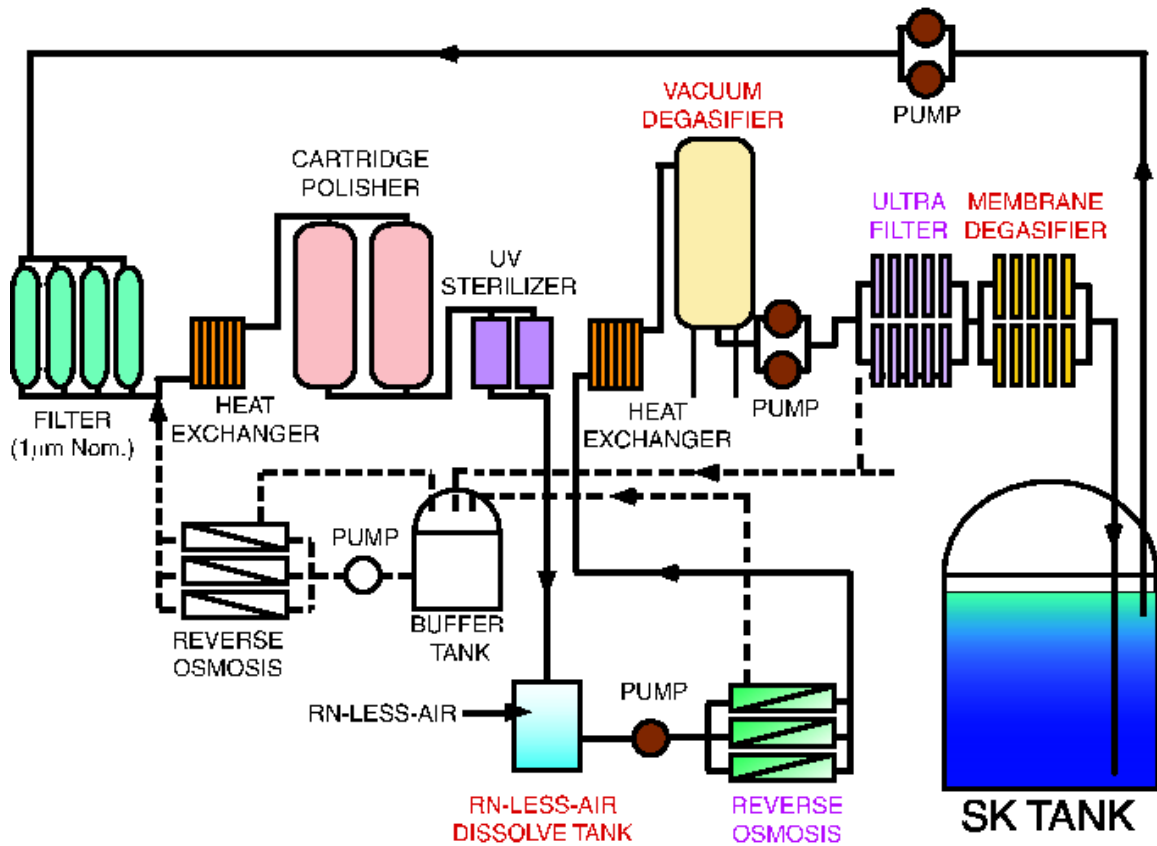


Figure 3.13: The water purification system [1].

an ultraviolet sterilizer which kills bacteria, and then a reverse osmosis and vacuum degassifier system for removing radon and other dissolved gasses. Finally the water is passed through a second filtering stage, removing particles larger than  $\sim 10$  nm, and then on to a membrane degassifier to reduce the radon levels even further, after which it is returned again to the tank.

The purification system keeps the radon level in the tank to around  $0.4 \text{ mBq/m}^3$ . The number density of particles in the water larger than  $\sim 2 \mu\text{m}$  is approximately  $6/\text{cm}^3$ . The attenuation length of light is  $\sim 100$  m at a wavelength of 420 nm. The resistivity of the water before and after passing through the filtration system is about  $11 \text{ M}\Omega\cdot\text{cm}$  and  $18.20 \text{ M}\Omega\cdot\text{cm}$ , respectively.

## 3.7 Calibration

### 3.7.1 Relative Gain Calibration

It is important that the gain of the PMTs be kept as uniform as possible in order to minimize position and direction dependent systematic errors in reconstructed momentum. Accordingly, the high voltage is adjusted individually on each PMT to homogenize the gain throughout the detector.

To calibrate the relative gains of the individual PMTs, a Xe-powered scintillator ball is lowered into the tank at several different fixed positions. The scintillator ball is made of an acrylic containing BBOT wavelength shifter and MgO powder diffuser. A Xe lamp followed by an ultraviolet (UV) filter and a neutral density (ND) filter provide the light to the ball via an optical fiber. The BBOT shifts the light to the visible range, peaking at 440 nm, and the light is diffused through the ball isotropically into the detector. The UV light from the Xe source is simultaneously sent to a monitoring system outside of the tank to monitor the light intensity and to generate a calibration trigger. Figure 3.14 shows a drawing of the relative gain calibration system.

The relative gain of the  $i$ th PMT is given by:

$$G_i = \frac{1}{f(\theta_i)} \frac{Q_i}{Q_0} r_i^2 \exp\left(\frac{r_i}{L}\right), \quad (3.5)$$

where  $Q_i$  is the charge of the  $i$ th PMT,  $f(\theta_i)$  is the angular acceptance of the  $i$ th PMT, which depends on the angle  $\theta$  between the axis of symmetry of the PMT and the direction of the incident photon,  $r_i$  is the distance from the Xe ball to the  $i$ th PMT,  $L$  is the attenuation length of the water, and  $Q_0$  is a normalization factor. In the relative gain calibration process, the high voltage of each PMT is adjusted in order to minimize the spread of  $G_i$  over all of the ID PMTs, yielding an overall spread

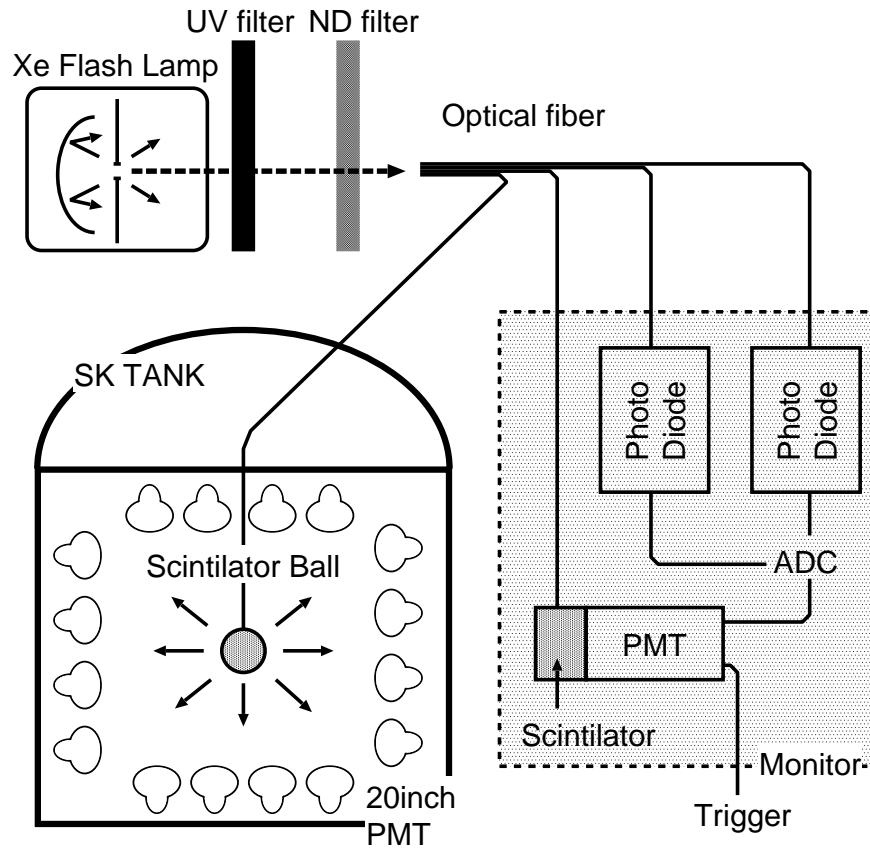


**Figure 3.14:** The relative gain calibration system [1].

in the relative gain of about 7%.

### 3.7.2 Absolute Gain Calibration

For measurement of the charge produced by a single photoelectron in a PMT, a low energy source must be used. To serve this purpose, a  $\text{Cf}^{252}$  source surrounded by Ni wire is used. The Cf source and Ni wire are encased in a polyethylene vessel and lowered into the tank, where the Cf emits neutrons through spontaneous fission that are captured by the Ni wire causing the emission of  $\gamma$  rays at various energies, most commonly 9 MeV. Each  $\gamma$  ray then produces an electromagnetic shower which in turn generates Cherenkov light that is observed by about 50–80 PMTs in total,

with no more than one p.e. per PMT. Single p.e. distributions are created for every PMT to set the conversion factor from raw observed charge in pC to a number of p.e. The mean value of the peaks, 2.055 pC, is used as the conversion factor from charge to p.e.

### 3.7.3 Energy Scale Calibration

The energy scale calibration is critical for many of the physics studies performed at Super-Kamiokande. Because of its importance and because of the large range in energies that are seen in the detector, several different methods are employed in the energy scale calibration process.

#### LINAC

For very low energies, a LINAC is used to inject electrons into the detector with energies ranging from 5 to 16.3 MeV. The LINAC setup can be seen in Fig. 3.15. The Monte Carlo is tuned to agree with the LINAC data to within 1%.

#### $^{16}\text{N}$ Decay

$^{16}\text{N}$  is used as another low energy calibration source. By lowering a deuterium-tritium generator into the detector  $^{16}\text{N}$  can be produced in the water. When it decays, an electron with an energy of up to 4.3 MeV, and a photon with an energy of 6.1 MeV are produced. The energy scale from this method agrees with the LINAC-tuned Monte Carlo to within 0.64%.

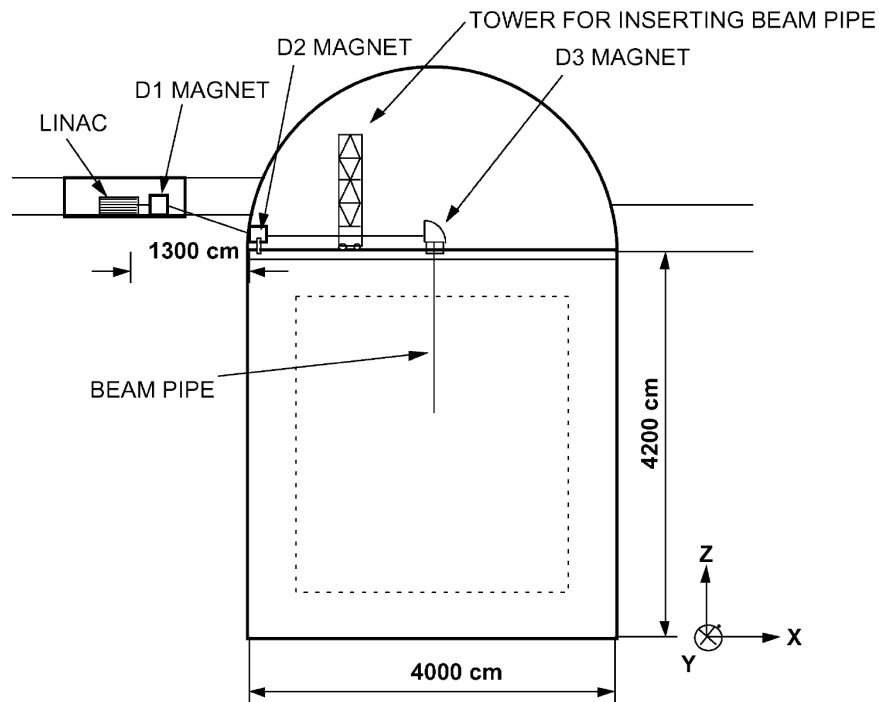


**Figure 3.15:** The LINAC calibration system [1].

### Decay Electrons

All of the cosmic ray muons which stop and subsequently decay in the detector provide a large sample of muon-decay electrons, which have a well known spectrum in the range of tens of MeV. The data from decay electrons and the Monte Carlo show the energy scale in the relevant range agrees to within 2.0%.

### Stopping Muons

Stopping muons (muons which stop somewhere in the detector) are used for energy calibration in two different ranges. For muons with momenta of up to approximately  $400 \text{ MeV}/c$ , the Cherenkov angle can be used to accurately measure the momentum. This momentum is compared to the momentum determined by the number of photoelectrons collected. The energy scale agreement between data and Monte Carlo for

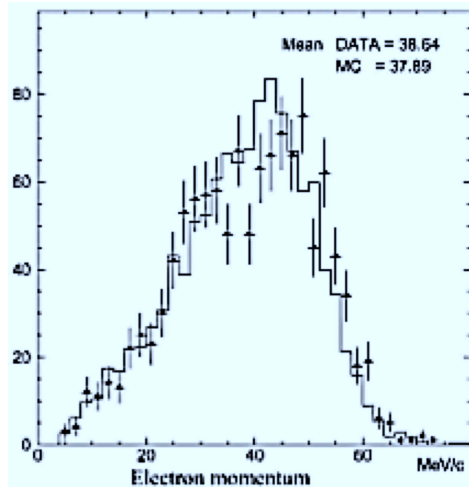


**Figure 3.16:** Decay electron spectrum from stopping muons used for calibration. The points represent the data and the histogram represents the Monte Carlo [1].

stopping muons in the range of 200–400 MeV is within 1.5%.

At higher momenta, the Cherenkov angle is indistinguishable from the maximal value of  $42^\circ$ , thus is independent of the muon energy and cannot be used for momentum determination. Instead, the distance traveled by the muon inside the detector is used in the calibration. This distance is calculated by locating the entry point of the muon and the vertex position of the decay electron it produced. A momentum can be inferred from the travel distance, which is compared to the number of photoelectrons collected. For the energy range 700 MeV to 3.5 GeV, the data and Monte Carlo agree to within 2.6%.

Figure 3.17 shows the relevant calibration distributions for the two stopping muon energy ranges.

### $\pi^0$ Reconstruction

A single  $\pi^0$  is often produced by neutral current neutrino interactions in Super-Kamiokande. The  $\pi^0$  always decays immediately into two  $\gamma$ s, each of which will

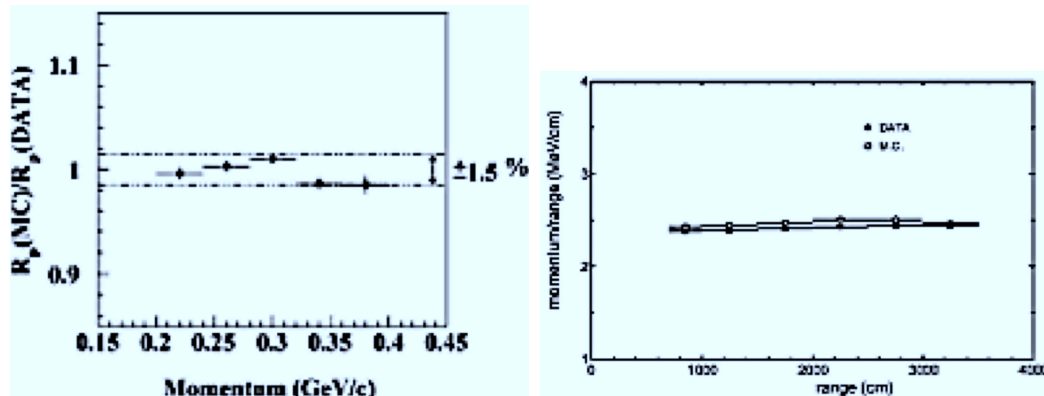


**Figure 3.17:** Left: Calibration using lower energy stopping muons. The double ratio of Monte Carlo over data for the ratio  $R_p$ , of measured momentum to inferred momentum from Cherenkov angle with the Monte Carlo prediction [1]. Right: Calibration using high energy stopping muons. The ratio of the momentum loss to the range. [1]

produce a Cherenkov ring in the detector. The invariant mass of these  $\gamma$ s is reconstructed and compared between data and Monte Carlo, as shown in Fig. 3.18. These distributions were made by calculating the invariant mass for all events which were found to contain two showering ( $e$ -like) rings. A Gaussian fit over the range 100–200  $\text{MeV}/c^2$  was then applied to both distributions. This calibration method finds the energy scale agreeing in the range of 150–600  $\text{MeV}$  to within 1%.

### Energy Scale Summary

All of the energy scale calibrations are summarized in Fig. 3.19. The different methods all agree to within about 2%.

### 3.7.4 Relative Timing Calibration

The relative timing calibration of the PMTs is critical for vertex position reconstruction. The length of the signal cables and the amplitude of the signal itself are both factors that have an effect on the timing response of the PMTs. The signal am-

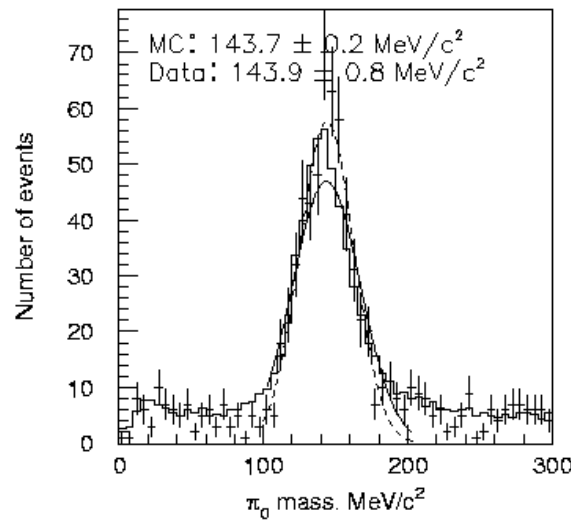


Figure 3.18:  $\pi^0$  mass calibration [1].

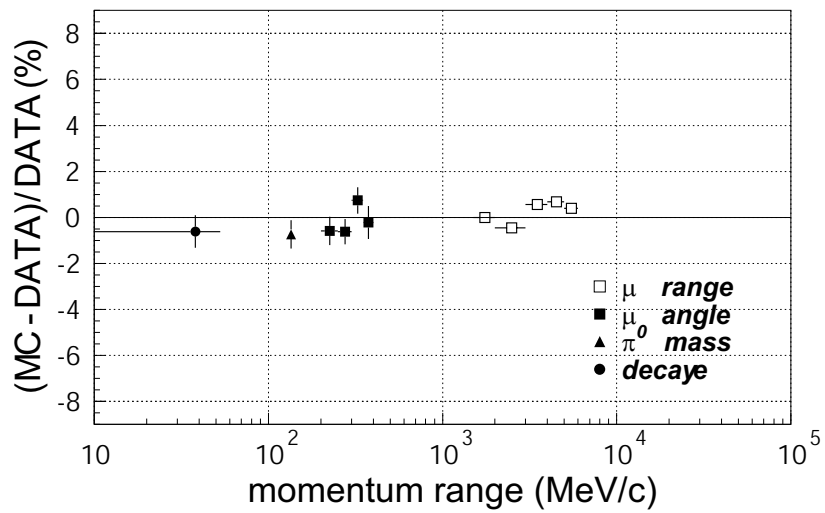
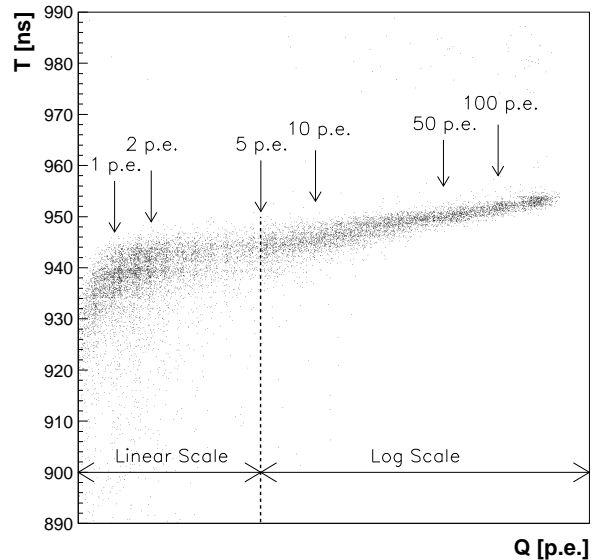


Figure 3.19: Summary of energy scale calibration [1].

plitude plays a role because of the time-walk effect, where smaller signals reach the discriminator threshold at a later time relative to their peak than do larger signals.

The hit timing of the PMTs is calibrated using an  $N_2$  laser. The laser emits 3 ns light pulses at 337 nm, which is shifted to 384 nm by a dye laser module. The light is then carried to a diffuser ball inside the tank by an optical fiber. The light is emitted into a  $TiO_2$  diffuser tip inside the diffuser ball, which is made of LUDOX

silica gel, all of which allows the light to be very uniformly distributed throughout the detector without significantly increasing the timing spread. Time-charge (TQ) maps are created from the laser calibration process and are implemented in the Monte Carlo and applied to the data. A typical TQ map can be seen in Fig. 3.20.



**Figure 3.20:** TQ map for a typical Super-Kamiokande PMT. Larger time (T) values correspond to earlier hits [1].

### 3.7.5 Water Transparency Measurement

The water transparency measurement gives the attenuation length of light across the Cherenkov light spectrum observed at Super-Kamiokande. The two effects that go into the attenuation length calculation are the amount of scattering and the amount of absorption as a function of wavelength. Understanding the attenuation length is critical to correctly model the light yield in the Monte Carlo. The water transparency is measured using three different methods: a laser ball, cosmic ray muons, and a laser fiber.

## Laser Ball

To measure the water transparency, a Nd:YAG laser is used to pump a Ti:Sa laser, the light from which is carried via optical fiber to a diffuser ball in the detector. A CCD camera placed at the top of the tank measures the intensity of the light from the diffuser ball through the water. The light is simultaneously sent along another optical fiber to an external PMT where the beam intensity is monitored. The intensity of the beam can be adjusted with a variable attenuation filter, and a range of wavelengths can be chosen. A drawing of the water transparency laser system can be seen in Fig. 3.21.

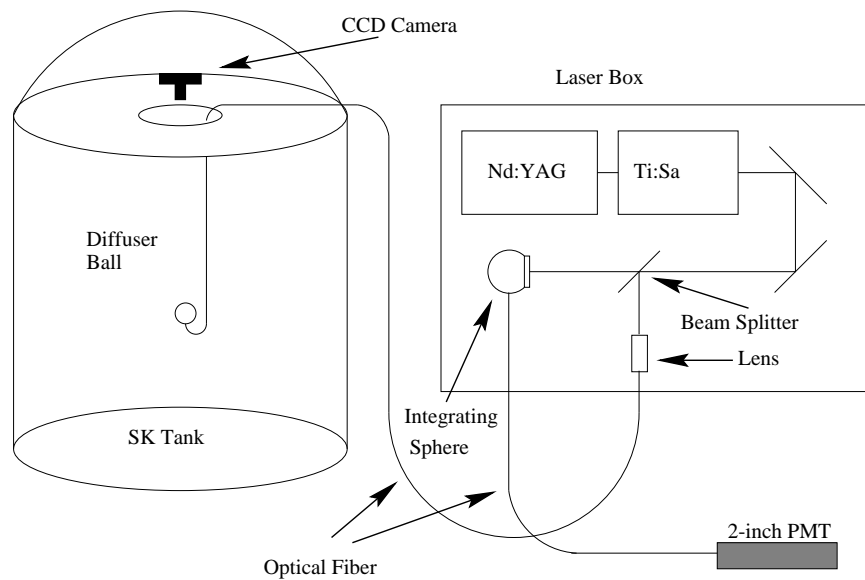


**Figure 3.21:** Water transparency laser system [1].

The ball is lowered to various depths and several measurements are taken at several wavelengths for each depth. After taking data at each depth and each wavelength, the attenuation length as a function of wavelength  $L(\lambda)$  is calculated by fitting the function:

$$\log \frac{I_{CCD}}{I_{\text{laser}}} = A - \frac{l_d}{L(\lambda)}, \quad (3.6)$$

where  $A$  is a constant,  $I_{CCD}$  is the intensity of the light seen at the CCD camera,  $I_{\text{laser}}$  is the intensity of the light at the laser monitor PMT, and  $l_d$  is the depth of the diffuser ball.

The laser ball measurement is repeated over time to account for variation in the attenuation length correlated with the water purification cycle.

### Cosmic Ray Muons

Vertical, downward-going cosmic ray muons which traverse the entire length of the detector are also used to measure water transparency. Because these muons are all highly energetic, they produce a constant number of Cherenkov photons per unit length traveled in the detector. Thus, the water transparency can be measured by correlating the charge observed by each PMT and its distance from the muon track. The muon track is reconstructed by creating a line between its entrance and exit points in the detector.

The charge  $Q$  observed at each PMT is given by:

$$Q = Q_0 \cdot \frac{f(\theta)}{l} \cdot \exp\left(-\frac{l}{L}\right), \quad (3.7)$$

where  $Q_0$  is a constant,  $f(\theta)$  is the PMT acceptance as a function of the incident angle of the photon,  $l$  is the path length of the photon, and  $L$  is the attenuation length.

One of the advantages of the cosmic ray muon measurement of the water transparency is that it can be done during normal data taking. The time variation of the attenuation length as measured by cosmic ray muons can be seen in Fig. 3.22.

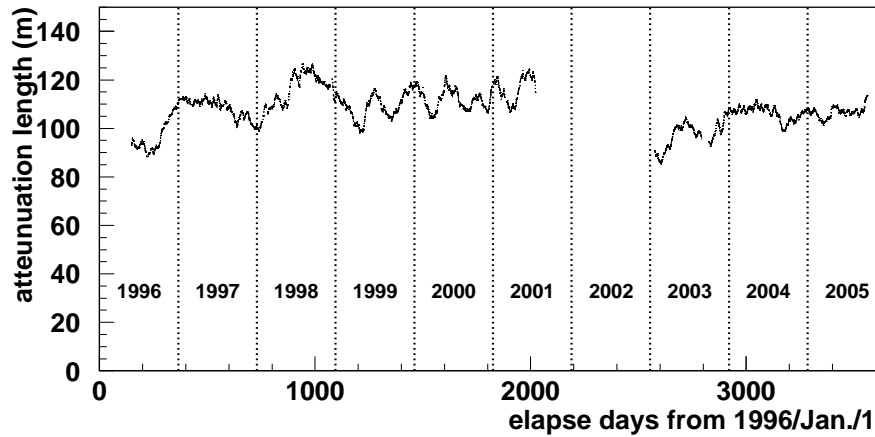


**Figure 3.22:** Attenuation length as a function of time, attained from downward-going cosmic ray muons [1].

### Light Scattering

The attenuation length is given by:

$$L = (\alpha_{\text{abs}} + \alpha_{\text{scat}})^{-1}, \quad (3.8)$$

where  $\alpha_{\text{abs}}$  is the coefficient corresponding to absorption and  $\alpha_{\text{scat}}$  is the coefficient corresponding to scattering.

To separately measure the effects of scattering in the water, a  $\text{N}_2$  laser with a wavelength selecting dye module is used. Monochromatic light at 337 nm, 371 nm, 400 nm, and 420 nm is produced and injected into the detector via an optical fiber pointing straight down toward the bottom of the tank. The laser is fired every 6 seconds during normal data taking. Figure 3.23 shows a drawing of the light scattering laser system.

As can be seen in Fig. 3.23, the barrel of the detector is divided into 5 regions for this measurement. With this setup, the PMT hits that occur at the top or at the barrel of the detector are clearly due to scattered or reflected photons. The absorption and scattering coefficients are tuned such that the PMT hit timing distributions are in

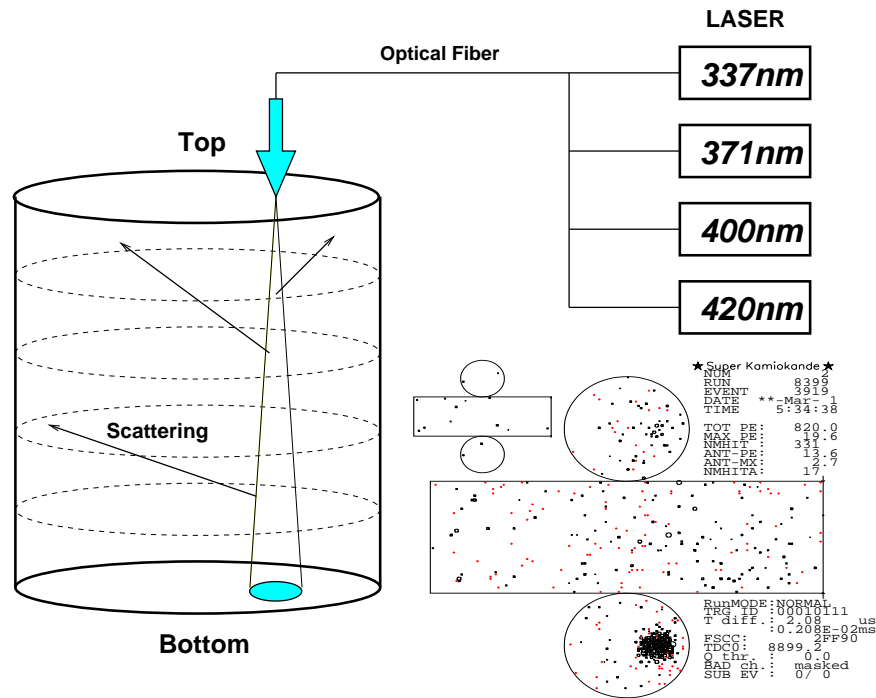


**Figure 3.23:** Light scattering laser system [1].

agreement with the light scattering calibration data taken with the laser fiber setup.

Figure 3.24 shows the final results of the attenuation coefficient calculation. The markers in the plot represent the data from the laser system and the solid and dashed lines represent the model used in the Monte Carlo, which includes the effects of Rayleigh scattering, Mie scattering, and absorption. The Monte Carlo is tuned to fit the laser data.

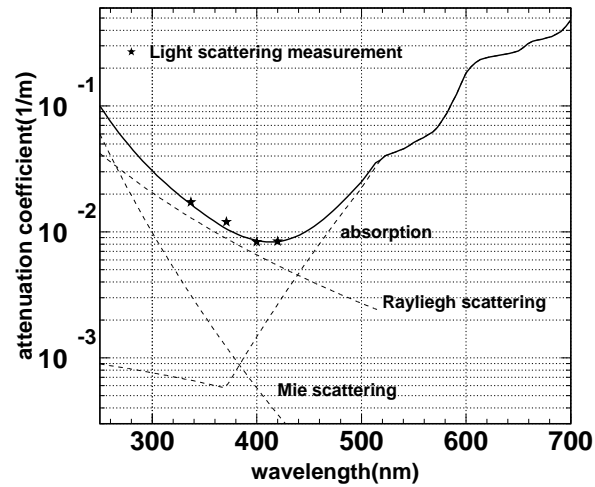


**Figure 3.24:** Attenuation coefficient as a function of wavelength. Markers indicate data taken by the laser system. Solid and dashed lines indicate the model used in the Monte Carlo [1].

## Chapter 4

# Atmospheric Neutrino Monte

## Carlo

The only source of background in this search arises from atmospheric neutrino interactions taking place within the detector. Atmospheric neutrinos are one of the final by-products of cosmic rays which strike the atmosphere. Primary cosmic rays interact hadronically with the nuclei of air molecules in the upper atmosphere to create a shower of mesons mostly comprised of pions and kaons. The pions and kaons then produce neutrinos as they progress down their respective decay chains. For the most part, these neutrinos pass through the earth without interacting at all. However, a small fraction of them do interact inside the inner detector of Super-Kamiokande at a rate of about 8 per day. When summed over the total livetime of the experiment, this tallies up to a substantial amount of background events to sort out, thus it is important to understand and model their production and interaction rates.

## 4.1 Atmospheric Neutrino Flux

The atmospheric neutrino flux model used by Super-Kamiokande is the Honda flux model [30]. The flux of primary cosmic rays used in the Honda flux model is parametrized and fitted to experimental data as shown in Fig. 4.1. The effects of Earth's geomagnetic field and solar wind are taken into account in the primary cosmic ray flux calculation, the latter of which can cause fluctuations as large as a factor of two or more for 1 GeV cosmic rays and about 10% at 10 GeV.

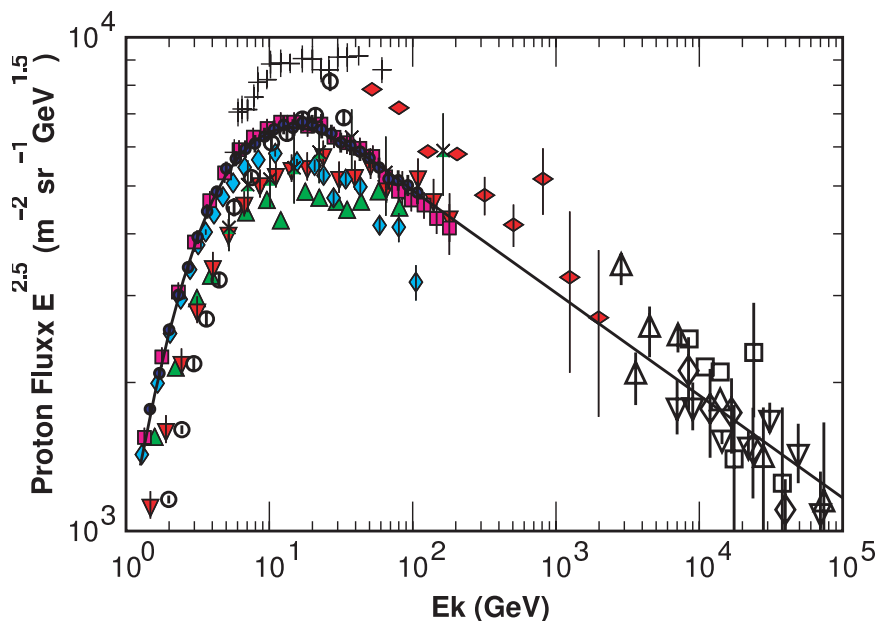


**Figure 4.1:** Flux of primary cosmic rays as predicted by the Honda flux model and observed experimentally. The data points are from the following experiments: Webber [31] (crosses), LEAP [32] (upward triangles), MASS1 [33] (open circles), CAPRICE [34] (vertical diamonds), IMAX [35] (downward triangles), BESS98 [36] (circles), AMS [37] (squares), Ryan [38] (horizontal diamonds), JACEE [39] (downward open triangles), Ivanenko [40] (upward open triangles), Kawamura [41] (open squares), and Runjob [42] (open diamonds).

The simulation model for primary cosmic ray interactions with the nuclei of air molecules was based on the NUCRIN [43] model for cosmic ray energies below 5 GeV and DPMJET-III [44] for energies above 5 GeV. The interactions generated in the

simulation give a profile of the secondary particles, including pions and kaons. The atmospheric neutrino flux is then obtained from the decays of these secondary particles.

The final atmospheric neutrino flux at Super-Kamiokande as calculated by Honda, *et al.* is shown in Fig. 4.2. The Honda flux was compared to models by Barr [45] (Fluka) and Battistoni [46] (Bartol), and all three models show agreement to within about 10% for neutrino energies up to 10 GeV. The energy range of interest in this study is around the mass of two nucleons, roughly 2 GeV. The overall systematic uncertainty of the absolute atmospheric neutrino flux is about 25% due to uncertainties in the absolute flux and interactions of the primary cosmic rays.

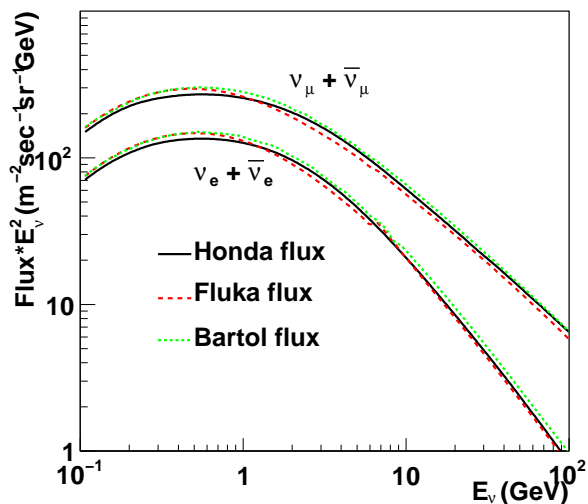


**Figure 4.2:** Atmospheric neutrino flux at Super-Kamiokande as predicted by the Honda flux model (solid), Fluka flux model (dashed), and Bartol flux model (dotted).

## 4.2 Neutrino Interactions

The NEUT [47] model was used to simulate the atmospheric neutrino interactions in Super-Kamiokande. This model includes the following four basic types of interaction:

(quasi-)elastic scattering :  $\nu + N \rightarrow l + N'$

single meson production :  $\nu + N \rightarrow l + N' + meson$

coherent pion production :  $\nu + N \rightarrow l + N' + hadrons$

deep inelastic scattering :  $\nu + {}^{16}O \rightarrow l + {}^{16}O + \pi$

where  $\nu$  represents the incoming atmospheric neutrino or anti-neutrino of either flavor ( $\mu$  or  $e$ ),  $N$  and  $N'$  represent the original and outgoing nucleon ( $p$  or  $n$ ), respectively, and  $l$  represents the outgoing lepton. Note that  $l$  can be either a charged lepton in the case of a charged current (CC) interaction, or a neutrino in the case of a neutral current (NC) interaction. All of the four interaction types above can be of CC or NC type.

Fermi momentum and Pauli blocking are taken into account for all of the neutrino-nucleon interactions. Fermi momentum of nucleons in  ${}^{16}O$  is calculated using the same technique described in Section 5.1. Pauli blocking is simulated by requiring that the momentum of the recoil nucleon exceed the Fermi surface momentum of the  ${}^{16}O$  nucleus, taken to be 225 MeV/ $c$  in NEUT.

### 4.2.1 Elastic and Quasi-Elastic Scattering

The  $V - A$  theory calculated by Llewellyn-Smith [48] is used to simulate the elastic and quasi-elastic interactions. These events typically produce only one ring from the outgoing lepton, or in some cases, a recoil proton with a momentum above Cherenkov threshold. For this reason, they are a rare background in this search, though occasionally more rings can be produced by such means as multiple scattering or subsequent hadronic interactions of the recoil nucleon.

The charged and neutral current quasi-elastic scattering cross sections from the Llewellyn-Smith model are shown in Fig. 4.3. cross sections for both neutrinos and

anti-neutrinos are shown in the figure.

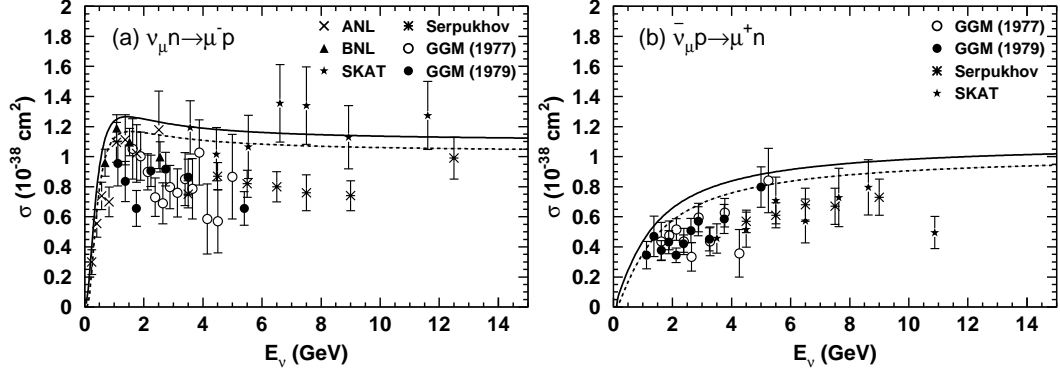


**Figure 4.3:** Cross sections for quasi-elastic scattering of  $\nu_\mu$  (left) and  $\bar{\nu}_\mu$  (right) used by NEUT (lines) overlaid on data (markers) from ANL [49], Gargamelle [50–52], BNL [53], Serpukhov [54] and SKAT [55].

## 4.2.2 Single Meson Production

Cross sections for single meson production are taken from Rein and Sehgal’s model [56]. This type of interaction becomes significant for neutrino energies above  $\sim 1$  GeV, where it is possible to form baryonic resonances which decay pionically:

$$\begin{aligned}\nu + N &\rightarrow l + N^* \\ N^* &\rightarrow N' + meson ,\end{aligned}$$

where  $N$  and  $N'$  are the initial and final state nucleons, respectively,  $N^*$  is an intermediate state baryonic resonance, and  $l$  is the outgoing lepton (charged lepton or neutrino).

The  $\Delta(1232)$  resonance is the dominant resonance below 1.4 GeV. For this resonance only, the angular distribution of pions is treated specially by the Rein and Sehgal model. An isotropic angular distribution is assumed for all other resonances.

Though rare, the production of  $\eta$  and  $K$  mesons is also included in the model.  $\eta$  and  $K$  single meson production account for only 4% and 0.6% of all the atmospheric

neutrino Monte Carlo events, respectively. Nonetheless, these are important interactions to consider in this analysis, which explicitly searches for rings from charged kaons and their decay products.

The cross sections for charged current single meson production interactions used in the Monte Carlo are shown in Fig. 4.4, overlaid on the relevant experimental data.

Single meson  $\Delta$  resonance interactions can create events with multiple rings, including rings from charged pions and recoil protons, both of which may be classified as muon candidates in the analysis (see Section 9.4.5). For these reasons, this type of atmospheric neutrino interaction was found to be the second largest source of background in the dinucleon decay search.

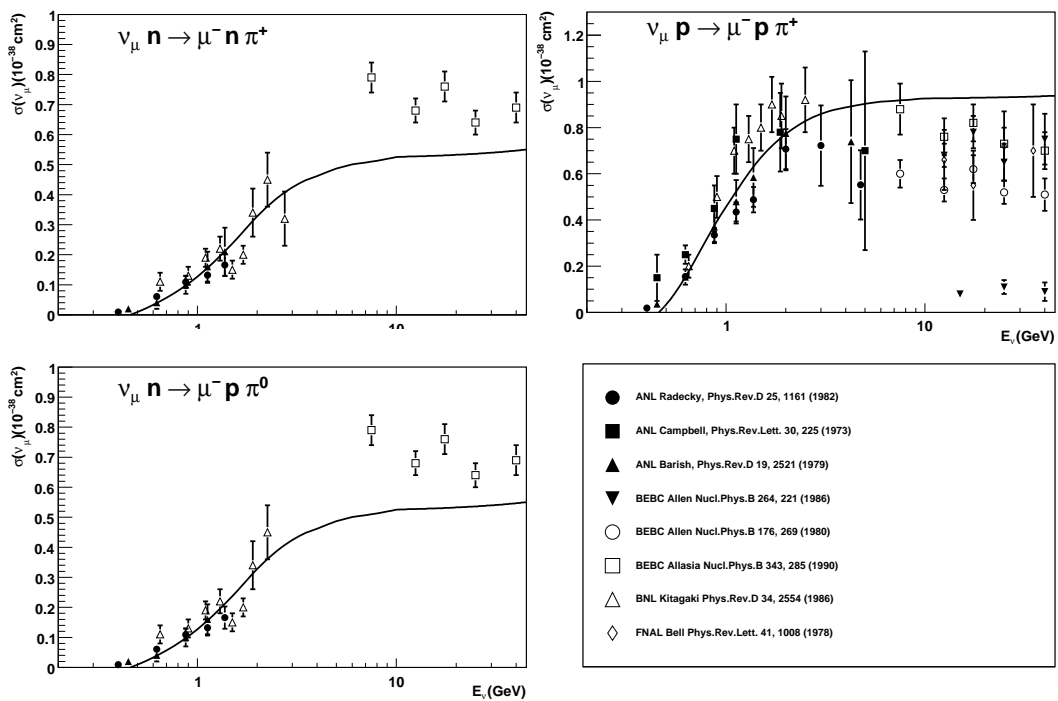


**Figure 4.4:** Single pion production cross sections from the Monte Carlo model (lines) and experimental data (markers). Top left: charged pion production off of a proton. Top right: charged pion production off of a neutron. Lower left: neutral pion production. Lower right: Key for the experimental data points.

### 4.2.3 Coherent Pion Production

When a neutrino scatters off of the entire  $^{16}\text{O}$  nucleus as a whole, rather than off of a single one of its constituent nucleons, a pion can be produced in a process called coherent pion production. The pion will carry away the same charge as the incoming weak current. The nucleus absorbs very little of the momentum exchanged in the interaction, thus the angular distribution of the outgoing pion is peaked in the direction of the incoming neutrino.

Because the pion never experiences the nuclear environment, only a single pion is produced in the interaction. More than 1 or 2 rings can be produced by coherent pion production if the outgoing pion interacts hadronically in the water, though such events are rare. Because this analysis is concerned only with events that have 3 rings or more, coherent pion production constitutes a small portion of the total background, and will not be discussed in detail in this dissertation. For more information on the treatment of coherent pion production in the atmospheric neutrino Monte Carlo, see [57].

### 4.2.4 Deep Inelastic Scattering

Two different models are used to calculate cross sections for deep inelastic scattering. A custom model [58] is used for interactions with an invariant mass  $W$  of the resulting hadrons from 1.3 to 2.0  $\text{GeV}/c^2$ , where only pions are considered as outgoing mesons. Due to their ability to produce several non-showering Cherenkov rings in a single event, multi-pion production from deep inelastic scattering of atmospheric neutrinos in this energy range was found to be the most prevalent source of background in this search.

For energies in excess of 2.0  $\text{GeV}/c^2$ , PYTHIA/JETSET [59] is used, which consid-

ers a wider variety of outgoing mesons. In all deep inelastic scattering calculations, the GRV98 [60] parton distribution function is used, including corrections from Bodek and Yang [61].

Studies have been conducted at Fermilab [62] using a 15-foot hydrogen bubble chamber to find the mean number of pions,  $\bar{n}_\pi$ , produced by deep inelastic interactions, found to be:

$$\bar{n}_\pi = 0.09 + 1.83 \ln W^2. \quad (4.1)$$

The KNO (Koba-Nielsen-Olsen) scaling is used to determine the number of pions in each deep inelastic scattering neutrino event. To avoid conflicts with the single pion production model in the overlapping range of  $W$ , at least two pions must be produced to invoke the deep inelastic scattering calculation.

The forward-backward asymmetry of the pion production was studied at the BEBC [63] experiment, and is given by:

$$\frac{\bar{n}_\pi^f}{\bar{n}_\pi^b} = \frac{0.35 + 0.4 \ln W^2}{0.50 + 0.09 \ln W^2}. \quad (4.2)$$

The charged current cross sections used in the Monte Carlo are shown in Fig. 4.5 along with the relevant experimental data.

Based on experimental results that are reviewed in [64] and [65], neutral current cross sections were assumed to have the following relationship to the charged current cross sections:

$$\frac{\sigma(\nu N \rightarrow \nu X)}{\sigma(\nu N \rightarrow \mu^- X)} = \begin{cases} 0.26 & (E_\nu < 3 \text{ GeV}) \\ 0.26 + 0.04(E_\nu/3 - 1) & (3 \text{ GeV} \leq E_\nu < 6 \text{ GeV}) , \\ 0.30 & (E_\nu \geq 6 \text{ GeV}) \end{cases} \quad (4.3)$$

$$\frac{\sigma(\bar{\nu} N \rightarrow \bar{\nu} X)}{\sigma(\bar{\nu} N \rightarrow \mu^+ X)} = \begin{cases} 0.39 & (E_\nu < 3 \text{ GeV}) \\ 0.39 - 0.02(E_\nu/3 - 1) & (3 \text{ GeV} \leq E_\nu < 6 \text{ GeV}) . \\ 0.37 & (E_\nu \geq 6 \text{ GeV}) \end{cases} \quad (4.4)$$

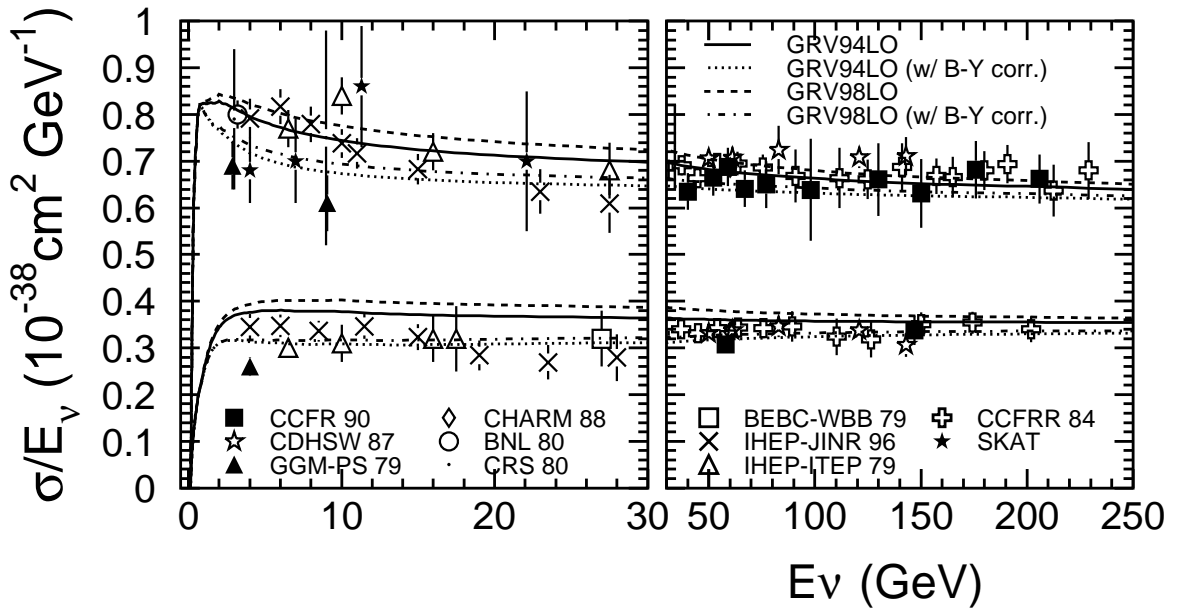


**Figure 4.5:** cross sections for deep inelastic charged current interactions. Calculations are shown for models with and without Bodek-Yang corrections for neutrinos (top curves) and anti-neutrinos (bottom curves). Experimental data points (markers) are overlaid.

### 4.3 Nuclear Effects

Mesons and nucleons created or scattered inside the  $^{16}\text{O}$  nucleus may interact hadronically by inelastic scattering, charge exchange, and/or absorption as they prop-

agate through the nuclear environment. To simulate these effects, a mean free path is first calculated using a point of origin determined by the Woods-Saxon distribution (Equation 5.1). A cascade model is then used to simulate inelastic scattering, charge exchange, and absorption. The results from  $\pi - N$  scattering experiments [66] are used in the determination of the final momentum from inelastic scattering or charge exchange. Pauli blocking is taken into account for all interactions.

## 4.4 Detector Simulation

Once the particles have left the parent nucleus, their propagation through the detector, the emission of Cherenkov light, and the response of the PMTs is handled by a GEANT3 [67] based Monte Carlo simulation of the Super-Kamiokande detector. Data acquisition electronics and trigger systems are also simulated in the Monte Carlo. A list of the simulated physics processes for each particle type is shown in Table 4.1.

Hadronic interactions above 500 MeV are simulated using the CALOR [68, 69] program, and a custom program developed originally for the Kamiokande experiment [58] based on experimental data from  $\pi$ - $^{16}\text{O}$  and  $\pi$ - $p$  scattering [70] is used for hadronic interactions below 500 MeV. Simulation results are compared to the CALOR package and the Fluka model to estimate systematic uncertainties for hadronic interactions.

A Poisson distribution with a mean given by Equation 3.4 is used to determine the number of Cherenkov photons generated at each wavelength, which are emitted at an angle given by Equation 3.3. Rayleigh scattering, Mie scattering, and absorption as described in Section 3.7.5 are all simulated for the Cherenkov photons.

PMT response is based on the quantum efficiency curve shown in Fig. 3.8 and the single photoelectron distribution.

particle type	simulated processes
$\gamma$	e <sup>+</sup> e <sup>-</sup> pair production Compton scattering Photoelectric effect
e <sup>±</sup>	Multiple scattering Ionization and $\delta$ -ray production Positron annihilation Cherenkov radiation
$\mu^{\pm}$	Decay in flight and at rest Multiple scattering Ionization and $\delta$ -ray production Direct e <sup>+</sup> e <sup>-</sup> pair production Nuclear interactions Cherenkov radiation
<i>hadrons</i>	Decay in flight and at rest Multiple scattering Ionization and $\delta$ -ray production Hadronic interactions Cherenkov radiation

**Table 4.1:** Physics processes simulated in the GEANT3 Super-Kamiokande Monte Carlo.

## Chapter 5

# Dinucleon Decay Monte Carlo

The dinucleon decay mode  $^{16}\text{O}(pp) \rightarrow ^{14}\text{C} K^+ K^+$  was studied in this analysis. The reasons for choosing this mode in lieu of other dinucleon decay modes with final state kaons (*i.e.*,  $^{16}\text{O}(pn) \rightarrow ^{14}\text{N} K^+ K^0$  and  $^{16}\text{O}(nn) \rightarrow ^{14}\text{O} K^0 K^0$ ) are described in Chapter 9. A total of 75,000 events of  $^{16}\text{O}(pp) \rightarrow ^{14}\text{C} K^+ K^+$  were simulated.

The  $^{16}\text{O}(pp) \rightarrow ^{14}\text{C} K^+ K^+$  Monte Carlo (also referred to as simply the “ $pp \rightarrow K^+ K^+$  Monte Carlo”) was generated in two stages. In the first stage, the kinematics of the kaons are determined, and any intra-nuclear interactions that take place before the kaons leave the parent nucleus are simulated. In the second stage, the kaons are propagated through the water using the official Geant3 [67] Super-Kamiokande detector simulation software described in Section 4.4.

## 5.1 Intra-Nuclear Simulation

In the dinucleon decay Monte Carlo, the Fermi gas model is used to determine the magnitude of each parent nucleon’s momentum. Figure 5.1 shows the distribution of momenta for the  $s$  and  $p$  wave states that were used. Because the vector sum of the decaying nucleons will always be non-zero, the outgoing kaons will never be

ejected with exactly back-to-back trajectories. The kinetic energy gained from the Fermi momentum is relatively small compared to that gained from the rest mass of the parent nucleons, however, so the kaons will still have a very large opening angle between them the great majority of the time.

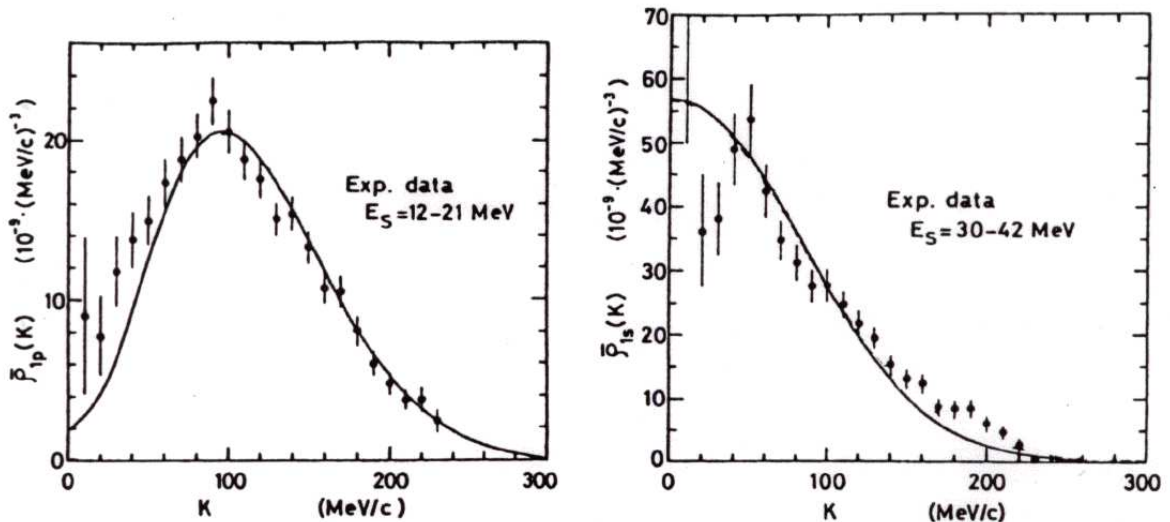


**Figure 5.1:** Calculated Fermi momentum distribution used in the Monte Carlo (lines) overlaid on experimental data points from electron scattering off  $^{12}\text{C}$  [71] (markers). Left:  $p$ -state. Right:  $s$ -state.

The momentum of the kaons can also be modified by an effect called “correlated decay”. The Monte Carlo assumes that there is a 10% chance of a correlated decay [72] occurring in a given dinucleon decay event. Correlated decay is the name given to the decay process in which a third, spectator nucleon becomes involved in the decay interaction, absorbing a portion of the available energy. The resulting momentum distribution of the kaons and the spectator nucleon is akin to a three-body decay. Correlated decay is speculated to happen on theoretical grounds, based on the overlapping of wave functions. As this process is not well understood, a 100% uncertainty was taken with this effect when calculating the systematic errors in the analysis.

Figure 5.2 shows the simulated kinematics of the original protons before they decay, and Fig. 5.3 shows the kinematics of the outgoing kaons from the decay. The effect of correlated decay can be seen in the tails of the plots in the latter figure.

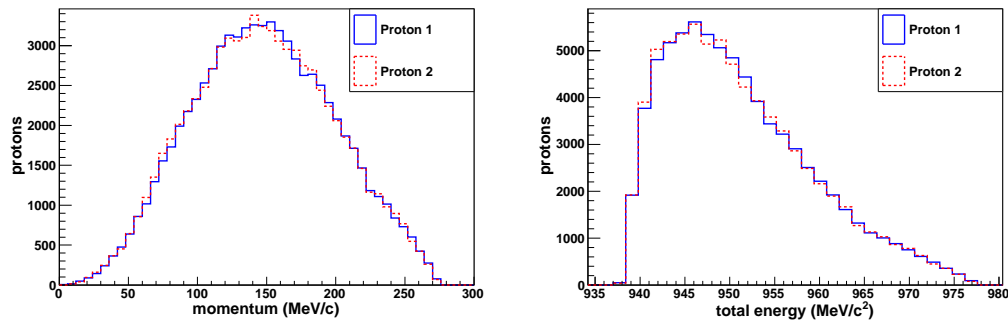


**Figure 5.2:** Kinematics of decay protons in simulated  $^{16}\text{O}(pp) \rightarrow ^{14}\text{C} K^+ K^+$  events. The momentum (left) and total energy (right) of the first (solid lines) and second (dashed lines) protons.

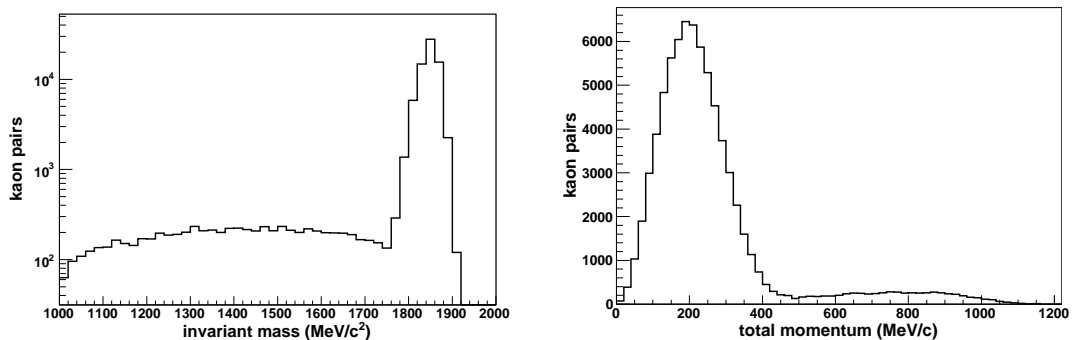


**Figure 5.3:** Kinematics of outgoing kaons in simulated  $^{16}\text{O}(pp) \rightarrow ^{14}\text{C} K^+ K^+$  events. The invariant mass (left), and total momentum (right) are shown.

The final task of the intra-nuclear simulation is to propagate the kaons through the nuclear environment. It is possible, for example, that a kaon may undergo charge exchange ( $K^+n \rightarrow K^0p$ ) before exiting the parent nucleus in which the dinucleon decay took place. The kaon is stepped through the nucleus by increments of 0.07 fm, and at each step the cross-sections for charge exchange, elastic, and inelastic interactions are calculated using the model of Oset, *et al.* [73].

The distance that the kaon travels through the nuclear environment is determined by the location of the dinucleon decay point within the nucleus. A Woods-Saxon distribution is used to determine the dinucleon decay point:

$$\rho(r) = \frac{\rho(0)}{1 + \exp\left(\frac{r-a}{b}\right)}, \quad (5.1)$$

where  $\rho(r)$  is the nuclear density as a function of  $r$ , the radial distance from the center of the nucleus,  $a = 1.07A^{1/3} = 2.69$  fm is the maximum radius for  $^{16}\text{O}$ , and  $2b = 0.82$  fm is the thickness of the nuclear surface

Charge exchange of the  $K^+$  is considered an intrinsic source of inefficiency in this search. In the simulation, charge exchange occurred inside the parent nuclear environment with a frequency of 0.05% per kaon.

## 5.2 Extra-Nuclear Simulation

In the next stage of the Monte Carlo simulation, the kinematic vectors of the kaons calculated from the intra-nuclear simulation are used as the inputs to the official Geant3-based Super-Kamiokande Monte Carlo software. The kaons are propagated through the detector, and hadronic interactions, ionization energy loss, Cherenkov light production, subsequent particle decays, and detector response are all simulated. See Section 4.4 for more details on the Super-Kamiokande detector simulation.

The hadronic interaction cross-section for  $K^+$  calculated from the simulation is shown in Fig. 5.4. The types of interactions that were simulated are listed in Table 4.1. The most important types of hadronic interactions that were simulated were elastic and inelastic interactions, charge exchange,  $\Sigma$  creation, and  $\Lambda$  creation. The latter three were sources of intrinsic inefficiency in this search, as they destroy the  $K^+$  state

before it has a chance to decay. The simulated dinucleon decay kaons underwent charge exchange in water at a rate of about 10% per kaon.  $\Sigma$  creation and  $\Lambda$  creation occurred at a rate of about 1% and .5% per kaon, respectively.

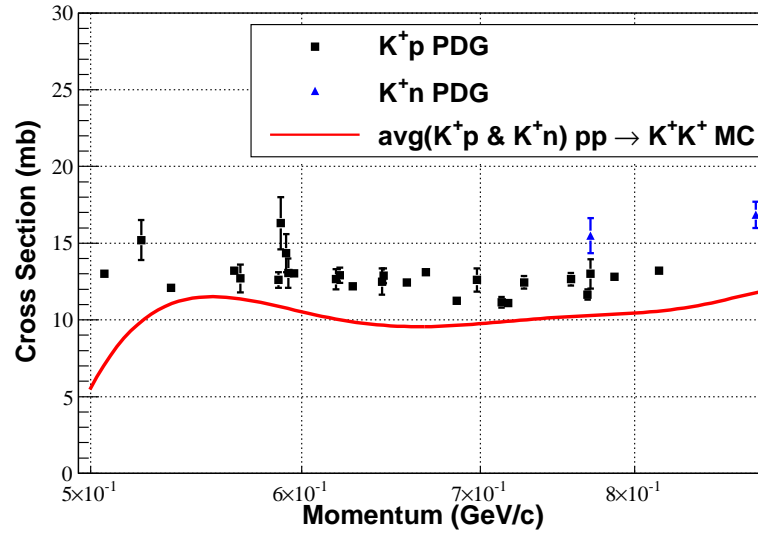


**Figure 5.4:** Kaon-nucleon interaction cross-section calculated from the  $^{16}\text{O}(pp) \rightarrow ^{14}\text{C} K^+ K^+$  Monte Carlo overlaid on  $K^+ - p$  and  $K^+ - n$  cross sections taken from the PDG [12].

## Chapter 6

# Data Reduction Process

The data reduction process separates events caused by interesting physical phenomena from events induced by uninteresting incidental sources, such as radioactivity in and around the walls or cosmic ray muons. Before reduction, there are on the order of  $10^6$  events ( $\approx 10$  gigabytes of data) recorded per day. Low energy triggers comprise the majority of these events, occurring at a rate of about 11 Hz. Cosmic ray muons dominate the high energy triggers, occurring at a rate of about 3 Hz.

The physically interesting events are categorized as either fully contained (FC), partially contained (PC) or upward going muons (UPMU). This search is concerned only with the FC events, thus only the FC reduction process is described here. FC reduction is performed by a five step automated process. The description of the PC and UPMU reduction processes is beyond the scope of this thesis, but may be read about in further detail in [57].

### 6.1 First Reduction

The first reduction step aims to remove events from cosmic ray muons and radioactive decays. The cuts in the step must be robust and relatively loose, as it is

applied during the online data taking process.

The requirements for the first reduction are as follows:

- $PE_{300} \geq 200$ : The number of photoelectrons in the ID that fall within a 300 ns sliding window in time must be greater than 200.
- $NHITA_{800} \leq 50$ : The number of hits in the OD that fall within a fixed window in time running from 400 ns before the ID trigger to 400 ns after must be less than 50, or else the OD trigger must have been disabled at the time.
- $TDIFF \geq 100 \mu s$ : The time interval between the previous event and the current event must be greater than  $100 \mu s$ . This is to reject Michel electrons from the decay of stopping muons.

The event rate is reduced to about 3000 events per day after the first reduction stage.

## 6.2 Second Reduction

The aim of the second reduction stage is the same as that of the first with the additional goal of removing flasher events, which are events caused by flashing PMTs. Essentially the same cuts are applied, but in this stage they are slightly tighter. The second reduction process and all later reduction processes are applied offline.

- $PE_{max}/PE_{300} < 0.5$ : here  $PE_{max}$  is the maximum number of photoelectrons collected by a single PMT in a given event, and  $PE_{300}$  is the same quantity as defined in the first reduction process. This cut removes flasher events.

- $NHITA_{800} \leq 25$  if  $PE_{total} < 100000$  **p.e.:** Where  $PE_{total}$  is the total number of photoelectrons collected in the ID. As in the first reduction stage, this cut may be circumvented if the OD trigger was disabled at the time.

## 6.3 Third Reduction

The goal of the third reduction stage is similar to that of the first two, however the cuts and tools used in this stage are more elaborate than before. The third reduction stage is broken up into six sub-stages:

- **through-going muon cut**
- **stopping muon cut**
- **cable hole muon cut**
- **flasher cut**
- **accidental muon cut**
- **low energy muon cut**

### 6.3.1 Through-Going Muon Cut

Through-going cosmic ray muons enter and exit the detector, leaving behind a substantial amount of charge in the ID along with a cluster of charge at both the entrance and exit points in the OD. A special muon fitter is used to make the following through-going muon cuts.

Events which satisfy the following criteria are categorized as through-going muon events and are rejected:

- $PE_{max} > 250$  **p.e.:** If a PMT in the ID collected more than 250 p.e., then the following cuts are applied.
- $mugood > 0.75$ : The goodness value from the special muon fitter must be greater than 0.75.
- $NHITA_{in} \geq 10$  **or**  $NHITA_{out} \geq 10$ : The number of hit OD PMTs inside an 800 ns time window and located within 8 m of the entrance (in) or exit (out) point must be greater than 10.

### 6.3.2 Stopping Muon Cut

The special muon fitter is again used in the stopping muon cut.

Events which satisfy the following criteria are categorized as stopping muon events and are rejected:

- $\{mugood > 0.5$  **and**  $NHITA_{in} \geq 5\}$  **or**  $NHITA_{in} \geq 10$ : Where the same definitions from the through-going muon cut are used.

### 6.3.3 Cable Hole Muon Cut

This cut removes cosmic ray muons which penetrate the detector through the cable holes used to run cable bundles down to the PMTS. When this happens, little to no signal is left in the OD, thus making the standard through-going or stopping muon cuts ineffective. The cable hole muon cuts are as follows:

Events which satisfy the following criteria are categorized as cable hole muon events and are rejected:

- $NHITA > 1$ : There must be at least one hit in the OD.

- $l_{veto} < 4$  m: The distance between the vertex and the cable hole ( $l_{veto}$ ) must be less than 4 m.

### 6.3.4 Flasher Cut

Flasher events occur when there is a discharge from the dynode of a PMT. They are characterized by their unusually wide timing distribution.

Events which satisfy the following criteria are categorized as flasher events and are rejected:

- $NMIN_{100} \geq 14$  **or**  $NMIN_{100} \geq 10$  **if**  $NHIT_{ID} < 800$ : Where  $NMIN_{100}$  is the minimum number of hit ID PMTs in a 100 ns time window, and  $NHIT_{ID}$  is the total number of hit PMTs in the ID.

### 6.3.5 Accidental Muon Cut

Cosmic ray muons will occasionally enter the detector shortly after a low energy event, but within the same trigger gate. Because the light deposited in the OD from the muon is relatively late compared to the initial trigger timing, these accidental muon events require a special cut.

Events which satisfy the following criteria are categorized as accidental muon events and are rejected:

- $NHITA_{off} > 20$ : The number of hit OD PMTs in the 500 ns time window from 400 ns to 900 ns after the trigger must be greater than 20.
- $PE_{off} > 5000$  **p.e.:** The total number of photoelectrons collected in the ID in the same 500 ns time window as above must be greater than 5000.

### 6.3.6 Low Energy Muon Cut

Low energy events caused by radioactive decays and noise in the electronics are removed in this step.

Events which satisfy the following criteria are categorized as accidental muon events and are rejected:

- $NHIT_{50} < 50$ : The number of hit ID PMTs within a 50 ns sliding window in time must be less than 50. The residual hit time of each PMT is used, which takes into account the time of flight of the photons from a single vertex point. The vertex is defined here as the point which most strongly peaks the residual time distribution. 50 PMT hits roughly correspond to a 9 MeV event.

At the end of the third reduction stage, the event rate has been reduced to 45 events per day.

## 6.4 Fourth Reduction

The fourth reduction stage is dedicated to removing the remaining flasher events. An important characteristic of flasher events is that the light pattern created in these events tends to be repeated over long periods of time. This repetition is exploited in the fourth reduction process, which is explained in further detail in [57].

The event rate has been reduced to about 18 events per day after applying the fourth reduction stage.

## 6.5 Fifth Reduction

The fifth and final stage in the FC reduction process is designed to remove various remaining cosmic ray muon and flasher events. It consists of four steps:

- final stopping muon cut
- invisible muon cut
- final accidental muon cut
- long tail flasher cut

### 6.5.1 Final Stopping Muon Cut

This cut is similar to the stopping muon cut applied earlier during the third reduction stage, but in this step the entrance point is now computed by extrapolating backward along the fitted track of the muon, rather than using the earliest hit PMT.

Events which satisfy the following criteria are categorized as stopping muon events and are rejected:

- $NHITA_{in} \geq 5$ : Where  $NHITA_{in}$  is defined as before.

### 6.5.2 Invisible Muon Cut

This cut targets muons which are below Cherenkov threshold (hence “invisible”), but emit a decay electron in the detector which can be seen.

Events which satisfy the following criteria are categorized as invisible muon events and are rejected:

- $PD_{total} < 1000$ : The total number of photoelectrons in the ID is less than 1000.

- $NHITA_{early}^{max} > 4$ : The maximum number of hit OD PMTs in a 200 ns time window allowed to move from 100 ns before the trigger to 8900 ns after the trigger is greater than 4.
- $NHIA_{early}^{max} + NHITA_{500} > 9$  if  $l_{cluster} < 500$  cm **or else**  $NHITA_{early} > 9$ : Where  $NHITA_{500}$  is the number of hit OD PMTs in a 500 ns time window from  $-100$  ns to 400 ns, and  $l_{cluster}$  is the distance between the two OD clusters used during the calculation of  $NHITA_{early}$  and  $NHITA_{500}$ .

### 6.5.3 Final Accidental Muon Cut

The final accidental muon cut further eliminates muons which accidentally sneak in after a low energy event.

Events which satisfy the following criteria are categorized as accidental muon events and are rejected:

- $PE_{500} < 300$  **p.e.:** The total number of photoelectrons in the ID within a 500 ns time window from  $-100$  ns to 400 ns must be less than 300.
- $NHITA_{late}^{max} > 20$ : The number of hit OD PMTs in a 200 ns sliding time window allowed to move from 400 ns to 1600 ns after the trigger must be greater than 20.

### 6.5.4 Long Tail Flasher Cut

The long tail flasher cut is similar to the flasher cut applied during the third reduction phase, but with tighter cut values.

Events which satisfy the following criteria are categorized as long tail flasher events and are rejected:

- $NMIN_{100} > 5$  if  $GOOD_{point} < 0.4$ : The minimum number of hit ID PMTs in a 100 ns sliding time window allowed to move from 300 ns to 800 ns after the trigger gate must be greater than 5 if the goodness of the point fit,  $GOOD_{point}$ , is greater than 0.4.

After applying the fifth reduction process, the event rate has been reduced to about 16 events per day.

## 6.6 Final Reduced Data Sample

Approximately 16 events per day remain in the data after applying all five of the FC reduction processes. Three final cuts are applied to reduce the data even further to create the final sample:

- $NHITAC < 10$ : The number of OD PMT hits in the cluster with the highest charge must be less than 10.
- $EVIS > 30$  MeV: The total amount of visible energy must be greater than 30 MeV, where the visible energy is defined as the sum of the energy of each ring when assuming all rings to have been produced by electrons.
- $WALL > 200$  cm: The distance from the vertex point to the nearest wall must be greater than 200 cm. This is the fiducial volume (FV) cut.

The above cuts reduce the final event rate in the data to about 8.2 events per day. The contamination from undesired backgrounds in the data at this stage, such as cosmic ray muons and flashers, is estimated to be negligible ( $< 1\%$ ). The estimated efficiency of the reduction process for both atmospheric neutrino events and dinucleon

Reduction Stage	Events per Day
Pre-Reduction	1,200,000
First Reduction	3,000
Second Reduction	200
Third Reduction	45
Fourth Reduction	16
Final Reduction (FV)	8.2

**Table 6.1:** Event rates in the data after each stage of the fully contained reduction process.

decay events is about 99.9%. Table 6.1 summarizes the event rates at each stage of the reduction process.

## Chapter 7

# Physics Reconstruction

Reconstruction on a ring-by-ring basis was done in a two-step, bootstrapping process. First, the standard Super-Kamiokande event reconstruction algorithm was applied. From this, the reconstructed event vertex, ring directions, and Cherenkov angles were used as inputs for the second step of ring reconstruction, which utilized a custom built algorithm suitable for identifying multiple particle vertices in a single event. The name of the second reconstruction algorithm is MVFIT, for multiple vertex fitter.

## 7.1 Standard Reconstruction Algorithm

The standard Super-Kamiokande event reconstruction software is made of several specialized algorithms that combined make up the full reconstruction process. The algorithms are listed below in sequential order:

### (1) Vertex Position and Ring Direction

Calculates a single event vertex based on the point where the residual timing distribution of hit PMTs has the sharpest peak. Also calculates the direction

and Cherenkov angle of the dominant ring.

(2) Ring Counting

Additional rings are searched for using a likelihood method. The event vertex position and direction of the dominant ring calculated in the previous step are used in the calculation. The total number of rings is determined in this step.

(3) Showering Likelihood

A showering likelihood variable is calculated for all rings in the event based on the ring's opening angle and a comparison between the observed light pattern and the expected light patterns for showering and non-showering particle types.

(4) Ring Momentum

The momentum of each ring is calculated by comparing the amount of charge accumulated inside a  $70^\circ$  cone with respect to the ring's direction. A look-up table based on MC simulations and detector calibration is used for the conversion from charge to momentum. The observed charge in each PMT is also divided up into separate rings in this step.

(5) Ring Number Correction

Possible fitting mistakes are corrected by eliminating rings of very low momentum that overlap with other more energetic rings.

(6) Decay Electron Finding

Rings from decay electrons following the primary event are identified.

### 7.1.1 Vertex Position and Ring Direction

There are three parts in the initial event vertex position and dominant ring fitting procedure: (1) point fit, (2) direction fit, and (3) TDC fit.

#### Point Fit

The event vertex position estimation is performed with the assumption that all of the light observed in the detector was emitted simultaneously from a single point source. To find the point that best matches this hypothesis, a three-dimensional grid of test points throughout the volume of the ID is considered, and the single best of these points is kept. Then the process is repeated with a finer granularity in a small region around the best point of the previous granularity level.

The best test point in the grid is determined by maximizing a goodness calculation, which is based on the hit times of the PMTs. The point fit goodness is defined as follows:

$$G_{point} = \frac{1}{N_{hit}} \sum_i \exp \left( -\frac{(t_i - \bar{t})^2}{2(a \times \sigma_t)^2} \right), \quad (7.1)$$

where  $N_{hit}$  is the total number of hit PMTs,  $\sigma_t$  is the timing resolution of the PMTs (2.5 ns),  $a = 1.5$  is a factor to crudely account for light scattering, and  $\bar{t}$  represents the average value of the residual times of the PMTs,  $t_i$ , which are defined:

$$t_i = t_i^0 - \frac{d_i}{v(d_i, q_i)}, \quad (7.2)$$

where  $t_i^0$  is the recorded absolute time of the PMT hit,  $d_i$  is the distance from the test vertex point to the PMT, and  $v$  is the effective velocity of light in water as a function of  $d_i$  and the recorded charge,  $q_i$ , accounting for wavelength and acceptance effects.

This vertex fitting algorithm is guided by the assumption that all light in the event was originated simultaneously from the same point. In cases where this is not true, however, the reconstructed event vertex found by the point fit algorithm will tend to approximate an “average” event vertex (*e.g.*, a point along the track over which a single muon radiates Cherenkov light, or a point between two spatially separated muons). The point fit vertex can still be safely used as a springboard for more accurate vertex fitting algorithms applied later in the reconstruction process, however.

### Direction Fit

In the next step, the direction and Cherenkov angle of the dominant ring is estimated. The initial direction guess is found by calculating a charge-weighted vector sum of all light in the detector using the event vertex found by the point fit in the previous step. From there, a directional test grid in  $(\theta, \phi)$  space is generated, analogous to the test grid in the vertex point fit. A goodness calculation is again used, this time to find the best direction in the grid, along with the best Cherenkov opening angle.

The goodness used in the directional fit is defined as follows:

$$G_{dir} = \frac{\int_0^{\theta_C} Q(\theta) d\theta}{\sin \theta_C} \exp \left( -\frac{(\theta_C - \theta_{max})^2}{\sigma_a^2} \right), \quad (7.3)$$

where  $\theta_C$  is the test opening angle (allowed to vary),  $Q(\theta)$  is the charge distribution as a function of angle relative to the test direction,  $\theta_{max} = 42^\circ$  is the maximum Cherenkov angle assuming the particle’s velocity  $\beta = 1$ , and  $\sigma_a$  is the estimated rms spread of PMT hits around  $\theta_C$ . The test direction and opening angle which yield the maximum goodness are taken as the best fit.

## TDC Fit

The purpose of the TDC fitting step is to more precisely fit the vertex position by taking into account the finite track length of a massive charged particle and the effect of indirect light caused by scattered Cherenkov photons. The vertex, ring direction, and Cherenkov angle of the dominant ring found in the point fit and direction fit steps are used as inputs to this step.

In this step, a modified residual time calculation for the PMT hits inside the Cherenkov cone is used:

$$t_i = t_i^0 - \frac{1}{c} |\vec{X}_i - \vec{O}| - \frac{n}{c} |\vec{P}_i - \vec{X}_i|, \quad (7.4)$$

where  $\vec{O}$  is the test vertex position,  $\vec{X}_i$  is the position along the track where photons would be emitted toward the  $i$ -th PMT,  $n$  is the index of refraction for water,  $\vec{P}_i$  is the position of the  $i$ -th PMT, and  $t_i^0$  is the recorded absolute time of the hit of the  $i$ -th PMT.

The goodness for PMTs inside ( $G_I$ ) and outside ( $G_O$ ) the Cherenkov cone are calculated slightly differently, as shown below:

$$G_I = \sum_i \frac{1}{\sigma_i^2} \exp \left( -\frac{(t_i - \bar{t})^2}{2(a \times \bar{\sigma})^2} \right), \quad (7.5)$$

$$G_O = \sum_i \frac{1}{\sigma_i^2} \max \left[ \exp \left( -\frac{(t_i - \bar{t})^2}{2(a \times \bar{\sigma})^2} \right), 0.8 \exp \left( -\frac{t_i - \bar{t}}{20 \text{ ns}} \right) \right], \quad (7.6)$$

where  $\sigma_i$  is the timing resolution of the  $i$ -th PMT,  $\bar{\sigma}$  is the average PMT timing resolution,  $a = 1.5$  is a factor to account for indirect scattered light,  $t_i$  is the residual time of the  $i$ -th PMT,  $\bar{t}$  is the average residual time of the PMTs, and 20 ns is the average time difference between direct and scattered light. The  $G_I$  goodness value

and the  $G_O$  goodness value are calculated separately for PMT hits inside ( $\theta_i < \theta_C$  or  $t_i < \bar{t}$ ) and outside ( $\theta_i > \theta_C$  or  $t_i > \bar{t}$ ) of the Cherenkov opening angle, corresponding to the direct and scattered light, respectively.

The final overall goodness for the test vertex position is then calculated using both  $G_I$  and  $G_O$ , as shown below:

$$G_{total} = \frac{G_I + G_O}{\sum_i \sigma_i}. \quad (7.7)$$

The track length used in the calculation is estimated by summing the charge within  $70^\circ$  of the direction of the ring and then calculating the corresponding muon momentum required to produce that amount of light. Using this track length, the total goodness,  $G_{total}$ , is maximized as a function of vertex position and ring direction. Then the procedure is repeated, calculating a new track length and varying the vertex position and ring direction to maximize the total goodness once again. This is repeated in an iterative process until a final, stable fit is reached.

The resolution of the TDC fit vertex, determined by the distance between the reconstructed vertex position and the true vertex position of Monte Carlo events, is shown in Fig. 7.1 for various subsamples of single-ring atmospheric neutrino events. The resolution falls between 50 cm and 90 cm, depending on the sample.

### 7.1.2 Ring Counting

After fitting an event vertex and identifying the dominant ring, the ring counting algorithm is applied to search for other possible rings in the event. There are two basic steps to the ring counting procedure: (1) search for ring candidates and (2) test the best candidate found in step (1). If the ring candidate passes the test in step (2), it is removed from the search map and the process is repeated from step (1) again.

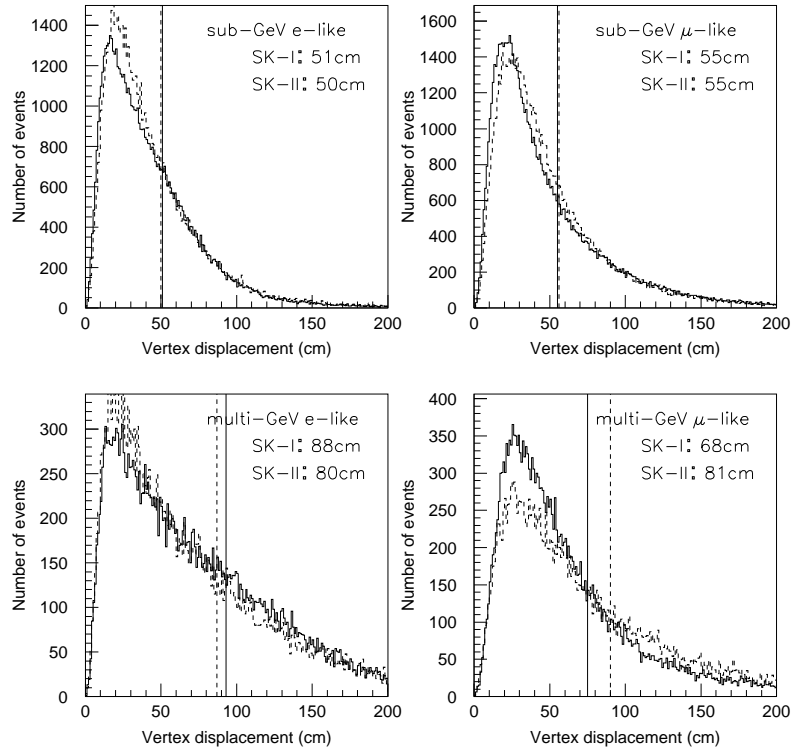


**Figure 7.1:** Distance between the TDC fit reconstructed vertex and the event true vertex for sub- GeV ( $<1.33$  GeV) and multi- GeV ( $>1.33$  GeV) single-ring atmospheric neutrino Monte Carlo events.

This continues until all ring candidates fail the test in step (2).

## Ring Candidate Search

To search for ring candidates, a Hough transform is applied to the PMT hits. This involves first mapping the PMT hits in  $(\theta, \phi)$  space relative to the event vertex and dominant ring direction. Then, the charge in each hit is distributed uniformly along a virtual circle corresponding to a projection of a cone with a  $42^\circ$  half-opening angle centered on the position of the hit PMT itself. This results in the accumulation of charge at the center of a true Cherenkov ring, where the Hough-transformed charge

distributions overlap the most. See Fig. 7.2 for an illustration of this concept.

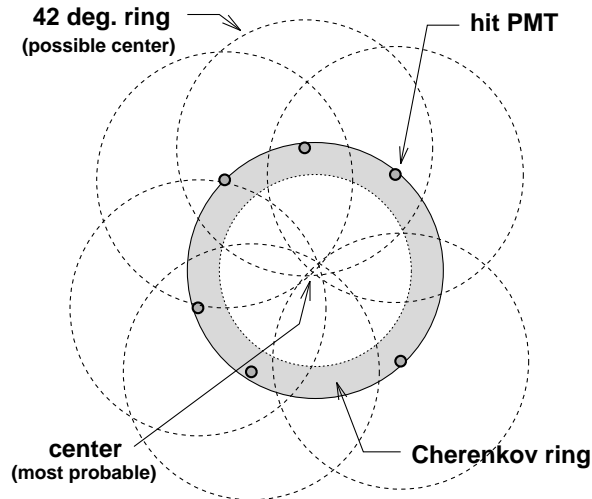


**Figure 7.2:** The basic concept of the Hough Transform. The charge in a PMT is distributed along a circle corresponding to a  $42^\circ$  Cherenkov opening angle as seen from the event vertex. The circles of the hit PMTs from the same Cherenkov ring will then overlap in the center of the actual ring.

In practice, virtual circles are not actually drawn out, but instead an expected charge distribution function  $f(\theta)$  is mapped out for each hit PMT, weighted by the observed charge distribution. When plotted in a 2-D histogram, the ring directions become visible as peaks of charge as shown in Fig. 7.3.

### Ring Candidate Test

After identifying the candidate rings, they are tested through the use of a log-likelihood method. If there are  $N$  rings already confirmed to be good candidates in the event, then the  $(N + 1)$ -th candidate ring is tested for its validity.

The ring candidate test likelihood is defined as follows:

$$F = \sum_i^5 \{ \log [(P_i)_{N+1}] - \log [(P_i)_N] \}, \quad (7.8)$$

where  $P_i$  is the probability density function for the  $i$ -th evaluation function. So,

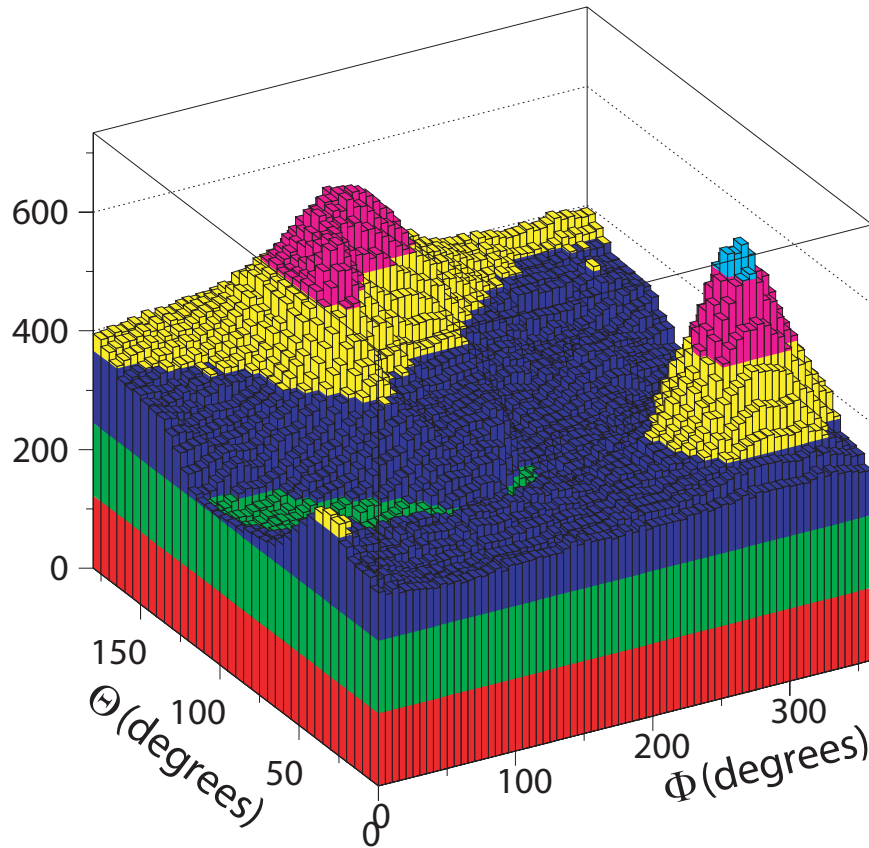


**Figure 7.3:** A two dimensional histogram of a Hough transformed charge distribution. Two distinct charge peaks can be seen, corresponding to the directions of two candidate Cherenkov rings in the event.

$P_{N+1}$  and  $P_N$  are the probability functions for the event to have  $(N + 1)$  and  $N$  rings, respectively. Note that the algorithm is limited to a maximum of five rings in an event.

The following quantities are used in determining the evaluation functions:

- The difference of  $L(N + 1) - L(N)$
- The average value of the expected charge from the  $(N + 1)$ -th ring near the edges of the  $N$  confirmed Cherenkov rings
- The average value of the expected charge outside the  $(N + 1)$ -th ring

- The residual charge left after subtracting the expected charge from the  $N$  confirmed rings
- The difference between the charge in peak of the candidate ring and the average charge inside and outside the candidate ring

Here, the function  $L(N)$  is defined:

$$L(N) = \sum_i \log \left( \text{prob} \left( q_i^{\text{obs}}, \sum_{n=1}^N \alpha_n \cdot q_{i,n}^{\text{exp}} \right) \right), \quad (7.9)$$

where  $\text{prob}(q_i^{\text{obs}}, q_i^{\text{exp}})$  is the probability of detecting  $q_i^{\text{obs}}$  given the expected value of  $q_i^{\text{exp}}$ . The probability density functions were determined using Monte Carlo studies.

### 7.1.3 Showering Likelihood

The showering likelihood algorithm is intended to separate rings into two different types: a showering type and a non-showering type. The former type describes the diffused ring patterns created by electrons, positrons and gamma-rays due to the effects of electromagnetic showering and multiple scattering. See Fig. 7.4 for an example of how a showering ring appears in the event display. The latter type describes the sharper-edged ring patterns generated by more massive charged particles, such as muons and charged mesons, including kaons. See Fig. 7.5 for an example of how a non-showering ring appears in the event display.

The Cherenkov opening angle provides another feature of distinction between showering and non-showering rings. The Cherenkov angle is expected to always be maximal ( $42^\circ$ ) for the lighter, showering type particles, but it may be smaller for more massive particles if they are not traveling at highly relativistic speeds or after they have lost energy through ionization. The fuzziness or crispness of the light pattern

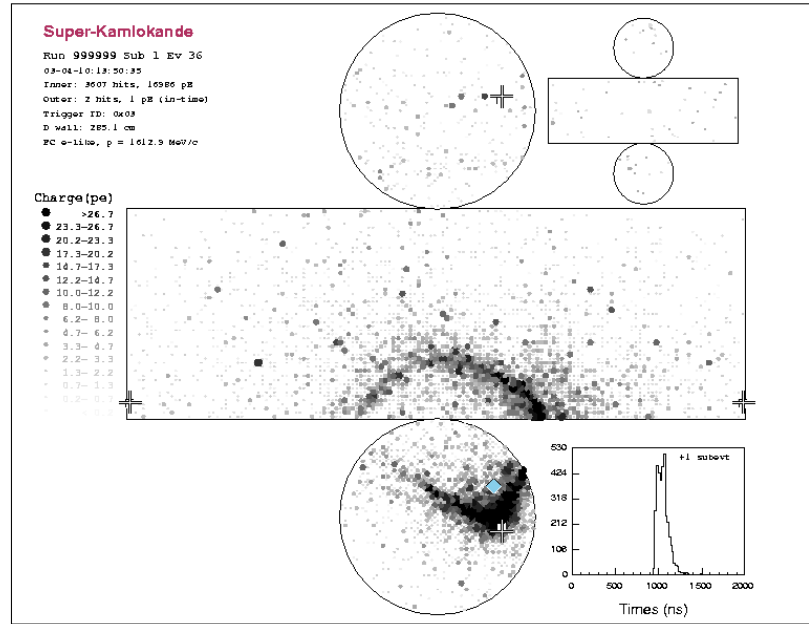


Figure 7.4: Example of a showering ring.

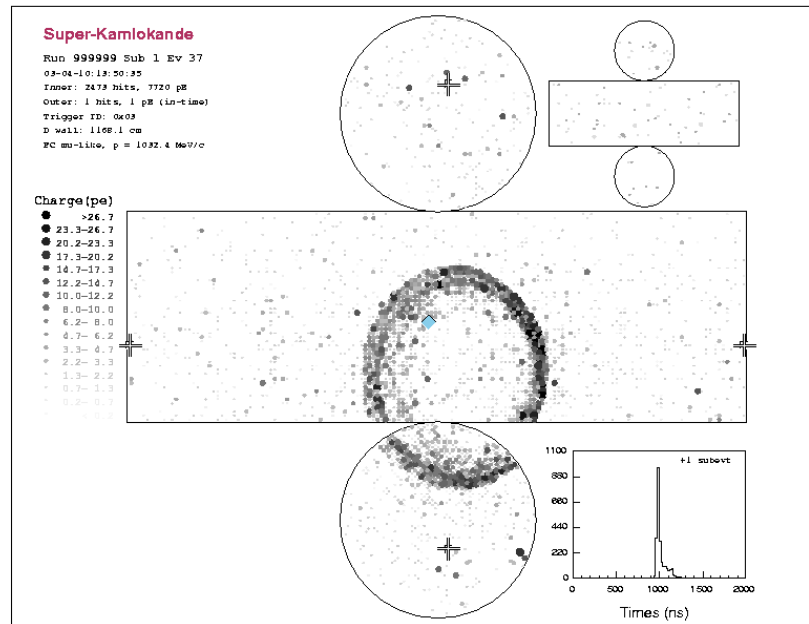


Figure 7.5: Example of a non-showering ring.

and the Cherenkov opening angle are both exploited simultaneously by the showering likelihood algorithm.

The showering likelihood calculation depends on the ability to formulate expected charge distributions for the two ring type hypotheses. The details of those expected charge distributions will be explained first, followed by the description of the likelihood itself.

### Expected Charge Distributions

The expected charge distributions describe the amount of charge expected to be seen in in each PMT given that the ring was produced by an electron ( $q^{\text{exp}}(e)$ ) to represent the showering type, or a muon ( $q^{\text{exp}}(\mu)$ ) to represent the non-showering type. They are defined as:

$$q_i^{\text{exp}}(e) = \alpha_e Q^{\text{exp}}(p_e, \theta_i) \left( \frac{R}{r_i} \right)^{1.5} \frac{1}{\exp(\frac{r_i}{L})} f(\Theta_i) + q_i^{\text{scat}}, \quad (7.10)$$

$$q_i^{\text{exp}}(\mu) = \left( \alpha_\mu \frac{\sin^2 \theta_{x_i}}{r_i (\sin \theta_{x_i} + r_i \cdot \frac{d\theta}{dx} |_{x=x_i})} + q_i^{\text{knock}} \right) \frac{1}{\exp(\frac{r_i}{L})} f(\Theta_i) + q_i^{\text{scat}}, \quad (7.11)$$

where:

- $\alpha_e, \alpha_\mu$  : normalization factors
- $r_i$  : distance from the vertex to the  $i$ -th PMT
- $\theta_i$  : opening angle between the  $i$ -th PMT direction and the ring direction
- $L$  : light attenuation length in water
- $f(\Theta_i)$  : correction for the PMT acceptance as a function of the photon incidence angle  $\Theta_i$
- $R$  : radius of the virtual sphere (16.9 m)
- $Q^{\text{exp}}(p_e, \theta_i)$  : expected p.e. distribution from an electron as a function of the the electron momentum and the opening angle
- $x$  : position of the muon along its track
- $x_i$  : position of the muon along its track where Cherenkov photons are emitted toward the  $i$ -th PMT
- $q_i^{\text{scatt}} (q_i^{\text{knock}})$  : expected p.e.s for the  $i$ -th PMT from scattered photons (knock-on electrons)
- $\theta (\theta_{x_i})$  : Cherenkov opening angle of the muon at track position  $x (x_i)$

The expected p.e. distribution distribution for an electron,  $Q^{\text{exp}}(p_e, \theta_i)$ , was obtained through Monte Carlo studies. Note that scattered photons are accounted for as well as direct photons by  $q_i^{\text{scat}}$ .

The expected p.e. distribution for a muon is calculated analytically. The  $\sin^2 \theta$  dependence arises from the Cherenkov angle dependence of the intensity of the Cherenkov photons. The term  $r(\sin \theta + r(d\theta/dx))$  takes into account the shrinking size of the

Cherenkov angle as the particle loses momentum while it travels through the water.

### Likelihood Calculation

The showering ( $e$ -like) and non-showering ( $\mu$ -like) likelihood functions for the  $n$ -th ring are defined as:

$$L_n(e, \mu) = \prod_{\theta_i < (1.5 \times \theta_C)} \text{prob} \left( q_i^{\text{obs}}, q_{i,n}^{\text{exp}}(e, \mu) + \sum_{n' \neq n} q_{i,n'}^{\text{exp}} \right), \quad (7.12)$$

where the product is over the PMTs inside the Cherenkov cone of the  $n$ -th ring ( $1.5 \times \theta_C$ ).  $q_i^{\text{obs}}$  is the number of observed p.e.s in the  $i$ -th PMT,  $q_{i,n}^{\text{exp}}(e \text{ or } \mu)$  is the expected number of p.e.s in the  $i$ -th PMT coming from the  $n$ -th ring when assuming the  $n$ -th ring was produced by either an electron or a muon.  $q_{i,n'}^{\text{exp}}$  is the same quantity, only from the  $n'$ -th ring. The function  $\text{prob}(q_i^{\text{obs}}, q_i^{\text{exp}})$  gives the probability of detecting  $q_i^{\text{obs}}$  p.e.s in the  $i$ -th PMT given the expected amount,  $q_i^{\text{exp}}$ . The  $q_{i,n}^{\text{exp}}(e)$  and  $q_{i,n}^{\text{exp}}(\mu)$  expectation values are optimized by altering the direction and opening angle of the  $n$ -th ring to yield the maximum likelihood value.

The likelihood is translated into a  $\chi^2$  parameter to allow it to be combined with another estimator that uses the Cherenkov opening angle. The  $\chi^2$  value is shown below:

$$\chi_n^2(e, \mu) = -2 \log L_n(e, \mu) + \text{const.} \quad (7.13)$$

The probability for a ring to be of a particular type based on the light pattern is then given by the following:

$$P_n^{\text{pattern}}(e, \mu) = \exp \left( -\frac{(\chi_n^2(e, \mu) - \min[\chi_n^2(e), \chi_n^2(\mu)])^2}{2\sigma_{\chi_n^2}^2} \right), \quad (7.14)$$

where  $\sigma_{\chi_n^2}^2 = \sqrt{2N}$  is the approximate resolution of the  $\chi^2$  distribution,  $N$  being the number of PMTs used in the calculation.

The probability for a ring to be of a particular type based on the Cherenkov opening angle is given by:

$$P_n^{\text{angle}}(e, \mu) = \exp\left(-\frac{(\theta_n^{\text{obs}} - \theta_n^{\text{exp}}(e, \mu))^2}{2(\delta\theta_n)^2}\right), \quad (7.15)$$

where  $\theta_n^{\text{obs}}$  and  $\delta\theta_n$  are the reconstructed opening angle of the  $n$ -th ring and the fitting error, respectively, and  $\theta_n^{\text{exp}}(e \text{ or } \mu)$  is the expected opening angle of the  $n$ -th ring based on the reconstructed electron-like or muon-like momentum.

The final probability calculation is simply the product of the light pattern probability calculation and the Cherenkov angle probability calculation:

$$P(e, \mu) = P^{\text{pattern}}(e, \mu) \times P^{\text{angle}}(e, \mu). \quad (7.16)$$

The final showering likelihood variable used to determine whether a ring is of a showering or non-showering type is defined as:

$$L_{\text{show}} \equiv \sqrt{-\log P(\mu)} - \sqrt{-\log P(e)}. \quad (7.17)$$

Positive values of  $L_{\text{show}}$  indicate a preference for the non-showering type, and negative values indicate a preference for the showering type.

### 7.1.4 Ring Momentum

To calculate the momentum of the particle which produced the Cherenkov ring, the integrated charge within a  $70^\circ$  half-opening angle is used. This integrated charge is called *RTOT*, and is described below:

$$RTOT_n = \frac{G_{MC}}{G_{data}} \left( \alpha \sum_{\substack{\theta_{i,n} < 70^\circ \\ -50 \text{ ns} < t_i < 250 \text{ ns}}} \left( q_{i,n}^{\text{obs}} \exp\left(\frac{r_i}{L}\right) \frac{\cos \Theta_i}{f(\Theta_i)} \right) - \sum_{\theta_{i,n} < 70^\circ} S_i \right), \quad (7.18)$$

where:

$\alpha$  : normalization factor

$G_{\text{data}}, G_{\text{MC}}$  : relative PMT gain parameter for data and MC

$\theta_{i,n}$  : opening angle between  $n$ -th ring direction and  
 $i$ -th PMT direction

$t_i$  : residual (= time of flight subtracted) hit time  
of  $i$ -th PMT

$L$  : light attenuation length of water

$r_i$  : distance from vertex position to  $i$ -th PMT

$f(\Theta_i)$  : correction function for PMT acceptance as a  
function of photon incidence angle  $\Theta_i$

$S_i$  : expected amount of p.e.s from scattered pho-  
tons for  $i$ -th PMT

The summation is restricted to a time window spanning  $-50$  ns to  $+250$  ns, where  $0$  ns represents the peak of the residual hit time distribution. The purpose of this window is to exclude light that may have originated from muon-decay electrons created by muon decay.

After determining the  $RTOT$  value of a ring, the corresponding momenta for various particle hypotheses is calculated by linearly extrapolating between points on the look-up table shown in Fig. 7.6. This typically means finding the showering-like

momentum (equivalent value for electron, positron, or gamma), and the muon-like momentum. For the purposes of this study, a third particle type was added to the list: the charged kaon. To generate the points in the look-up table, Monte Carlo simulations of single ring events for each of the particle types were generated at various true momentum values, and the mean RTOT value for the corresponding true momentum was calculated and entered into the table. The kaon points were generated specially for this study.

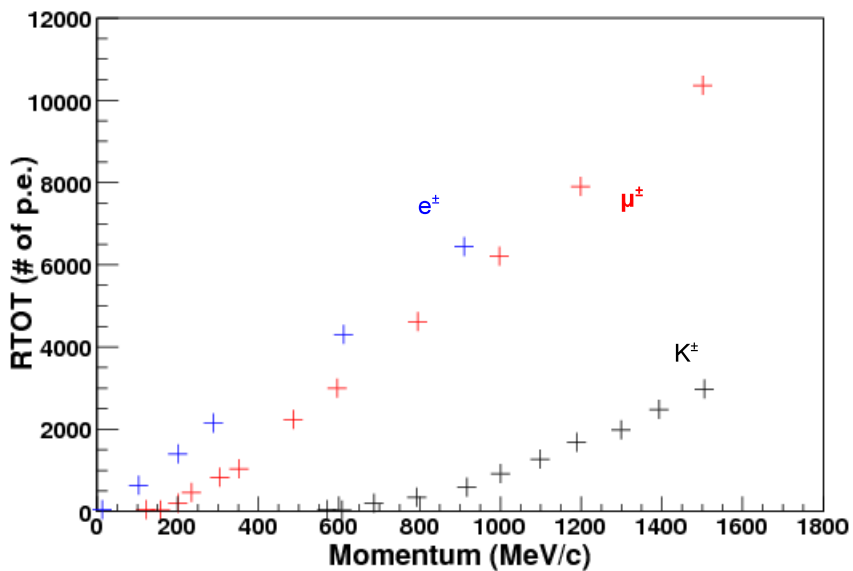


**Figure 7.6:** *RTOT* - momentum look-up table. The blue, upper set of crosses are for electrons, the red, middle set of crosses are for muons, and the black, lower set of crosses are for charged kaons.

The energy scale stability of the detector was tested by observing the mean reconstructed energy of stopping cosmic ray muons and the decay electrons which they produced (see Section 3.7.3 for details). It varied within  $\pm 0.88\%$  during the SK-I runtime.

The absolute energy scale was adjusted separately by observing the number of photoelectrons generated by through-going cosmic ray muon events. A variety of

calibration data were used to check the scale, such as stopping cosmic ray muons, the decay electrons they produce, and the reconstructed invariant mass from  $\pi^0$  particles produced in atmospheric neutrino interactions. By comparing these data samples to Monte Carlo simulations, the absolute calibration error was estimated to be less than  $\pm 0.74\%$  for the SK-I data taking period.

### Ring Separation

In order to properly reconstruct the momenta of particles in a multi-ring event, the charge collected by the PMTs must be correctly divided amongst the different rings. This process is called ring separation. To perform the ring separation, a likelihood function is used which describes the likelihood of the charge observed in a given PMT to belong to a particular ring:

$$L = \sum_{\theta_{i',n} < 70^\circ} \log \left( \text{prob} \left( q_{i'}, \sum_{n'} \alpha_{n'} \cdot q_{i',n'}^{\text{exp}} \right) \right), \quad (7.19)$$

where  $q_{i'}$  is the observed amount of charge in the  $i'$ -th PMT,  $q_{i',n'}^{\text{exp}}$  is the expected amount of charge in the  $i'$ -th PMT coming from the  $n'$ -th ring,  $\text{prob}(q_i^{\text{obs}}, q_i^{\text{exp}})$  is the probability function for detecting  $q_i^{\text{obs}}$  charge in the  $i$ -th PMT given the total expected amount  $q_i^{\text{exp}}$ , and  $\alpha_{n'}$  is the scaling factor for each ring. The scaling factor is used as an optimization parameter, increasing or decreasing the amount of expected charge from each ring such that the total amount expected best matches the observed value.

The observed p.e.s in the  $i$ -th PMT belonging to the  $n$ -th ring are obtained as:

$$q_{i,n}^{\text{obs}} = q_i^{\text{obs}} \frac{\alpha_n \cdot q_{i,n}^{\text{exp}}}{\sum_{n'} \alpha_{n'} \cdot q_{i,n'}^{\text{exp}}}, \quad (7.20)$$

where the optimization parameters,  $\alpha_n$ , have been chosen to maximize  $L$ .

### 7.1.5 Ring Number Correction

Occasionally, a fake ring is identified and must be removed. To eliminate these rings, the ring number correction algorithm is applied. Ring number correction removes rings with a very small reconstructed momentum relative to any overlapping rings.

### 7.1.6 Decay Electron Finding

The reconstruction algorithm for finding and identifying decay electrons categorizes them in three ways:

- Sub-event type:

The decay electrons are observed in a separate event (sub-event).

- Primary-event type:

The decay electrons are observed in the primary event.

- Split type:

The decay electrons occurred around the end of the event timing window, and is recorded in the primary event and sub-event.

Sub-event type decay electron events require the following criteria:

- (1) The time interval from the end of a primary event is less than  $20 \mu\text{s}$ .
- (2) The total number of hit PMTs is greater than 50.
- (3) The goodness of the vertex fit is greater than 0.5.
- (4) The number of hit PMTs in a 50 ns time window is greater than 30.

(5) The total number of p.e.s is less than 2000.

(6) The number of hit PMTs in a 50 ns time window is greater than 60.

where the requirement of 60 hit PMTs in 50 ns corresponds to about 11 MeV of electron energy. The first criterion rejects gammas emitted from  $\mu^-$  captured on  $^{16}\text{O}$  nuclei.

Primary-event type decay electron events require another peak after the primary peak with more than 20 hits above the background level in a 30 ns time window.

Additional requirements for decay electron events are:

(7) the number of hit PMTs in a 30 ns time window is greater than 40 (primary-event and split types only)

(7)  $0.1 \mu\text{s} < \Delta t < 0.8 \mu\text{s}$  or  $1.2 \mu\text{s} < \Delta t < 20 \mu\text{s}$  (all types)

where  $\Delta t$  is the time between the primary peak and the decay electron peak. The final criterion rejects decays in the inefficient time interval around  $1 \mu\text{s}$ . The overall efficiency for detecting decay electrons is 80% for  $\mu^+$  and 63% for  $\mu^-$ .

## 7.2 Multiple Vertex Fitter

The MVFIT (multiple vertex fitter) algorithm is simple in principle. It first starts a loop over each ring found by the standard Super-Kamiokande event reconstruction algorithm used in the first step of ring reconstruction described in Section 7.1. As it considers each ring in turn, it masks all light outside of the ring's Cherenkov angle  $+10^\circ$  and subtracts any remaining light expected to have been contributed by other overlapping rings. Section 7.1.3 and Section 7.1.4 describe how the expected charge is calculated for each ring. With the masking applied, selected portions of the standard

Super-Kamiokande event reconstruction algorithm are then applied to the remaining light pattern, treating the unmasked light pattern as if it were actually from a single ring event. After one ring is considered, the masking is undone and the process is repeated for the next ring until all found rings in the event have been exhausted.

MVFIT reconstructs each ring according to three particle type hypotheses and records the reconstructed particle information from each of the three hypotheses for every ring in the event. These three particle hypotheses are (1) electromagnetic showering-type particles ( $e^\pm$  or  $\gamma$ ), referred to in this study as gamma-like, (2)  $\mu^\pm$ , referred to in this study as mu-like, and (3)  $K^\pm$ , referred to in this study as kaon-like.

A summary of the MVFIT procedure that is repeated for each ring is described below:

For each ring in an event:

- (1) Mask all light outside  $\theta_C + 10^\circ$
- (2) Subtract remaining expected light from overlapping rings
- (3) For each PID hypothesis (gamma-like, muon-like, and kaon-like):
  - (a) Apply the vertex position and ring direction reconstruction algorithm described in Section 7.1.1
  - (b) Apply the showering likelihood reconstruction algorithm described in Section 7.1.3
  - (c) Apply the ring momentum reconstruction algorithm described in Section 7.1.4
- (4) Store reconstructed variables for all three PID hypotheses
- (5) Unmask all light in the event; continue on to next ring

See Appendix A for the reconstructed variable resolutions obtained by MVFIT.

### 7.3 Reconstructed Ring Variables

By the end of the ring reconstruction process, each ring has associated with it a list of variables with values corresponding to all three of the potential PID hypotheses, along with the PID independent showering likelihood.

The final list of reconstructed ring variables is shown below:

1. Vertex Position (*kaon-like, muon-like, and gamma-like*)
2. Momentum (*kaon-like, muon-like, and gamma-like*)
3. Cherenkov Angle (*kaon-like, muon-like, and gamma-like*)
4. Direction (*kaon-like, muon-like, and gamma-like*)
5. Showering Likelihood (*PID independent*)

## Chapter 8

# Dinucleon Decay Signal

Before performing the search for dinucleon decay into kaons, three main decisions had to be made in order to limit the types of experimental signal that would be studied to a reasonably small set. The three decisions that ultimately defined the signal in this search were:

- Choice of dinucleon decay mode
- Choice of kaon decay modes
- Choice of Cherenkov ring combinations

Once the acceptable signal event types were narrowed down, a comprehensive list of descriptive characteristics was set down. This information then provided a platform for the search methodology described in Chapter 9.

### 8.1 Choice of Dinucleon Decay Mode

At first glance, there appear to be three dinucleon decay modes with final state kaons from which to choose:  $pp \rightarrow K^+ K^+$ ,  $pn \rightarrow K^+ K^0$ , and  $nn \rightarrow K^0 K^0$ . However, each  $K^0$  will decay with equal probability as either a  $K_S^0$  or a  $K_L^0$ . This is

important because the subsequent decay of the kaons is a critical part of the experimental signature.

The neutral kaons themselves emit no Cherenkov light. They can be detected and reconstructed only through the signature of their respective decay products. It turns out, however, that the majority of  $K_L^0$  produced by dinucleon decay would often travel outside of the detector before decaying ( $c\tau = 15.3$  m and  $\beta \sim .8$ ), thus being rendered undetectable. The rate of regeneration was estimated to be too small to appreciably increase the possible detection rate of  $K_L^0$ . Thus, all of the  $K_L^0$  dinucleon decay modes can be immediately eliminated from consideration.

Table 8.1 shows the branching ratios for the most probable final kaon decay states for all combinations of  $K^+$  and  $K_S^0$ . The two most favorable decay modes of  $K^+$  and  $K_S^0$  were included in this analysis:  $K^+ \rightarrow \mu^+\nu_\mu$  (B.R. 64%);  $K^+ \rightarrow \pi^+\pi^0$  (B.R. 21%);  $K_S^0 \rightarrow \pi^+\pi^-$  (B.R. 69%);  $K_S^0 \rightarrow \pi^0\pi^0$  (B.R. 31%). A 50% penalty is taken for every appearance of  $K_S^0$ , since the listed value is intended to measure the branching ratio of the decay mode of the  $K^0$ . A statistical factor of two has been folded into the branching ratio of the final decay states where two identical nucleon decay via different channels.

From Table 8.1 it can be seen that  $pp \rightarrow K^+ K^+$  has the greatest advantage in final decay state branching ratios, with a maximum theoretical efficiency of 70%, given the kaon decay modes that are considered. This is almost twice as large as the total theoretically achievable efficiency of either of the other two dinucleon decay modes,  $pn \rightarrow K^+ K^0$  and  $nn \rightarrow K^0 K^0$ , with maximum efficiencies of 42% and 36%, respectively. Thus,  $pp \rightarrow K^+ K^+$  was chosen for study in this analysis.

Decay Mode	Final State	B.R.
$pp \rightarrow K^+ K^+$	$\mu^+ \nu_\mu \mu^+ \nu_\mu$	40%
	$\mu^+ \nu_\mu \pi^+ \pi^0$	26%
	$\pi^+ \pi^0 \pi^+ \pi^0$	4%
total		70%
$pn \rightarrow K^+ K^0$	$\mu^+ \nu_\mu \pi^+ \pi^-$	22%
	$\mu^+ \nu_\mu \pi^0 \pi^0$	10%
	$\pi^+ \pi^0 \pi^+ \pi^-$	7%
	$\pi^+ \pi^0 \pi^0 \pi^0$	3%
total		42%
$nn \rightarrow K^0 K^0$	$\pi^+ \pi^- \pi^+ \pi^-$	22%
	$\pi^+ \pi^- \pi^0 \pi^0$	12%
	$\pi^0 \pi^0 \pi^0 \pi^0$	2%
total		36%

**Table 8.1:** Final state branching ratios for dinucleon decay into kaons. 100% represents the sum of all possible final decay states for a given dinucleon decay mode.

## 8.2 Choice of Kaon Decay Modes

At the next level of detail, the decision of which kaon decay modes to consider had to be made. The complexity of this choice was compounded by the fact that the final decay states of the signal events are a combination of two kaon decays. Helpfully, the theoretical branching ratios of the kaon decay modes are well known, and could be used to inform this decision.

Only the two most favorable  $K^+$  decay modes,  $K^+ \rightarrow \mu^+ \nu_\mu$  and  $K^+ \rightarrow \pi^+ \pi^0$ , were selected for this search. The next most favorable decay modes are three-body decays (*e.g.*,  $K_{e3}^+$  and  $K_{\mu3}^+$ ), which are significantly more challenging from an experimental perspective. The three-body decay modes would have a total Cherenkov ring count that would be beyond even the large number expected from the two chosen decay modes, significantly complicating and reducing the accuracy of the event reconstruction process. Further, the three-body decay modes lack the powerful discriminating

Decay Mode	Final State	B.R. (Calc.)	B.R. (MC)
$pp \rightarrow K^+ K^+$	$\mu^+ \nu_\mu \mu^+ \nu_\mu$	40%	30%
	$\mu^+ \nu_\mu \pi^+ \pi^0$	26%	19%
	$\pi^+ \pi^0 \pi^+ \pi^0$	4%	3%
	sum of above	70%	52%

**Table 8.2:** Final state branching ratios for  $pp \rightarrow K^+ K^+$ . The second branching ratio (B.R.) column was obtained from the Monte Carlo, and thus includes inefficiencies due to hadronic interactions of the kaons.

Hadronic Interaction	Probability per $K^+$
Charge Exchange ( $K^+ n \rightarrow K^0 p$ )	9.5%
$\Sigma$ Resonance ( $K^+ N \rightarrow \Sigma \pi$ )	1.0%
$\Lambda$ Resonance ( $K^+ N \rightarrow \Lambda \pi$ )	0.5%

**Table 8.3:** Hadronic interactions leading to detection inefficiencies in the simulated dinucleon decay events.

power of the monochromatic momenta of the decay products seen in the chosen two-body decay modes. All other  $K^+$  decay modes have insignificantly small branching ratios, and were thus not considered in this study.

The combined final state branching ratios for the two chosen kaon decay modes can be seen in Table 8.2, where the first numerical column shows the calculated branching ratio, and the second numerical column shows the branching ratio as obtained from the Monte Carlo. The latter takes into account inefficiencies due to hadronic interactions of the kaons, which are displayed in Table 8.3. The leading source of hadronic interaction inefficiencies was found to be charge exchange occurring as the kaon traveled through the water.

## 8.3 Cherenkov Ring Combinations

Having chosen which dinucleon decay mode and which final kaon decay states to consider, one last choice must be made to narrow down the signal characteristics to a set that can be reasonably studied. The basis of the final choice is strictly experimental in nature; it is to determine which of the various possible Cherenkov ring combinations that could arise in a signal event to consider in the analysis.

### 8.3.1 Ring Counting Inefficiencies

An important experimental limitation that had to be considered was that the Super-Kamiokande ring counting software has a built in maximum limit of five found rings. That means that an ideal event of the final state  $^{16}\text{O}(pp) \rightarrow ^{14}\text{C} K^+ K^+ \rightarrow \pi^+\pi^0 \pi^+\pi^0$  (two kaon rings, four gamma rings; see Section 8.4), could never have all six rings reconstructed.

More confoundingly, the ring counting software also occasionally misses rings completely, as it was originally designed and optimized for atmospheric neutrino and single proton decay ( $p \rightarrow e^+\pi^0$ ) events. Such events typically have at most two or three easily distinguishable rings, and have less than half the amount of visible light in the detector as would be seen in a dinucleon decay event.

Additionally, there was about a one in four chance that a kaon will decay in flight (see Section 8.4.2), thus boosting its decay products along its direction of movement, and therefore increasing the chance of creating significant ring overlap. Ring overlap was another complication that taxes the abilities of the ring finding and reconstruction software. Overlapping rings have a chance of being mistakenly identified as one single ring with a reconstructed momentum larger than that of either of its true constituent rings.

Nring	$\mu^+\nu_\mu$	$\mu^+\nu_\mu$	$\mu^+\nu_\mu$	$\pi^+\pi^0$	$\pi^+\pi^0$	$\pi^+\pi^0$
1		5.6%		6.2%		2.8%
2		33.1%		23.5%		15.5%
3		44.9%		41.9%		38.9%
4		15.6%		24.5%		32.6%
5		0.8%		4.0%		10.2%

**Table 8.4:** Frequency of found ring count by final decay state. Each column sums to 100%.

Another factor to be considered was that about one fifth of the kaons are produced below Cherenkov threshold, as shown in Fig. 8.3, due to the boost received as a result of the Fermi momentum of the parent protons.

Table 8.4 shows the total ring count frequency for each of the chosen final decay states. The combined effect of the sources of ring counting inefficiencies mentioned above can be seen in the table. Ideally, one would expect to find 4 rings for  $K^+K^+ \rightarrow \mu^+\nu_\mu \mu^+\nu_\mu$ , and the maximum 5 rings for  $K^+K^+ \rightarrow \mu^+\nu_\mu \pi^+\pi^0$  and  $K^+K^+ \rightarrow \pi^+\pi^0 \pi^+\pi^0$ . Regardless, the ring counting software worked well enough with the dinucleon decay events to continue the search and ultimately achieve a respectable final signal efficiency.

Though a large fraction of the chosen signal events had only two found rings, this category was dropped from further consideration across all final decay states. The reason for this choice depended largely upon the fact that many of these events contained in-flight kaon decays (hence the low ring count), which in turn decrease the performance of the reconstruction process described in Chapter 9. In addition, the amount of background to sort through would have been increased dramatically by including two-ring events. Thus, only events with 3–5 rings were considered in this search.

Final State	Nring	1 $K^+$	2 $K^+$	1 $\mu^+$	2 $\mu^+$	1 $\gamma$	2 $\gamma$	3 $\gamma$	4 $\gamma$
$\mu^+\nu_\mu \mu^+\nu_\mu$	3	60%	36%	42%	54%	–	–	–	–
	4	17%	79%	14%	79%	–	–	–	–
$\mu^+\nu_\mu \pi^+\pi^0$	3	61%	9%	58%	–	45%	49%	–	–
	4	63%	28%	71%	–	22%	64%	–	–
	5	35%	54%	78%	–	9%	54%	–	–
$\pi^+\pi^0 \pi^+\pi^0$	3	51%	6%	–	–	9%	52%	39%	–
	4	62%	15%	–	–	2%	22%	59%	17%

**Table 8.5:** Breakdown of true particle type frequency for rings generated in dinucleon decay events. 100% represents all dinucleon decay Monte Carlo events of a given final decay state.

### 8.3.2 True Particle Type Frequency

The next step in the process of narrowing down the accepted signal was to create a table such as Table 8.5, which documents the frequency of rings generated by a given true particle type in an event of a given final decay mode.

The table immediately revealed a feature common to all final decay states, which was that there was at least one true kaon ring in a large majority of the signal events. This turned out to be quite useful, as the kaon rings became the crux of the event reconstruction process described in Chapter 9.

Next, only the events with at least one true kaon ring were considered, and all of the possible ring combinations of these events were examined in Table 8.6. The frequency of ring combinations are shown in the table as a percentage of all  $^{16}\text{O}(pp) \rightarrow ^{14}\text{C} K^+ K^+$  Monte Carlo events.

In rank order by frequency of appearance in the  $pp \rightarrow K^+ K^+$  Monte Carlo, the possible ring combinations with at least one true kaon are:

- |                       |                         |
|-----------------------|-------------------------|
| (1) $K^+ K^+ \mu^+$   | (3) $K^+ \gamma \gamma$ |
| (2) $K^+ \mu^+ \mu^+$ | (4) $K^+ \mu^+ \gamma$  |

3 Rings		4 Rings		5 Rings	
$K^+ K^+ \mu^+$	7.4%	$K^+ K^+ \mu^+ \mu^+$	3.5%	$K^+ K^+ \mu^+ \gamma \gamma$	0.4%
$K^+ \mu^+ \mu^+$	6.8%	$K^+ K^+ \mu^+ \gamma$	1.0%	$K^+ K^+ \gamma \gamma \gamma$	0.2%
$K^+ K^+ \gamma$	1.4%	$K^+ \mu^+ \gamma \gamma$	3.2%	$K^+ \gamma \gamma \gamma \gamma$	0.6%
$K^+ \mu^+ \gamma$	4.1%	$K^+ K^+ \gamma \gamma$	1.0%		
$K^+ \gamma \gamma$	4.9%	$K^+ \gamma \gamma \gamma$	2.2%		

**Table 8.6:** Table of found ring combinations broken down by true particle type. Numbers are taken as a percentage of the total number of simulated  $^{16}\text{O}(pp) \rightarrow ^{14}\text{C} K^+ K^+$  events. Note that the gammas originate from neutral pion decay ( $\pi^0 \rightarrow \gamma\gamma$ ).

- |                                |  |
|--------------------------------|--|
| (5) $K^+ K^+ \mu^+ \mu^+$      | (10) $K^+ K^+ \gamma \gamma$           |
| (6) $K^+ \mu^+ \gamma \gamma$  | (11) $K^+ \gamma \gamma \gamma \gamma$ |
| (7) $K^+ \gamma \gamma \gamma$ | (12) $K^+ K^+ \mu^+ \gamma \gamma$     |
| (8) $K^+ K^+ \gamma$           | (13) $K^+ K^+ \gamma \gamma \gamma$    |
| (9) $K^+ K^+ \mu^+ \gamma$     |  |

To perform the final pruning of this list, the event reconstruction performance and the characteristics of the atmospheric neutrino background had to be considered.

In order to be able to make a strong claim that even a single candidate event found in the data is indeed a  $pp \rightarrow K^+ K^+$  event, strong evidence for two back-to-back  $K^+$  was required, though the evidence did not necessarily need to come in the form of two found  $K^+$  rings. For lack of a second found  $K^+$  ring in an event, a  $\mu^+$  ring could take its place, as the  $\mu^+$  could be required to fall into a narrow momentum window corresponding to  $K^+$  decay. The  $\mu^+$  ring would also be required to have a reconstructed vertex point located where one would have expected the missing kaon to have decayed, derived from the single found kaon ring's vertex position and ring direction.

A  $\gamma$  ring, however, was not considered a suitable substitute for a missed kaon ring. Firstly, the momentum window of the true  $\gamma$  rings was too large to be a reliable

indicator of  $K^+$  decay. Secondly, the reconstructed vertex resolution for  $\gamma$  rings was too large (see Section A.3) to be a reliable indicator of the expected event topology corresponding to the back-to-back dinucleon decay kaons.

### 8.3.3 Final List of Ring Combinations

The final consideration weighed the gain in signal efficiency achieved by including a particular ring combination against the estimated amount of effort required to accurately reconstruct the event, along with the estimated background that would accrue by including said ring combination. As a general rule for this search, the more gamma rings there were in the event, the more difficult it would be to accurately reconstruct, and the more background one would have to contend with.

Thus, with all of the above considerations in mind, the ring combinations  $K^+ \mu^+$ ,  $\gamma$ ,  $K^+ \gamma \gamma$ ,  $K^+ \gamma \gamma \gamma$ ,  $K^+ K^+ \gamma \gamma \gamma$ , and  $K^+ \gamma \gamma \gamma \gamma$  were eliminated. This left the final list of signal event ring combinations, referred to as event categories in the event reconstruction process, that were searched for in this analysis:

- $K^+ K^+ \mu^+$
- $K^+ \mu^+ \mu^+$
- $K^+ K^+ \mu^+ \mu^+$
- $K^+ \mu^+ \gamma \gamma$
- $K^+ K^+ \gamma$
- $K^+ K^+ \mu^+ \gamma$
- $K^+ K^+ \gamma \gamma$
- $K^+ K^+ \mu^+ \gamma \gamma$

## 8.4 Signal Characteristics

The characteristics of the  $pp \rightarrow K^+ K^+$  signal events were very distinct compared those of the atmospheric neutrino background events. In a dinucleon decay event,

both of the kaons are ejected from the parent nucleus in a back-to-back configuration, traveling a distance of up to 1.3m before coming to a stop and eventually decaying. The kaons each would have a sufficient momentum to emit a detectable amount of Cherenkov light, and at least one of each kaon's decay products would in turn emit Cherenkov light of its own.

Figure 8.1 shows an illustration of an idealized  $pp \rightarrow K^+ K^+$  event, where one kaon has decayed via  $K^+ \rightarrow \pi^+ \pi^0$ , and the other via  $K^+ \rightarrow \mu^+ \nu_\mu$ . Note that the  $\pi^0$  is represented as two  $\gamma$ 's. This is because the  $\pi^0$  decays at a rate fast enough that the distance it travels before it decays is unresolvable in a detector, therefore the resultant  $\gamma$ 's can be considered to originate from the same vertex point as their parent  $\pi^0$ .

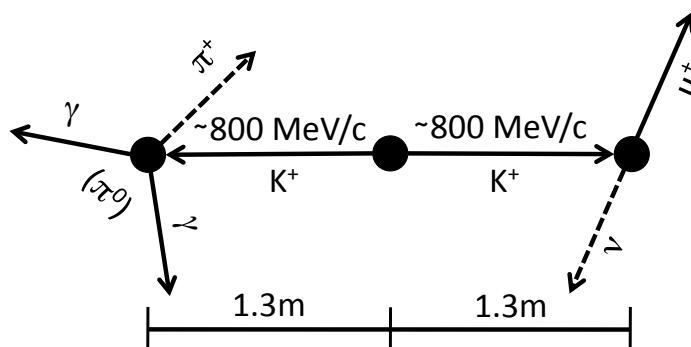


**Figure 8.1:** A cartoon illustration of an ideal  $pp \rightarrow K^+ K^+$  event. Dashed lines represent undetectable particles.

In total, there are three discernible particle vertices in a  $pp \rightarrow K^+ K^+$  event: one shared by the kaons at the point of the dinucleon decay, and one additional vertex at the point of each kaon decay. These vertices would be separated by distances that are resolvable in Super-Kamiokande, and they all would lie approximately along the axis of the back-to-back kaons.

All of this together presents an incredibly unique event geometry. When com-

bined with kinematic information and other characteristics of the event's constituent rings, the result is an event signature that is quite difficult to mistake, when well reconstructed.

### 8.4.1 Multiple Vertices

One of the most distinguishing aspects of the dinucleon decay signal is the fact that it contains three distinct vertices where Cherenkov light emitting particles are produced, separated by distances resolvable by the detector ( $\sim 1$  m). The first vertex comes from the point where the dinucleon decay itself occurs. This vertex point is shared by both of the outgoing kaons. The second and third vertex points occur at the decay points of the two kaons.

Figure 8.2 shows the distance between the kaon decay point and the original dinucleon decay vertex. Also shown is the distance between the two kaon decay points in each event. As expected, the distance between the kaon decay points had a peak near twice the distance of the first plot due to the back-to-back directionality of the kaons, with a sharp fall off at larger distances.

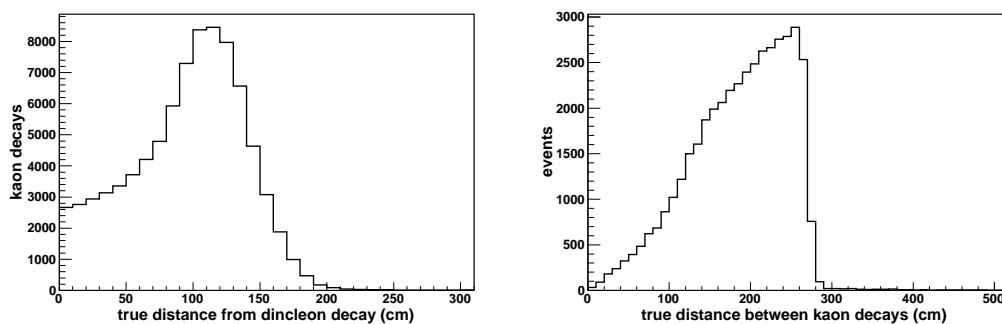


**Figure 8.2:** Left: The true distance between the kaon decay point and the dinucleon decay point. Right: The true distance between the two dinucleon decay points within the same event.

## 8.4.2 Kaon Rings

Another distinctive feature of the signal events was the presence of Cherenkov rings produced by charged kaons. Figure 8.3 shows the true momentum distribution for the  $K^+$  produced in the dinucleon decay Monte Carlo. About 77% of the kaons were produced above Cherenkov threshold. This feature is atypical not only when compared to the atmospheric neutrino background, but also when compared to any study previously performed at Super-Kamiokande. For this reason it required the addition of new reconstruction tools, as described in Section 7.1.4.

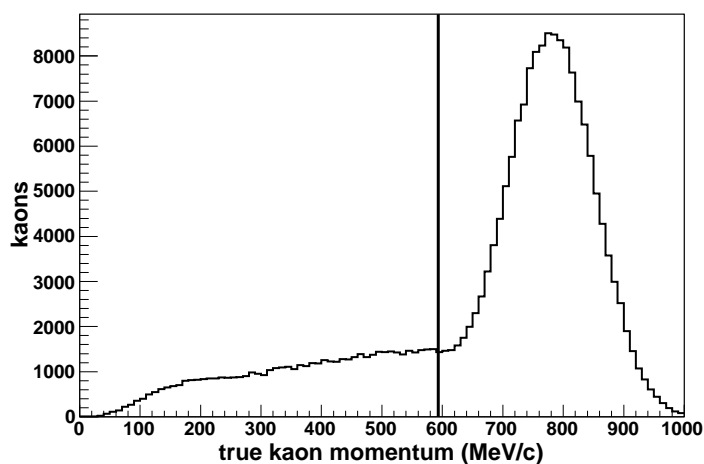


**Figure 8.3:** The momentum distribution of the outgoing kaons produced by the dinucleon decay reaction  $^{16}\text{O}(pp) \rightarrow ^{14}\text{C} K^+ K^+$  in the Monte Carlo. The line represents the Cherenkov threshold for  $K^+$ , 563 MeV/ $c$ .

Unfortunately, it was difficult to distinguish kaon rings from muon rings on an individual basis, as they are both non-showering particles. There was a further unfortunate similarity between the kaon and muon rings in the dinucleon decay signal events that prevents their respective well-determined momenta from being used as an identifying feature.

It happens that the kaon-like reconstructed momentum of the true  $\mu^+$  rings in the

dinucleon decay signal fell right in the expected true  $K^+$  momentum window, and vice versa for the muon-like momentum of the true  $K^+$  rings. This can be understood by considering the RTOT-momentum look-up table used in the momentum reconstruction process, shown in Fig. 7.6. The peak kaon momentum is about 800 MeV/ $c$ , while the peak muon momentum is 236 MeV/ $c$ . Both of these yield a very similar RTOT value of roughly 500 p.e. Fortunately, the event topology was able to help inform the ring classification, as described in detail in Chapter 9, and the kaon rings in the signal were yet able to be identified with very high fidelity.

### 8.4.3 Back-to-Back Kaons

Besides the mere presence of Cherenkov rings generated by charged kaons, the back-to-back directionality of the kaon rings is also a distinct feature of dinucleon decay. Figure 8.4 shows the cosine of the opening angle between the true directions of the kaons. It peaks sharply at  $-1$ , though there is a tail due to the Fermi momentum of the parent protons, as well as the effect of correlated decay (see Section 5.1). Roughly 93% of the kaon pairs had an opening angle between them of greater than  $154^\circ$  (*i.e.*,  $\cos(\theta) < -0.9$ ).

### 8.4.4 Features of Kaon Decay Modes

Each of the final decay modes of the kaons had its own set of unique features, described in this section.

#### $K^+ \rightarrow \mu^+ \nu_\mu$ Features

In the muon decay mode,  $K^+ \rightarrow \mu^+ \nu_\mu$ , the outgoing particles are emitted back-to-back from the kaon decay point, each with a momentum of precisely 236 MeV/ $c$ .

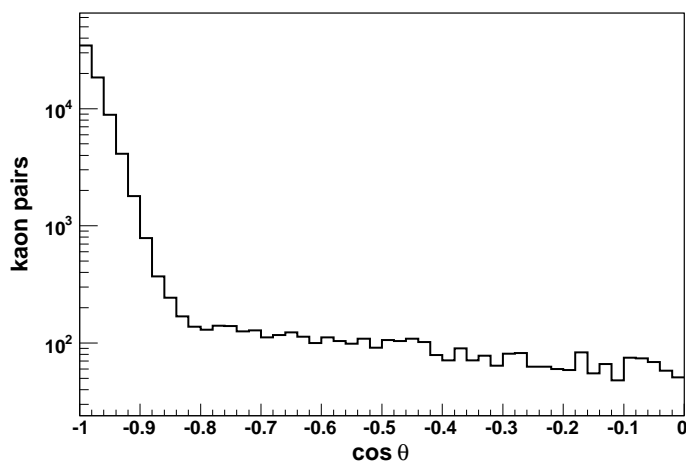


**Figure 8.4:** Cosine of the opening angle between the true directional vectors of the outgoing kaons.

This is above Cherenkov threshold for the muon ( $p_{\text{thresh}}[\mu^\pm] = 120 \text{ MeV}/c$ ), giving the particle a Cherenkov angle of  $34.6^\circ$ . The neutrino leaves the tank without being detected.

Figure 8.5 shows the distribution of true muon momenta produced by the decay mode  $K^+ \rightarrow \mu^+ \nu_\mu$  in the dinucleon decay Monte Carlo. The peak at  $236 \text{ MeV}/c$  corresponds to the monochromatic momentum resulting from a kaon decaying while at rest. The momentum values that differ from  $236 \text{ MeV}/c$  occurred when the parent kaon decayed in flight before it could come to a stop through ionization energy loss. These off-peak muons accounted for about 27% of all muons in the dinucleon decay Monte Carlo that were produced through kaon decay.

### $K^+ \rightarrow \pi^+ \pi^0$ Features

In the pion decay mode,  $K^+ \rightarrow \pi^+ \pi^0$ , the outgoing particles are again emitted back-to-back, this time with a precise momentum of  $203 \text{ MeV}/c$ . However, the  $\pi^0$  immediately ( $\tau = 8.4 \times 10^{-17} \text{ s}$ ) decays into two gammas, each of which is boosted

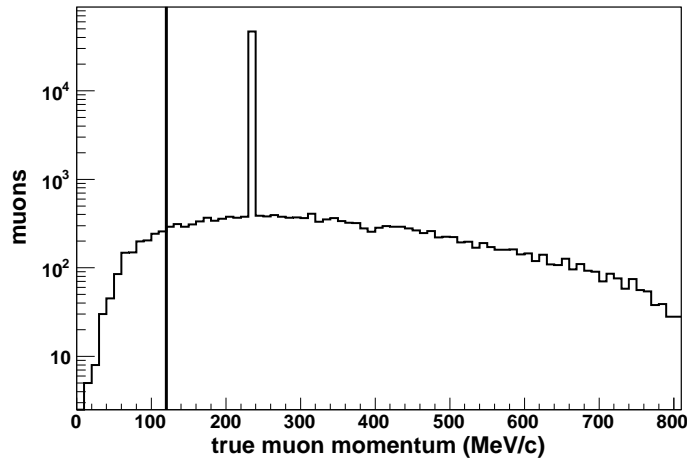


**Figure 8.5:** True momentum distribution of muons produced by the kaon decay channel  $K^+ \rightarrow \mu^+ \nu_\mu$  in the dinucleon decay Monte Carlo. The line represents the Cherenkov threshold for  $\mu^+$ , 120 MeV/ $c$ . The peak corresponds to the monochromatic momentum of 236 MeV/ $c$  resulting from a kaon decaying while at rest. The off-peak values are from in-flight decays of the parent kaons.

along the direction of the parent pion. This gives the gammas momenta ranging from 20 MeV/ $c$  to 227 MeV/ $c$ , as shown in Fig. 8.6, with a small tail resulting from in-flight kaon decays.

The  $\pi^+$ , on the other hand, have a precisely determined momentum of 203 MeV/ $c$ , which is barely above Cherenkov threshold ( $p_{\text{thresh}}[\pi^\pm] = 160$  MeV/ $c$ ). The small number of Cherenkov photons produced by the  $\pi^+$ , however, get drowned out by the copious amount of light produced by all of the other visible particles in the dinucleon decay event. The  $\pi^+$  is effectively undetectable, and therefore no attempt was made to search for any rings produced by  $\pi^+$  in this analysis.

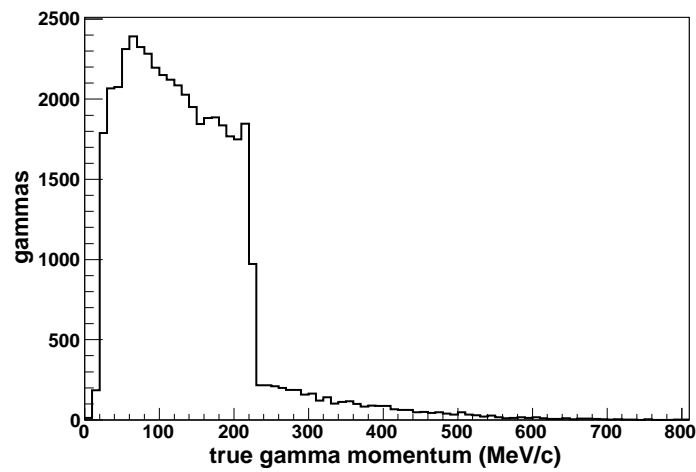


**Figure 8.6:** True momentum distribution of gammas produced by the kaon decay channel  $K^+ \rightarrow \pi^+\pi^0$  in the dinucleon decay Monte Carlo. The range of momenta produced by decays while the kaon is at rest is 20–227 MeV/ $c$ . The tail is from in-flight decays of the parent kaons. Gammas are EM showering particles, thus will always yield detectable Cherenkov light for any energy above a few MeV/ $c$ .

## Chapter 9

# Dinucleon Decay Search

The underlying methodology of the search was to hypothesize that each event analyzed was generated by dinucleon decay into kaons, and then compare how well the event's reconstructed variables matched the expected values for a genuine signal event, as determined by the dinucleon decay Monte Carlo.

The search was performed in four steps. The first (and most involved) step was to classify all found rings in an event as either kaon, muon, or gamma candidate rings. The second step was to categorize the event based on the classification of its constituent rings. In the third step, several precuts were applied which reduce the background and “cleaned up” the signal without reducing the search efficiency too much. Finally, in the fourth and final step, thirty-seven reconstructed variables were all combined into a single discriminatory variable through the use of a boosted decision tree. A final cut was placed on the output of the boosted decision tree which was used to define the final accepted signal-like sample.

## 9.1 Ring Classification

The ring classification stage depended upon the hypothesis that the observed rings in an event arose from the reaction  $^{16}\text{O}(pp) \rightarrow ^{14}\text{C} K^+ K^+$ , where the kaons then decayed via  $K^+ \rightarrow \mu^+ \nu_\mu$  or  $K^+ \rightarrow \pi^+ \pi^0$ . Under this assumption, the topology of the event may inform the choice of ring classification in a powerful way.

The term “ring classification” is used in this analysis, whereas “particle identification” (or “PID”) is not. This was a conscious choice to reflect that rings were being matched up with the most appropriate particle type based on the hypothesis that the event is indeed a dinucleon decay event. This should yield correct results for the signal events, however the particle type assignments should be incorrect almost by design when considering background atmospheric neutrino events. Hence the term “PID” was deemed somewhat inappropriate to use in this stage of the search.

In more conventional Super-Kamiokande analyses, PID is performed at the individual ring level, essentially only taking into account whether or not the particle is of a showering or non-showering type. The former would indicate an electron, positron, or gamma, and the latter would indicate a muon or a heavier charged particle. This level of distinction is nearly always sufficient for the studies performed at Super-Kamiokande.

In the case of dinucleon decay into kaons, however, rings generated by charged kaons would be identified as non-showering, but no further disambiguation could be made between said kaon rings and rings generated by muons based on their respective showering likelihoods alone. This was the motivating factor behind incorporating topology into the ring classification process.

The next important assumption regarded which of the Cherenkov light producing particles in a given dinucleon decay event were most likely to be found. Table 9.1, Ta-

ble 9.2, and Table 9.3 show the frequency of finding a given number of rings produced by kaons, muons, and gammas in the dinucleon decay Monte Carlo, respectively. The entries in the tables are organized by final state and the total number of rings found in an event. Note that the  $\gamma$ 's were the by-products of the  $\pi^0$  produced by the decay of the  $K^+$ .

Final State	Nring	0 $K^+$	1 $K^+$	2 $K^+$	$\geq 1 K^+$
$\mu^+\nu_\mu \mu^+\nu_\mu$	3	4%	60%	36%	96%
	4	4%	17%	79%	96%
$\mu^+\nu_\mu \pi^+\pi^0$	3	30%	61%	9%	70%
	4	9%	63%	28%	91%
	5	11%	35%	54%	89%
$\pi^+\pi^0 \pi^+\pi^0$	3	44%	51%	6%	56%
	4	23%	62%	15%	77%

**Table 9.1:** Frequency of rings produced by kaons in  $pp \rightarrow K^+ K^+$  Monte Carlo events.

Final State	Nring	0 $\mu^+$	1 $\mu^+$	2 $\mu^+$	$\geq 1 \mu^+$
$\mu^+\nu_\mu \mu^+\nu_\mu$	3	4%	42%	54%	96%
	4	7%	14%	79%	93%
$\mu^+\nu_\mu \pi^+\pi^0$	3	42%	58%	–	58%
	4	29%	71%	–	71%
	5	22%	78%	–	78%

**Table 9.2:** Frequency of rings produced by muons in  $pp \rightarrow K^+ K^+$  Monte Carlo events.

Final State	Nring	0 $\gamma$	1 $\gamma$	2 $\gamma$	3 $\gamma$	4 $\gamma$	$\geq 1 \gamma$
$\mu^+\nu_\mu \pi^+\pi^0$	3	6%	45%	49%	–	–	94%
	4	14%	22%	64%	–	–	86%
	5	37%	9%	54%	–	–	63%
$\pi^+\pi^0 \pi^+\pi^0$	3	0%	9%	52%	39%	–	100%
	4	0%	2%	22%	59%	17%	100%

**Table 9.3:** Frequency of rings produced by gammas in  $pp \rightarrow K^+ K^+$  Monte Carlo events.

An important feature that can be seen in Table 9.1 is that there was at least one ring produced by a kaon in the majority of all dinucleon decay events of the three chosen final states. The ring classification algorithm took advantage of this fact and used the kaon rings as the cornerstone of the full classification process.

### 9.1.1 Two Kaon Ring Classification

The key to ring classification and the overall event reconstruction in this search was to first identify the kaon candidate ring(s) in the event. Accordingly, the first priority of the ring classification process was to determine whether or not there are two rings that can be classified as kaon candidates. This was done by considering the pair of rings with the largest opening angle between their directions and checking to see whether they satisfied the following criteria:

- (1) the opening angle must be  $> 154^\circ$
- (2) the vertex separation must be  $< 640$  cm
- (3) the showering likelihood of both rings must be  $> -2.4$
- (4) the Cherenkov angle of both rings must be  $< 40^\circ$
- (5) the invariant mass must be  $< 1940$  MeV/ $c^2$
- (6) the total momentum must be  $< 400$  MeV/ $c$

where the last three items were all calculated using the kaon-like values for both rings.

Figure 9.1 shows the distributions of the variables used in the two-kaon classification process for the dinucleon decay Monte Carlo. Each entry represents either the pair of rings with the largest opening angle between their directions in a given event

(*e.g.*, the reconstructed invariant mass), or one of those two rings counted individually (*e.g.*, the showering likelihood).

### 9.1.2 Kaon Decay Product Ring Classification

After the two kaon candidates have been identified, the next step was to classify all of the remaining rings in the event as one of the two possible kaon decay product ring types, muon or gamma. This step of the classification relied heavily upon the geometric relationship between the kaons and their decay products. See Fig. 8.1 for an illustration of the dinucleon decay event geometry.

The primary instrument in this step of the classification was the impact parameter for each particle type hypothesis. The impact parameter was defined as the distance between the vertex of a kaon decay product candidate ring and an infinite line drawn along the directional vector of the most likely parent kaon candidate. See Fig. 9.2 for an illustration of the impact parameter.

The particle type hypothesis which yielded the smallest impact parameter became the classification of the ring. Figure 9.3 shows the impact parameters for all true  $\mu^+$  and  $\gamma$  rings in the dinucleon decay Monte Carlo as calculated using both the muon-like and gamma-like vertex of every ring. The difference between the incorrect and correct impact parameter can be seen in Fig. 9.4. The positive entries in this plot represent rings where the correct classification would be assigned using the impact parameter method.

To further refine the performance of the kaon decay product ring classification, all muon and gamma candidate rings were also required to satisfy the type-specific criteria listed below:

- Muon candidates:  $200 \text{ MeV}/c < \text{muon-like momentum} < 300 \text{ MeV}/c$

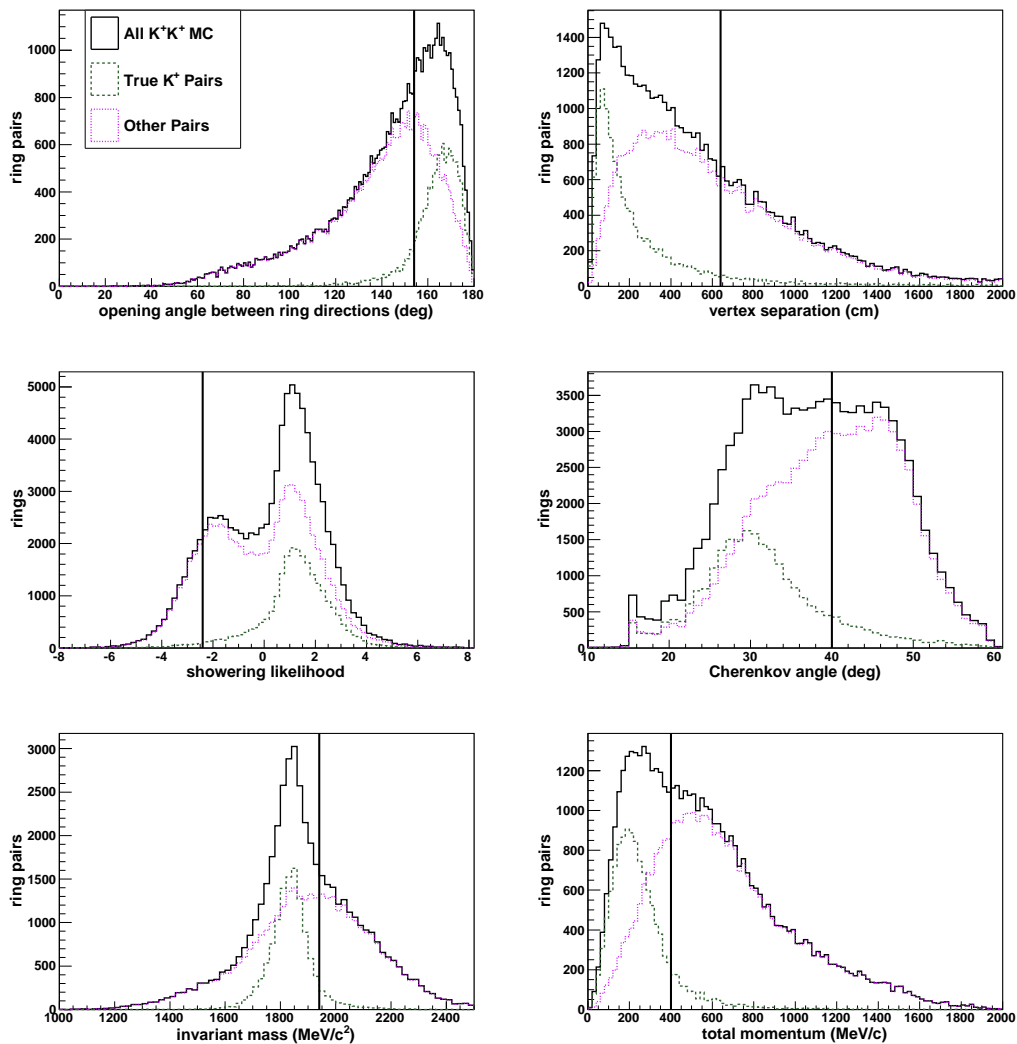


**Figure 9.1:** Reconstructed variables used in the two-kaon classification process. Kaon-like variables were used in all applicable plots. The dashed lines show the subset of events where the rings were actually generated by two kaons, and the dotted lines show the subset of events where the rings were generated by other particles (including events where only one of the rings from the pair was a true kaon ring). Vertical lines indicate the two-kaon classification criteria.

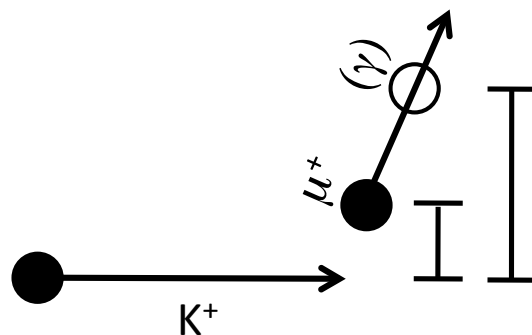


**Figure 9.2:** Illustration of the impact parameter variable used in the classification of the kaon decay product candidate rings. The illustration shows part of a reconstructed event where one kaon decayed via  $K^+ \rightarrow \mu^+ \nu_\mu$ . The circles represent reconstructed vertices and the arrows represent reconstructed ring directions. The correct classification has been chosen for the true  $K^+$  ring, and the impact parameter is shown for both possible classifications of the true  $\mu^+$  ring. The correct classification yields a smaller impact parameter.

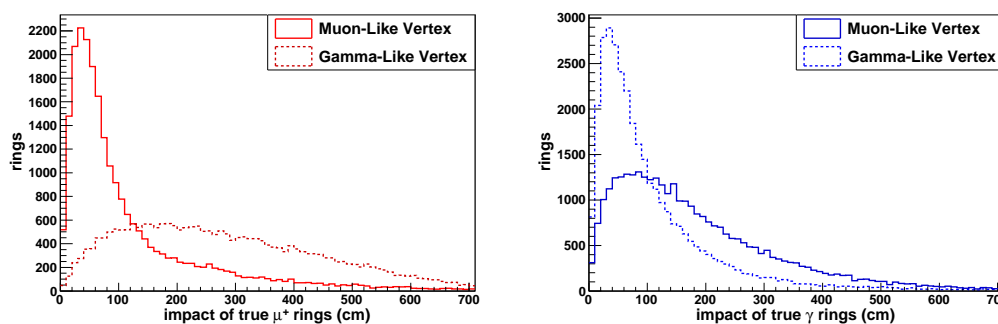


**Figure 9.3:** Impact parameter calculated using both the muon-like and gamma-like vertices of all true muon (left) and gamma (right) rings from the dinucleon decay Monte Carlo. Solid lines indicate the muon-like reconstructed vertex was used in the calculation of the impact parameter, and dashed lines indicate the gamma-like reconstructed vertex was used.

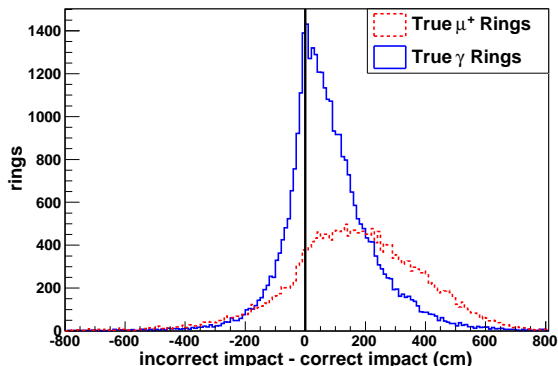


**Figure 9.4:** The difference between the impact parameter as calculated using the incorrect and the correct reconstructed vertex for all true muon and gamma rings. A positive value indicates that the correct particle type yielded the smaller impact parameter, thus would be chosen by the ring classification algorithm. The dashed line represents the true muon rings, and the solid line represents the true gamma rings from the dinucleon decay Monte Carlo.

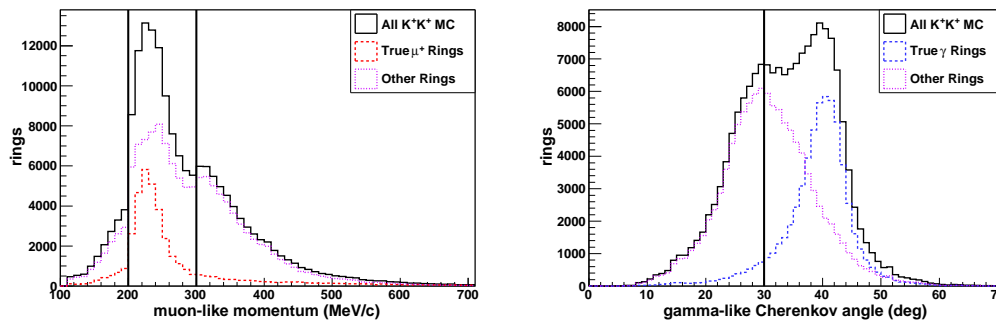
- Gamma candidates: gamma-like Cherenkov angle  $> 30^\circ$

Figure 9.5 shows the distributions of the variables used in the criteria above.

The overall performance evaluation for kaon decay product ring classification was estimated by assigning the correct classification to all kaon rings in every event (*i.e.*, the kaons are assumed to have been properly classified), and then applying the impact parameter method plus the secondary particle-specific criteria. The approximate misclassification rates under the given assumptions were about 20% for true muon rings and 28% for true gamma rings. The reason  $\gamma$  rings were more often mis-classified is because the reconstructed vertex resolution was somewhat worse than that of muon rings (see Appendix A).

### 9.1.3 Pion Classification

If the kaon decay product classification process classified two rings from the same parent kaon as gamma candidates, they were then taken to be from the same original



**Figure 9.5:** Reconstructed variables used in the secondary criteria of the kaon decay product classification process. Left: Reconstructed muon-like momentum of all rings in the dinucleon decay Monte Carlo. Right: Reconstructed gamma-like Cherenkov angle of all rings in the dinucleon decay Monte Carlo. In both plots, the dashed line represents the true muon (left) or gamma (right) rings, and the dotted line represents all other rings. The vertical lines indicate the classification criteria.

$\pi^0$ . The  $\pi^0$  was reconstructed in full and considered to be the kaon decay product. Its vertex was taken to be the spatial average of the reconstructed gamma-like vertices of its two constituent gamma rings.

#### 9.1.4 Low Gamma Momentum Correction

A final correctional step was taken to catch true muon rings that have been misclassified as gamma candidates. This was done when the total momentum of all gamma candidate rings was less than 100 MeV/c. If there was only one gamma candidate ring, it was reassigned as a muon candidate, as long as there were not already two muon candidates in the event. If there were two gamma candidates, the most non-showering ring was reassigned as a muon candidate first, and then the second. Again, the rule was held where there can be no more than two muon candidates in a single event. If there existed two muon candidates when the algorithm was attempting to reassign a current gamma candidate, the ring simply remained as a gamma candidate.

### 9.1.5 Single Kaon Ring Classification

If an event failed to meet the two-kaon search criteria outlined in Section 9.1.1, the single-kaon search criteria was then applied. About 23% of the kaons produced in dinucleon decay events had momenta below Cherenkov threshold and about 27% decay in flight, reducing the performance of the reconstruction software. For these reasons, events with only a single found kaon ring represented a significant enough portion of the signal that it entailed the creation of an additional algorithm designed to classify the rings in such events.

To find the most appropriate kaon candidate in the event, each ring was considered in turn as the “test” kaon candidate, as long as its kaon-like Cherenkov angle was  $< 40^\circ$  (see Fig. 9.6). The other rings in the event were forced to conform to the most appropriate kaon decay product test classifications under the assumption that the test kaon candidate ring was a true kaon ring. The test decay product classifications were determined by the algorithm set forth in Section 9.1.2. A variable called the “linearity” was then calculated for the test kaon candidate, effectively representing the likelihood that a given ring was from a true dinucleon decay kaon.

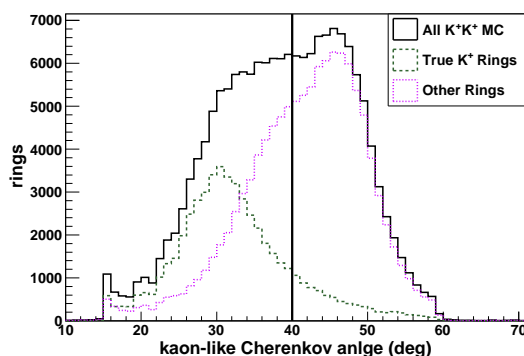


**Figure 9.6:** Reconstructed kaon-like Cherenkov angles for all rings in the dinucleon decay Monte Carlo. The dashed line represents the true kaon rings, and the dotted line represents all other rings. The vertical line represents the single-kaon classification criteria.

The linearity quantifies the linear geometry of the event, given the current test ring classifications. The linearity was calculated by first taking the cosine of the angle formed between a line drawn from the test kaon candidate's kaon-like vertex point to one of the test kaon decay product candidates' appropriate reconstructed vertex point and the directional vector of the test kaon candidate. This value was then multiplied by the cosine of the angle formed by the test kaon candidate's direction vector and the line between its vertex and the other decay product candidate ring's appropriate vertex. Figure 9.7 shows an illustration of how the linearity was determined. The more well aligned all of the vertices were along the test kaon candidate's direction, the more negative this value would be. A perfectly linear configuration would yield a linearity value of  $-1$ .

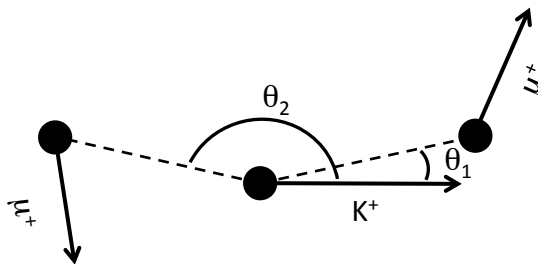


**Figure 9.7:** Illustration of the linearity variable used in the single-kaon classification process. The illustration shows reconstructed  $K^+K^+ \rightarrow \mu^+\nu_\mu \mu^+\nu_\mu$  event where the correct classification has been chosen for the three found rings ( $K^+$ ,  $\mu^+$ ,  $\mu^+$ ). The second kaon is here assumed to have been produced below Cherenkov threshold. The circles represent the reconstructed vertices, and the arrows represent the reconstructed directions. The linearity for the visible kaon candidate ring is defined as  $\cos \theta_1 \cdot \cos \theta_2$ .

Figure 9.8 shows the difference between the linearity calculated for every true gamma and muon ring and the true kaon ring in the same event, for all events in the dinucleon decay Monte Carlo which had only one true visible kaon ring. Entries with positive values represent events where the true kaon ring would have been chosen over the other rings in the event as the kaon candidate. Fifty-seven percent of the

dinucleon decay Monte Carlo events which contained only one true kaon event were correctly classified as a single kaon event. Of those, 94% correctly identified the true kaon ring as the kaon candidate.

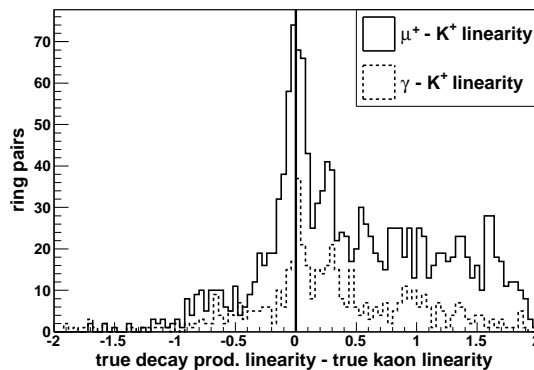


**Figure 9.8:** Difference in linearity between true muon and gamma rings and true kaon rings. Positive values indicate the true kaon ring was favored over the other ring as the kaon candidate.

## 9.2 Event Categorization

The event categorization process is simply the process of labeling each event according to the classifications of its constituent rings. For example, an event in which two rings were classified as kaon candidates, and one ring was classified as a muon candidate would be categorized as a “ $K^+ K^+ \mu^+$ ” event.

If at least one ring was not able to be classified as either a kaon, muon, or gamma candidate by the classification algorithms described in Section 9.1, then the event is simply categorized as an “other”-type event.

### 9.3 Precuts

After the ring classification and event categorization processes, several precuts were applied with the goal of eliminating easily identifiable background and restricting signal sample to events which were well reconstructed while retaining as large an efficiency as possible. The precuts are listed below:

- (1)  $1000 < POTOT < 11000$ , where  $POTOT$  is the total amount of light seen in the ID in units of p.e.
- (2)  $3 \leq NRING \leq 5$ , where  $NRING$  is the number of found rings in the event.
- (3)  $0 \leq NDCYE \leq 2$ , where  $NDCYE$  is the number of found decay electrons.
- (4)  $WALL > 200$  cm, where  $WALL$  is the distance from the event vertex to the nearest wall; this is the fiducial volume (FV) cut.
- (5) And finally, the event category must fall into one of the eight accepted dinucleon decay event categories listed in Section 8.3.3.

Figure 9.9 shows the distributions of the reconstructed variables used in the precuts.

The first three precuts were intended to retain roughly all of the signal while significantly reducing the background, which had a much wider spread in  $POTOT$  than the signal, and an event count distribution that fell rapidly with increasing ring count. The decay electron count was limited to the maximum number we would expect from the dinucleon decay signal events.

The fiducial volume cut was applied to ensure optimal and uniform reconstruction resolution throughout the target region. Further, it created a well-defined boundary with a volume that was simple to calculate. Both of these factors were crucial in the

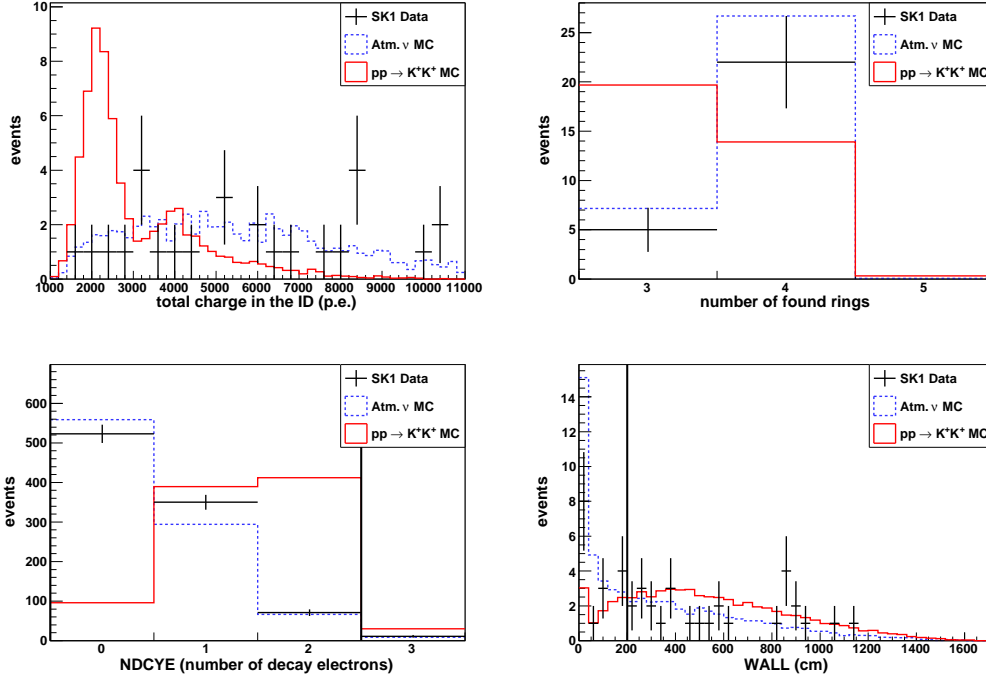


**Figure 9.9:** Reconstructed variables used in the precuts. From top-left to bottom-right:  $POTOT$ ,  $NRING$ ,  $NMUEDCY$ , and  $WALL$ . The solid lines indicate the  $pp \rightarrow K^+ K^+$  Monte Carlo, the dashed lines indicate the atmospheric neutrino Monte Carlo, and the markers indicate the SK-I data. Vertical lines indicate the boundaries of the precuts.

estimation of the total exposure. The fiducial volume was defined as the region in the ID that is at least 200 cm from the nearest wall.

Finally, the event category requirement ensures that the event was well reconstructed, and limits the search to categories that are most likely to come from a true dinucleon decay event. See Section 8.3 for a more detailed explanation of why these particular event categories were chosen.

Table 9.4 shows signal efficiency, expected background, and data events passing the precuts, broken down by event category. The total efficiency for the signal after applying the precuts was 21.9%. The total expected background was 33.9 events after normalizing to the SK-I livetime. The total number of events in the SK-I data passing

the precuts was 27.

Event Category	$pp \rightarrow K^+ K^+$ M.C. efficiency (%)	Atmospheric $\nu$ M.C. events / SK-I livetime	SK-I Data events
$K^+ K^+ \mu^+$	6.1	0.6	0
$K^+ \mu^+ \mu^+$	5.6	6.1	5
$K^+ K^+ \gamma$	1.1	0.4	0
$K^+ K^+ \mu^+ \mu^+$	2.7	0.0	0
$K^+ K^+ \gamma \gamma$	0.6	0.3	0
$K^+ \mu^+ \gamma \gamma$	4.6	26.1	22
$K^+ K^+ \mu^+ \gamma$	1.1	0.3	0
$K^+ K^+ \mu^+ \gamma \gamma$	0.2	0.1	0
total	21.9	33.9	27

**Table 9.4:** Signal, background, and data after applying precuts.

The event category in which the SK-I data and the expected background rate differed the most was  $K^+ \mu^+ \gamma \gamma$ , where the atmospheric neutrino Monte Carlo predicted 26 events of background, and only 22 such events were found in the data. Using Poisson statistics, the probability of seeing 22 or fewer events given the expected value of 26 is about 20%.

Table 9.5 summarizes background Monte Carlo events which survived the precuts by neutrino flavor and weak current type, and Table 9.6 shows the breakdown of neutrino interaction types of the surviving background. Charged current (CC) and neutral current (NC) muon neutrino events made up the majority of the background after the precuts. Single and multi-pion interactions were the dominant interaction types.

## 9.4 Multi-Variate Analysis

For the final portion of the analysis, a multi-variate approach was taken to increase the sensitivity of the search. Multi-variate techniques were considered appealing for

$\nu$ Mode	Events/200 Years	Events/1489.2 Days	%
CC $\nu_\mu$	1654	13.5	41
NC $\nu_\mu$	1303	10.6	32
CC $\nu_e$	588	4.8	14
NC $\nu_e$	517	4.2	13
total	4062	33.1	100

**Table 9.5:** Remaining background Monte Carlo events after precuts sorted by neutrino flavor and weak current type. CC: Charged Current; NC: Neutral Current. The first numerical column shows the unscaled number of events from the 200 year analysis sample. The second numerical column shows the number of events scaled to the SK-I livetime.

Interaction	Events/200 Years	Events/1489.2 Days	%
CC single pion delta resonance	942	7.7	23.2
CC multi-pion production	896	7.3	22.0
NC multi-pion production	660	5.4	16.2
NC diffractive pion production	549	4.5	13.5
NC single pion delta resonance	542	4.4	13.3
CC diffractive pion production	265	2.2	6.5
CC quasi-elastic	104	0.9	2.6
NC elastic	49	0.4	1.2
CC coherent pion production	35	0.3	0.9
NC coherent pion production	20	0.2	0.5
total	4062	33.1	100

**Table 9.6:** Remaining background Monte Carlo events after precuts sorted by neutrino interaction type. CC: Charged Current; NC: Neutral Current. The first numerical column shows the unscaled number of events from the 200 year analysis sample. The second numerical column shows the number of events scaled to the SK-I livetime.

this study due to their ability to simultaneously analyze many different discriminatory variables spanning many different event categories. This would be extremely difficult to accomplish using a simple cuts-based analysis, such as the one used in the  $p \rightarrow e^+\pi^0$  search, which hinges largely upon the combined discriminating power of only two variables: the invariant mass and the total momentum of the system.

After some consideration, a boosted decision tree was chosen to be used as the multi-variate tool for this analysis. Several factors played in this decision. First, the performance of a boosted decision tree is not degraded by the addition of weakly discriminating variables [74]. If a variable is so weakly discriminating as to be useless, it is simply not used by the boosted decision tree.

Second, a boosted decision tree will be unhindered by variables that may have trivial values for some events. This is accomplished through the use of a trivial bin designated by the user. For example, an event which has only one kaon candidate ring might be assigned a meaningless value of  $-10$  for its reconstructed dinucleon mass variable during the classification and categorization stage of the analysis. Thus if the boosted decision tree were to place a cut at 0 on this variable, it would effectively be the same as cutting on whether or not an event had two kaon candidates. This technique requires that the trivial bin be outside of the region of interest for the non-trivial entries, though it shouldn't be too far from the region of interest, or else the binning resolution of the variable will be degraded. In a multi-variate analysis, every event has to have some value for every variable, so the technique of using a trivial bin is particularly useful in this analysis because it allows events of all categories to be processed by the same boosted decision tree.

Finally, boosted decision trees have a proven track record in background dominated studies in the world of particle physics [75–77].

The process of creating and applying the boosted decision tree was accomplished in three stages: training, testing, and analysis. Each stage required its own independent set of signal and background Monte Carlo. As such, the atmospheric neutrino and dinucleon decay Monte Carlo sets were both divided into three roughly equal portions as described in Table 9.7. The actual SK-I data was only ever used in the final stage of performing the analysis, thus required no splitting.

Monte Carlo	Training	Testing	Analysis
$pp \rightarrow K^+ K^+$	25,000 events	25,000 events	25,000 events
Atm. $\nu$	150 years	150 years	200 years

**Table 9.7:** Division of the Monte Carlo in the multi-variate portion of the analysis.

### 9.4.1 Input Variables

In total, 37 variables were chosen to be used as inputs for the boosted decision tree. The names of these variables along with a brief description of each follow:

#### Variables related to the reconstructed dinucleon

- **rec\_dinuc\_mass:** The reconstructed dinucleon pair mass. Expected to peak near the sum of the true mass of two nucleons, roughly  $1900 \text{ MeV}/c^2$ , for signal events, and random for background events, which never contain two true kaons produced by dinucleon decay.
- **rec\_dinuc\_mom:** The reconstructed dinucleon pair momentum. Expected to be small (around  $200 \text{ MeV}/c$ ) for signal events, and be random for background events, which never contain two true kaons produced by dinucleon decay.
- **k\_cand\_vtxsep:** The separation of the vertices of the kaon candidates which make up the reconstructed dinucleon. Expected to be small for signal events, and random for background events, which never contain two true kaons produced by dinucleon decay.

#### Variables related to the reconstructed $\pi^0$

- **rec\_pi0\_mass:** The reconstructed  $\pi^0$  mass. Expected to peak at the true mass,  $135 \text{ MeV}/c^2$ , for signal events, and be somewhat random for background events, which may contain true pions, but are reconstructed under a false hypothesis.
- **rec\_pi0\_mom:** The reconstructed  $\pi^0$  momentum. Expected to peak around  $206 \text{ MeV}/c$  for signal events, and have a random distribution for background events, which do not contain monochromatic pions produced by kaon decay.
- **g\_cand\_vtxsep:** The separation of the vertices of the gamma candidates which make up the reconstructed  $\pi^0$ . Expected to be small for signal events, and somewhat random for background events, which are reconstructed under a false hypothesis.
- **rec\_pi0\_impact:** The impact parameter of the reconstructed  $\pi^0$ . Expected to be small for signal events and larger for background events, which are reconstructed under a false hypothesis.
- **g\_cand\_totmom:** The total momentum of all gamma candidates. Expected to peak around  $206 \text{ MeV}/c$  for signal events, where it is assumed that both true gamma rings are reconstructed as a single ring in events with only one gamma candidate. Background events, which do not contain monochromatic pions produced by kaon decay, are expected to have a random distribution.

### Variables related to the reconstructed momentum

- **k\_cand\_mom[0,1]:** The reconstructed momentum of the kaon candidates. Expected to peak roughly around  $800 \text{ MeV}/c$  for signal events, and have a random distribution for background events, which almost never even contain true kaons.

- **mu\_cand\_mom[0,1]:** The reconstructed momentum of the muon candidates. Expected to peak at 236 MeV/ $c$  for signal events, and have a random distribution for background events, which do not contain monochromatic muons produced by kaon decay.
- **g\_cand\_mom[0,1]:** The reconstructed momentum of the gamma candidates. Expected to have a distribution consistent with a monochromatic  $\pi^0$  with a momentum of 207 MeV/ $c$  (about 20–230 MeV/ $c$ ) for signal events, and have a random distribution for background events, which do not contain monochromatic pions produced by kaon decay.

#### Variables related to the reconstructed Cherenkov angle

- **k\_cand\_cang[0,1]:** The reconstructed Cherenkov angle of the kaon candidates. Expected to be roughly around  $30^\circ$  for signal events, and have a random distribution for background events, which almost never even contain true kaons, let alone kaons produced by dinucleon decay.
- **mu\_cand\_cang[0,1]:** The reconstructed Cherenkov angle of the muon candidates. Expected to be roughly around  $35^\circ$  for signal events, and have a random distribution for background events, which do not contain monochromatic muons produced by kaon decay.
- **g\_cand\_cang[0,1]:** The reconstructed Cherenkov angle of the gamma candidates. Expected to be roughly around  $42^\circ$  for signal events, and have a somewhat more random distribution for background events, which may contain pions, but are reconstructed under a false hypothesis.

### Variables related to the showering likelihood

- **k\_cand\_show[0,1]**: The showering likelihood of the kaon candidates. Expected to have a clear peak in the positive (non-showering) region for signal events, and have a somewhat more random distribution for background events, which are reconstructed under a false hypothesis.
- **mu\_cand\_show[0,1]**: The showering likelihood of the muon candidates. Expected to have a clear peak in the positive (non-showering) region for signal events, and have a somewhat more random distribution for background events, which are reconstructed under a false hypothesis.
- **g\_cand\_show[0,1]**: The showering likelihood of the gamma candidates. Expected to have a clear peak in the negative (showering) region for signal events, and have a somewhat more random distribution for background events, which are reconstructed under a false hypothesis.

### Variables related to the event geometry

- **mu\_cand\_impact[0,1]**: The impact parameter of the muon candidates. Expected to be small for signal events and larger for background events, which are reconstructed under a false hypothesis.
- **g\_cand\_impact[0,1]**: The impact parameter of the gamma candidates. Expected to be small for signal events and larger for background events, which are reconstructed under a false hypothesis.
- **decay\_vtxsep**: The separation between the reconstructed vertices of the kaon decay product vertices. Expected to be large (around 2.6 m) for signal events,

and smaller in background events, which have one true vertex. This variable is fairly accurate for background events despite their being reconstructed under a false hypothesis. Their accuracy is due to the fact that the decay product candidates are more likely to be correctly labeled as gammas and muons, thus yielding accurate reconstructed information.

### Variables related to the light pattern and the single vertex hypothesis

- **total\_rtot\_mag:** The magnitude of the vector sum of the light contained in each ring from the event vertex ( $RTOT$ ). Expected to be small in signal events due to the symmetry of the light pattern and larger in background events, which tend to be less symmetric.
- **total\_rtot\_dot\_k:** The magnitude of the vector sum of the light contained in each ring from the event vertex (called “rtot”) along the direction of the brightest kaon candidate ring. Expected to be small in signal events due to the back-to-back kaon rings of very similar momenta, and larger in background events, which lack this feature.
- **agood:** The goodness of the standard vertex fitter, which assumes the event has only one true vertex. Expected to be small for signal events, which have three true vertices, and larger for background events, which have one true vertex.
- **off\_vtx\_sep:** The separation between the standard (“official”) reconstructed event vertex and the dinucleon decay hypothesis event vertex. Expected to be small for signal events due to the symmetry of the underlying event geometry, and larger in background events, which are less symmetric and reconstructed under a false hypothesis.

### Variables related to the decay electrons

- **n\_dcy\_e:** The number of found decay electrons. Expected to be larger for signal events, which produce two true decay electrons, and smaller for background events, which tend to produce fewer true decay electrons.
- **dcy\_e\_vtxsep:** The separation between the vertices of the found decay electrons. Expected to be large (around 2.6 m) for signal events, and small ( $\sim 0$  m) for background events, which do not have true separated pion or muon vertices.

Figure 9.10 shows the input variable distributions for the analysis sample of the  $pp \rightarrow K^+ K^+$  signal Monte Carlo, the analysis sample of the atmospheric neutrino background Monte Carlo, and the SK-I data. The data and atmospheric neutrino Monte Carlo are in good agreement overall.

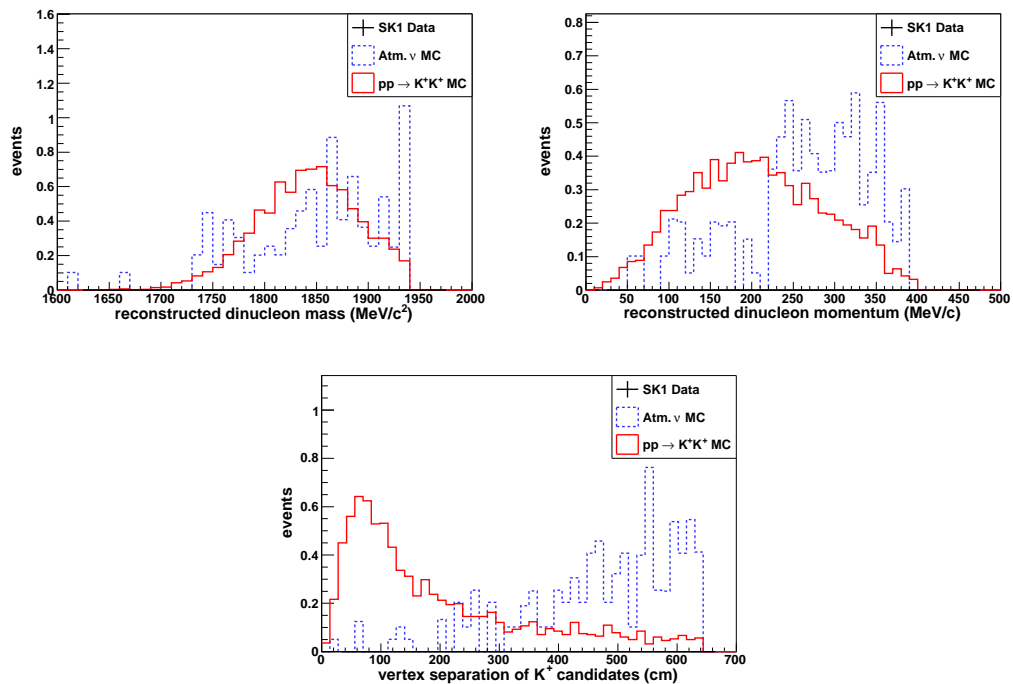


**Figure 9.10:** Distributions of the boosted decision tree input variables used to perform the final analysis. Trivial bins have not been plotted. The solid line represents the  $pp \rightarrow K^+K^+$  Monte Carlo, the dashed line represents the atmospheric neutrino Monte Carlo, and the crosses represent the SK-I data. This set of plots shows variables related to the reconstructed dinucleon pair. No data events were found to have two kaon candidates, thus there are no data entries in this set of plots.

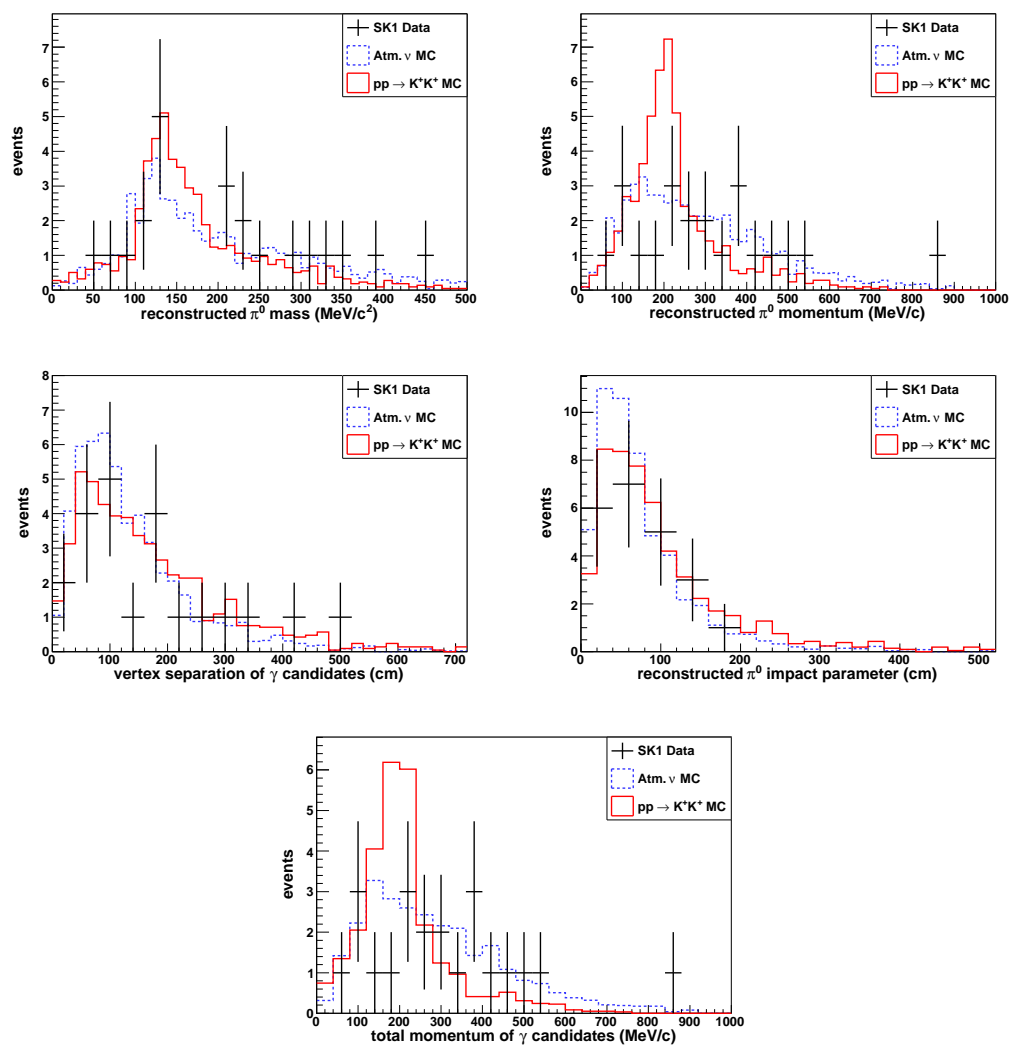


Figure 9.10: (Continued...) This set of plots shows variables related to the reconstructed  $\pi^0$ .

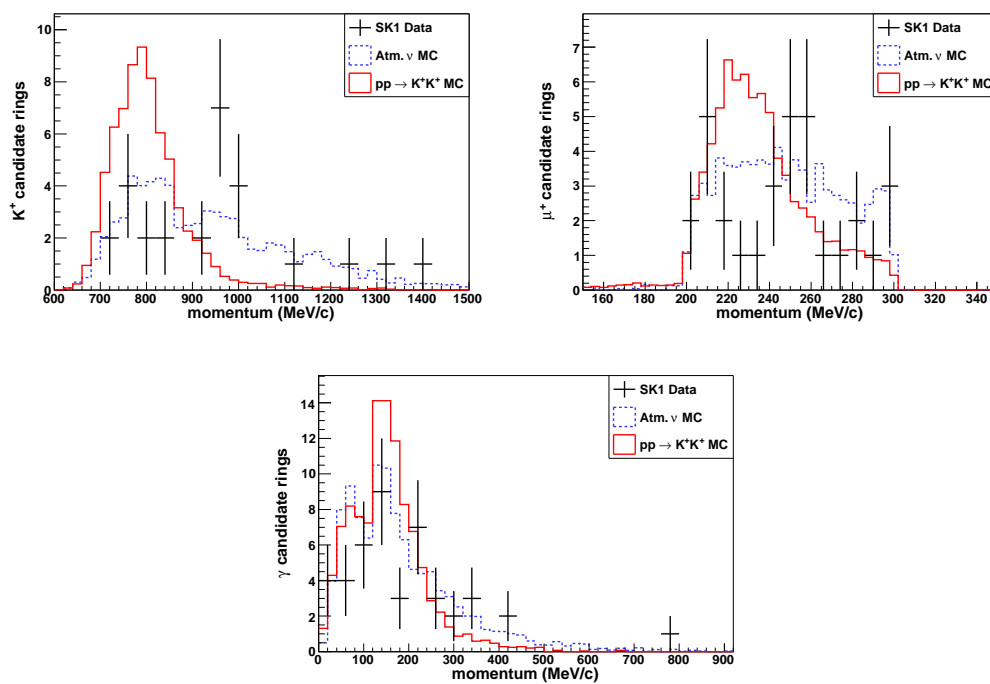


Figure 9.10: (Continued...) This set of plots shows the reconstructed momenta.

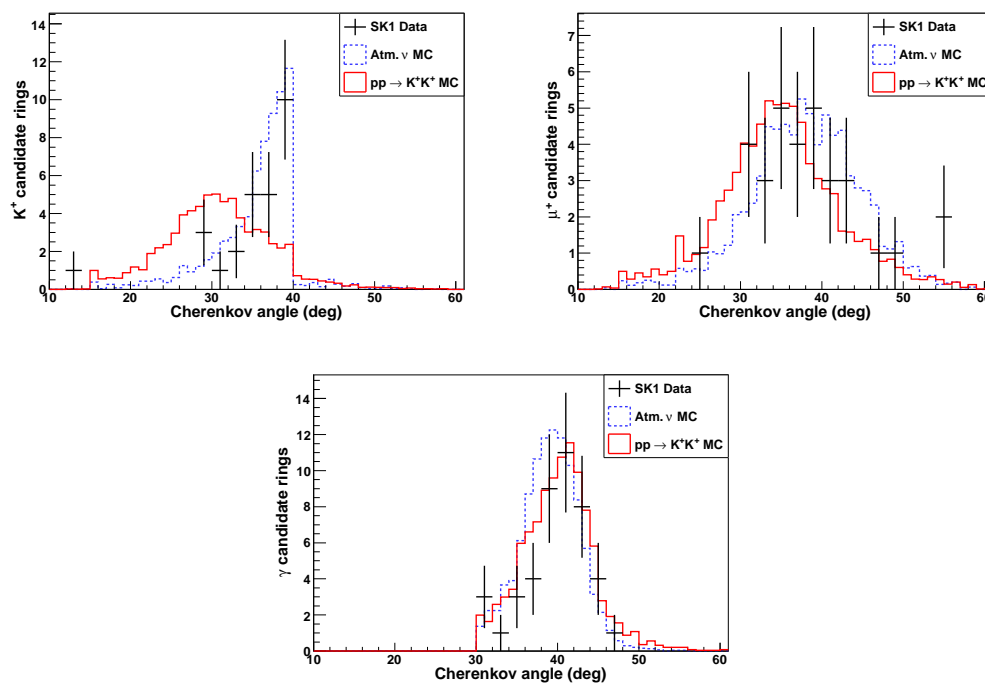


Figure 9.10: (Continued...) This set of plots shows the reconstructed Cherenkov angles.

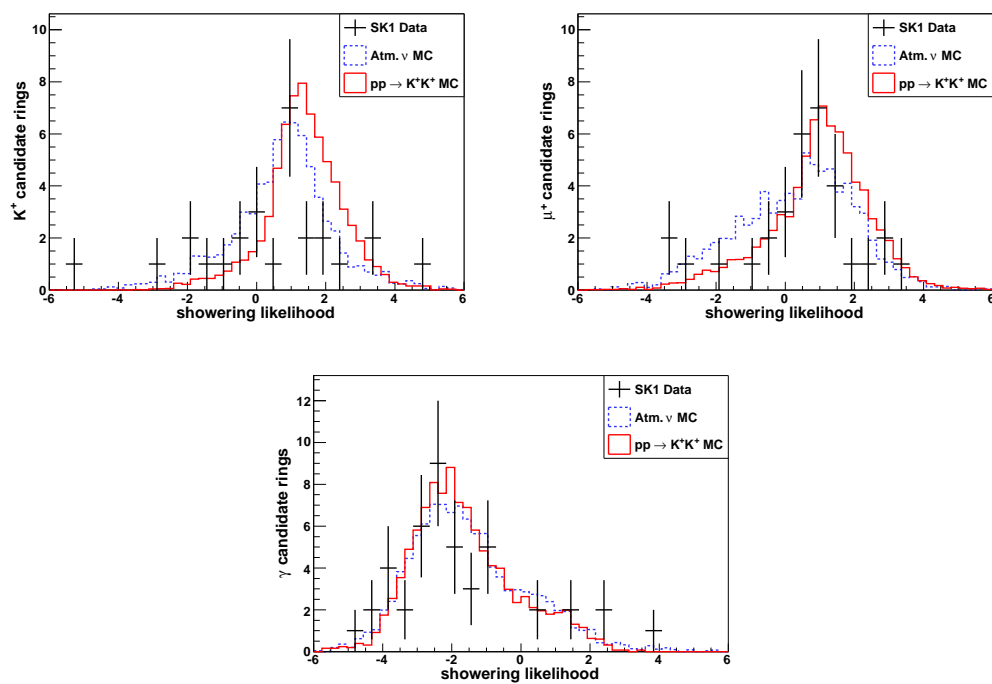
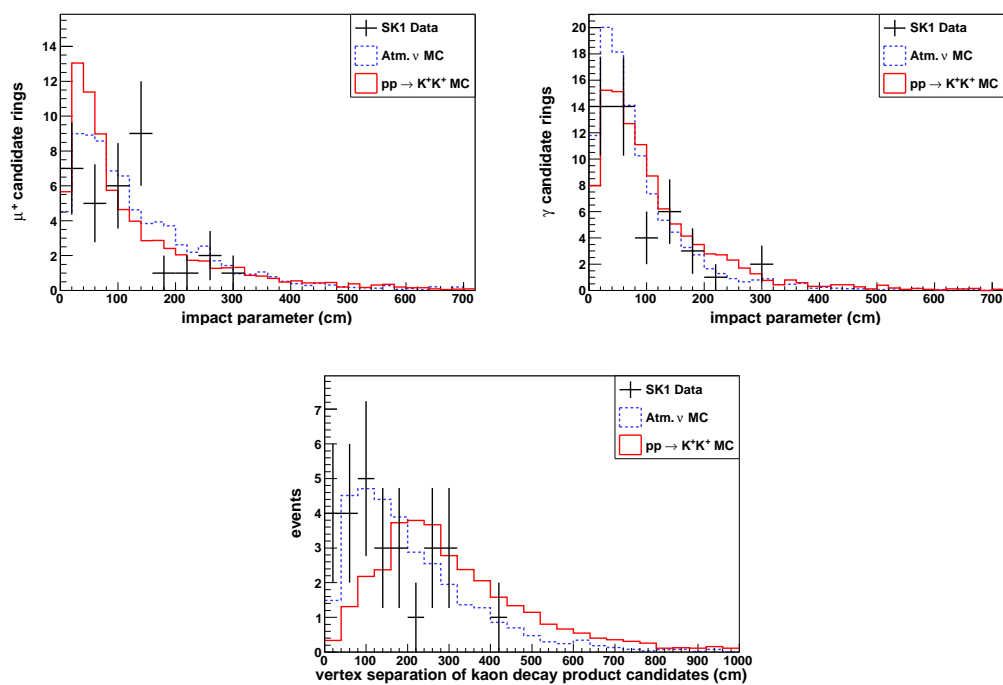
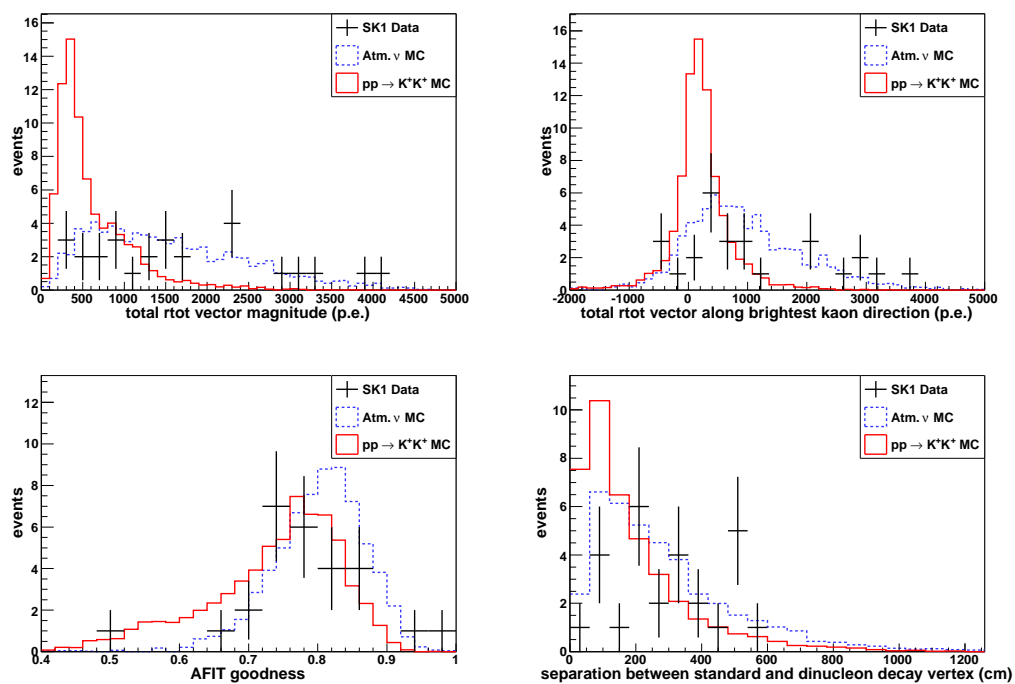


Figure 9.10: (Continued...) This set of plots shows the showering likelihoods.



**Figure 9.10:** (Continued...) This set of plots shows variables related to the geometry of the event.



**Figure 9.10:** (Continued...) This set of plots shows variables related to the symmetry of the light pattern of the event, and the fitting goodness using a single vertex hypothesis.

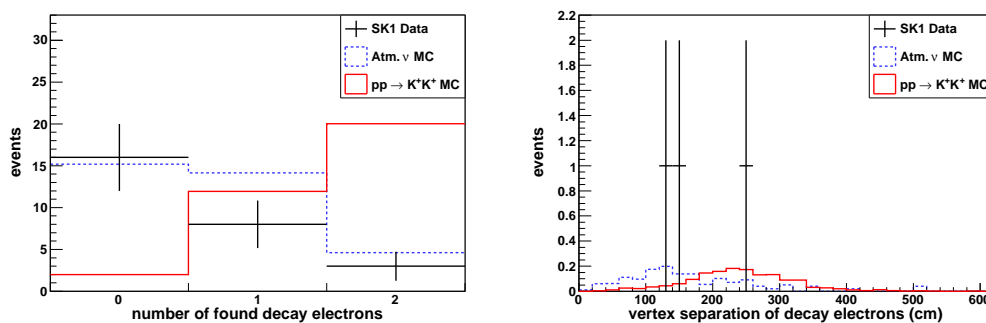


**Figure 9.10:** (Continued...) This set of plots shows variables related to the found decay electrons in the event.

### 9.4.2 Training and Testing of the Boosted Decision Tree

A boosted decision tree is a collection of individual decision trees that are created in an iterative process one after another, each using reweighted training events based on the performance of the previous tree in the chain. The complete collection of individual decision trees is referred to as the forest. The details of the boosted decision tree and how it is trained are described in further detail in Appendix B.

Figure 9.11 shows one of the decision trees from the forest of the boosted decision tree used in this analysis. In this diagram, events start at the top node and travel down the diagram until reaching one of the “signal-like” or “background-like” terminal “leaf” nodes. An event which passes the cut at a given node is considered signal-like, and travels to the right to the next node. Likewise, an event which fails the cut at a given node is considered background-like, and travels to the left to the next node. The output of each individual decision tree is  $+1$  or  $-1$ , depending on whether the path traversed by an event ends on a signal-like or background-like terminal leaf node, respectively.

When using the boosted decision tree to perform an analysis, each event fed in to the boosted decision tree is evaluated by every tree in the forest, and the final output of the boosted decision tree is given by the sum of each of the outputs of the individual decision trees, weighted by a “boost-weight” that is associated with each tree. The expression for the output, which is also described in Section B.1, is:

$$y_{\text{BDT}}(x) = \sum_{i \in \text{forest}} \ln(\alpha_i) \cdot h_i(x), \quad (9.1)$$

where  $x$  is the tuple of input variables, and  $h_i(x)$  and  $\alpha_i$  are the output and weight of the individual trees, respectively. The boost-weight of an individual tree is determined during the training phase, and essentially measures the tree’s overall performance in

separating signal from background. It is described in detail in Section B.3.

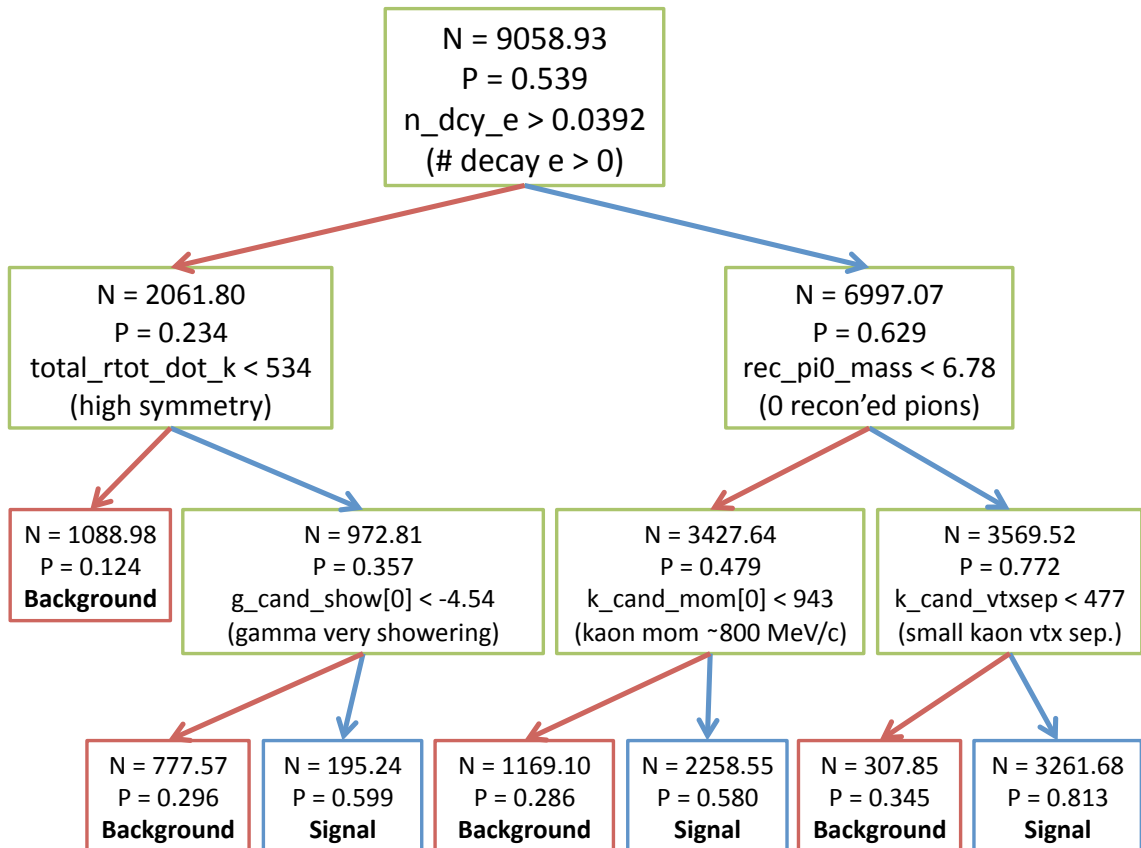


**Figure 9.11:** One of the decision trees from the boosted decision tree forest that was used in this analysis. The variable and cut value used at each branching node is depicted, along with an interpretation of the cut.  $N$  is the total weighted number of events at a given node.  $P$  is the signal purity of the node, defined as  $P = S/(S+B)$ , where  $S$  is the weighted number of true signal events at the node and  $B$  is the weighted number of true background events at the node. **Signal** and **Background** indicate a terminal signal-like and background-like leaf node, respectively.

The goal of the testing stage was to adjust the tuning parameters of the boosted decision tree to produce output for the signal and background Monte Carlo that satisfied certain criteria that were decided upon beforehand. The criteria chosen for this analysis required that the output distributions have the following qualities: (1) good overall separation between signal and background; (2) overall smoothness with no large and/or irregularly exaggerated jaggedness in either the signal or background

distribution; (3) relative smoothness in the background and signal distributions near the signal-like tail region of the background distribution. The emphasis on the signal-like tail region of the background is due to the fact that this is approximately where the final cut will be placed, as this search was intended to be a zero background search. Thus it was considered desirable to have well-behaved output distributions in that region in order to reduce systematic errors that could arise from fluctuations in the data.

The tuning parameters were adjusted through an iterative trial process until the criteria listed above were met. The three parameters which were tuned in the process were the total number of trees in the forest, the minimum number of events in a terminal node, and the pruning strength. The final configuration of the boosted decision tree is presented in Table 9.8.

Number of trees:	500
Min. events per leaf:	1
Boost type:	Ada-Boost
Separation type:	Gini Index
Number of bins:	50
Pruning method:	Cost Complexity
Pruning strength:	25.0

**Table 9.8:** Configuration of the boosted decision tree.

The outputs of the training, testing, and analysis stages are compared in Fig. 9.12. The shape difference between the training and testing samples indicated that the boosted decision tree was slightly overtrained on the training sample, meaning that the separation between the training signal and background distributions was somewhat better than that of the testing distributions. This does not indicate that the boosted decision tree would have inconsistent results from sample to sample, however, which is the primary concern regarding potential bias in the performance. A

very large degree of overtraining would indicate that the performance of the boosted decision tree will not be optimal when applied to samples that were not used in the training itself [74].

To check for consistent performance of the boosted decision tree on samples that were not used in the training process, the output of the testing sample and the output of the analysis sample were compared. Figure 9.12 demonstrates that the boosted decision tree performance was consistent across statistically similar samples of events.

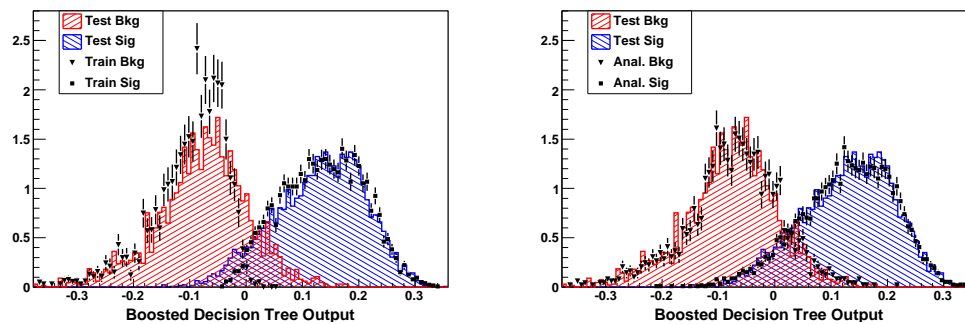


**Figure 9.12:** Comparisons of training, testing, and analysis outputs from the boosted decision tree. Left: boosted decision tree output for signal and background training samples (markers) and testing samples (hatched). Disagreement indicates slight (though non-problematic) overtraining of the boosted decision tree. Right: Boosted decision tree output for analysis samples (markers) and testing samples (hatched). Agreement indicates consistent performance of the boosted decision tree on statistically similar datasets.

### 9.4.3 Final Cut Placement for Boosted Decision Tree Output

The final stage of the multi-variate analysis was to assess the boosted decision tree output for the analysis sample of the signal and background Monte Carlo, and to choose the placement of the final cut that would be used to determine whether or not there was evidence for any signal events in the actual SK-I dataset.

The starting point for determining the final cut placement was to determine the point which maximized the significance, defined as  $S/\sqrt{S+B}$ , where  $S$  is the signal

efficiency and  $B$  is the background efficiency, for 1 signal event over 26 background events using the testing Monte Carlo samples, which would correspond to seeing 1 signal event in the 27 SK-I data events that passed the precuts. The significance curve for these parameters is shown in Fig. 9.13. The significance was found to be maximal for a cut placed at about 0.12.

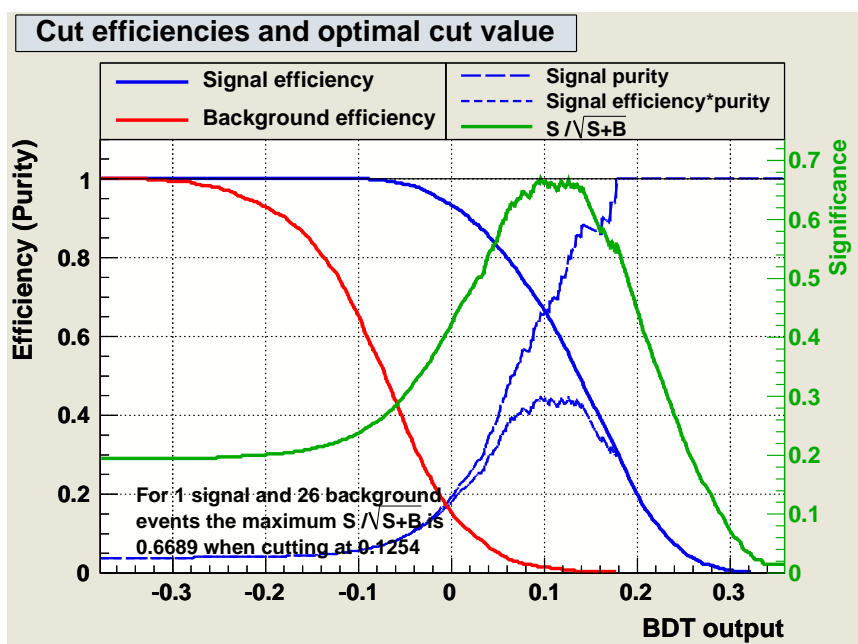


**Figure 9.13:** Significance curve for the boosted decision tree output determined by testing Monte Carlo for 1 signal event over 26 background events. The significance is defined as  $S/\sqrt{S+B}$ . The maximum significance is attained for a cut placed at about 0.12.

The signal efficiency and expected background values corresponding to a cut placed at 0.12 were calculated using the analysis Monte Carlo sample. The cut value was then incremented by steps of 0.01, the chosen granularity for the final cut placement. Table 9.9 shows the signal efficiency and expected background for a number of potential cut placements that were considered. The final cut placement was chosen to be 0.12, yielding a signal efficiency of 12.6% and an expected background of 0.28 events. It was decided to move the cut no lower than this due to the goal of having

zero background in the final analysis of the data. An expected background of 0.3 events or higher was deemed to be too large, given that the systematic errors on the background estimate were expected to be somewhat large.

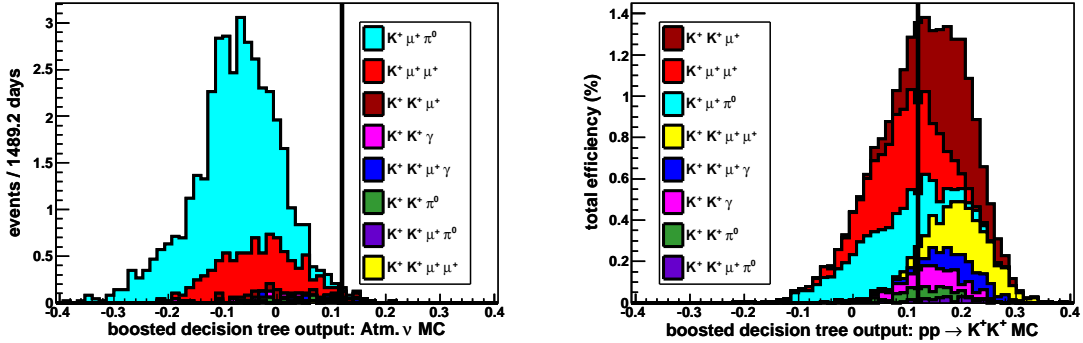
Cut Placement	Signal Efficiency	Expected Background
0.10	14.4%	0.51 evt./1489.2 days
0.11	13.5%	0.38 evt./1489.2 days
<b>0.12</b>	<b>12.6%</b>	<b>0.28 evt./1489.2 days</b>
0.13	11.5%	0.19 evt./1489.2 days
0.14	10.4%	0.16 evt./1489.2 days

**Table 9.9:** Signal efficiency and expected background for different final cut placements on the boosted decision tree output. Figures were calculated using the analysis Monte Carlo sample. 0.12 was chosen for the final cut placement to be used in the analysis of the data.

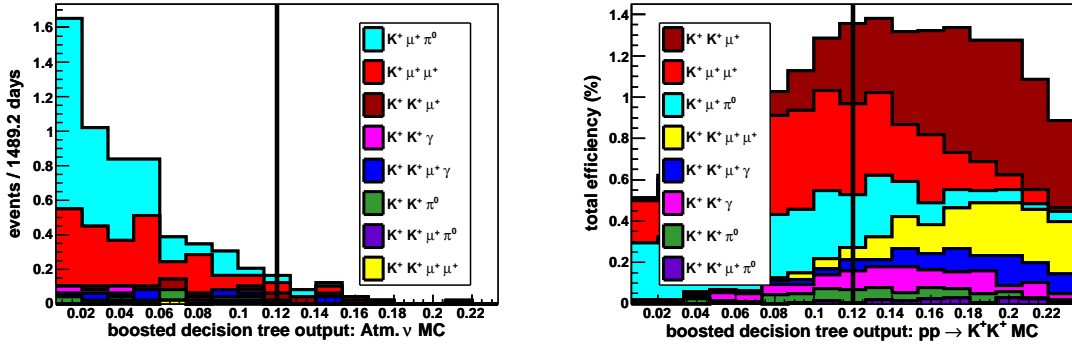
#### 9.4.4 Boosted Decision Tree Monte Carlo Results

Figure 9.14 shows the boosted decision tree output of the atmospheric neutrino and  $pp \rightarrow K^+ K^+$  analysis Monte Carlo samples. The results are color-coded by event category. Figure 9.15 shows an enlarged view of the Monte Carlo output in the region near the final cut, placed at 0.12. Events in the data with a final output greater than the cut value would be considered dinucleon decay signal candidates. The color legend in both figures list the event categories by decreasing abundance in each respective plot.

The final signal efficiency and expected background after applying the boosted decision tree cut are shown in Table 9.10. The final total efficiency for the signal after applying the boosted decision tree cut was 12.6%. The final total expected background was 0.28 events after normalizing to the SK-I livetime.



**Figure 9.14:** Boosted decision tree output for the Monte Carlo. Left: Atmospheric neutrino Monte Carlo. Right:  $pp \rightarrow K^+ K^+$  Monte Carlo. The legend lists the event categories by decreasing abundance in each respective plot. The vertical line indicates the final cut, placed at 0.12.



**Figure 9.15:** Boosted decision tree output for the Monte Carlo in the region near the final cut. Left: Atmospheric neutrino Monte Carlo. Right:  $pp \rightarrow K^+ K^+$  Monte Carlo. The vertical line indicates the final cut, placed at 0.12.

### 9.4.5 Final Background Characteristics

Table 9.11 shows the surviving background Monte Carlo events after applying the boosted decision tree cut, broken down by neutrino flavor and weak current type. Charged current (CC) and neutral current (NC) muon neutrino interactions dominate the background after the precuts.

Table 9.12 shows the specific neutrino interaction types of the final surviving background Monte Carlo. Single-pion and multi-pion production from delta resonance

Event Category	$pp \rightarrow K^+ K^+$ M.C. efficiency (%)	Atmospheric $\nu$ M.C. events / SK-I livetime
$K^+ K^+ \mu^+$	5.0	0.07
$K^+ \mu^+ \mu^+$	1.8	0.08
$K^+ K^+ \gamma$	0.8	0.02
$K^+ K^+ \mu^+ \mu^+$	2.5	0.00
$K^+ K^+ \gamma \gamma$	0.3	0.00
$K^+ \mu^+ \gamma \gamma$	1.0	0.08
$K^+ K^+ \mu^+ \gamma$	1.0	0.03
$K^+ K^+ \mu^+ \gamma \gamma$	0.2	0.00
total	12.6	0.28

**Table 9.10:** Signal and background after applying the boosted decision tree cut.

$\nu$ Mode	Events/200 Years	Events/1489.2 Days	%
CC $\nu_\mu$	8.73	0.18	64
NC $\nu_\mu$	3.00	0.06	22
CC $\nu_e$	2.00	0.04	15
NC $\nu_e$	0.00	0.00	0
total	13.73	0.28	100

**Table 9.11:** Final remaining background Monte Carlo events sorted by neutrino flavor and weak current type. CC: Charged Current; NC: Neutral Current. The first numerical column shows the unscaled number of events from the 200 year analysis sample. The second numerical column shows the number of events scaled to the SK-I livetime.

are the dominant sources of background after the final cut on the boosted decision tree output.

Table 9.13 shows the breakdown of the true particle types (PID) for each of the different ring classifications from the final background sample. A plurality of the kaon candidate rings were created by muons. The rest were mostly created by charged pions and protons. Half of the muon candidate rings were created by charged pions. A majority of the gamma candidate rings were created by actual gammas.

Interaction	Events/200 Years	Events/1489.2 Days	%
CC multi-pion production	5.34	0.11	38.9
CC single pion delta resonance	4.89	0.10	35.6
NC single pion delta resonance	2.00	0.04	14.6
NC diffractive pion production	1.00	0.02	7.3
CC quasi-elastic	0.50	0.01	3.6
NC multi-pion production	0.00	0.00	0.0
CC diffractive pion production	0.00	0.00	0.0
NC elastic	0.00	0.00	0.0
CC coherent pion production	0.00	0.00	0.0
NC coherent pion production	0.00	0.00	0.0
total	13.73	0.28	100

**Table 9.12:** Final remaining background Monte Carlo events sorted by neutrino interaction type. CC: Charged Current; NC: Neutral Current. The first numerical column shows the unscaled number of events from the 200 year analysis sample. The second numerical column shows the number of events scaled to the SK-I livetime.

True PID	$K^+$ Candidates	$\mu^+$ Candidates	$\gamma$ Candidates
$p$	5	5	0
$\pi^\pm$	8	11	1
$\mu^\pm$	12	2	0
$e^\pm$	1	1	3
$\gamma$	1	3	6
total	27	22	10

**Table 9.13:** True PID of all rings in final background sample.

### 9.4.6 Final Signal Characteristics

Table 9.14 shows the breakdown of the true particle types (PID) for each of the different ring classifications from the final signal sample. The kaon candidates had a purity of 92.6%, the muon candidates had a purity of 81.8%, and the gamma candidates had a purity of 67.4%. These high purities show that the classification algorithm performed quite well on the dinucleon decay signal Monte Carlo events.

Table 9.15 shows the purity of each of the event categories for the final signal

True PID	$K^+$ Candidates	$\mu^+$ Candidates	$\gamma$ Candidates
$K^+$	4273	276	27
$\pi^+$	57	128	32
$\mu^+$	224	2668	200
$e^+$	19	51	62
$\gamma$	42	138	663
total	4615	3261	984
purity	92.6%	81.8%	67.4%

**Table 9.14:** True PID of all rings in final signal sample.

sample. The purity is defined here as the fraction of events of a given category in which every ring in the event was correctly classified. The final entry represents the total purity of the final signal sample across all categories. The  $K^+ K^+ \mu^+$  and  $K^+ K^+ \mu^+ \mu^+$  categories both had very high purity; these represent the majority of the events in the final signal sample. The good performance in these categories is due to the two found kaons. The rest of the categories had purities ranging from 30-50%. The reason that these categories had somewhat worse purities than  $K^+ K^+ \mu^+$  and  $K^+ K^+ \mu^+ \mu^+$  is that they either were missing the second kaon ring, or because they contained gamma candidate rings, which have a worse purity than either kaon or muon candidate rings. Having correctly classified every ring in about two-thirds of the final signal sample is here considered a very good performance benchmark, given the highly complicated nature of the signal events and the ring classification algorithm that it entailed.

## 9.5 Systematic Uncertainties

The systematic uncertainties were broken down into four main categories: Monte Carlo simulation, detector knowledge, event reconstruction, and boosted decision tree

Event Category	Purity
$K^+ K^+ \mu^+$	84.7%
$K^+ \mu^+ \mu^+$	43.5%
$K^+ K^+ \gamma$	39.6%
$K^+ K^+ \mu^+ \mu^+$	81.7%
$K^+ K^+ \gamma \gamma$	41.8%
$K^+ \mu^+ \gamma \gamma$	31.1%
$K^+ K^+ \mu^+ \gamma$	32.5%
$K^+ K^+ \mu^+ \gamma \gamma$	48.7%
overall	65.5%

**Table 9.15:** Event categorization purity for the final signal sample.

related uncertainties. The first category, Monte Carlo simulation, had a unique set of uncertainties for the signal efficiency and expected background. The latter three categories were common to both signal and background.

### 9.5.1 Monte Carlo Simulation Uncertainties

#### Signal

The four main sources of uncertainty from the Monte Carlo for the signal efficiency were from hadronic interactions of the kaons, the simulation of correlated decay events, the Fermi momentum of the parent nucleons, and the branching ratios of the kaon decay channels.

Based on cross-section comparisons between the dinucleon decay Monte Carlo and those compiled by the PDG [12], the systematic uncertainty for hadronic interactions of the kaons was estimated to be 25%. Figure 5.4 shows the cross-sections from the  $pp \rightarrow K^+ K^+$  Monte Carlo overlaid on the experimental data points taken from the PDG.

The effect of correlated decay is described in Section 5.1. A 100% systematic

uncertainty was taken for this effect. The uncertainty in the Fermi momentum was taken to be 20%, following [4]. The uncertainty on the kaon branching ratios was assumed to be negligibly small.

## Background

For the atmospheric neutrino background, there were also four main systematic uncertainty terms taken into account. All four of these effects were taken to have a direct effect on the final background uncertainty. The neutrino flux was taken to have an 8% uncertainty, the neutrino interaction cross-section 15%, nuclear effects were taken to have a 20% uncertainty, and pion propagation simulation uncertainties, which are the dominant source overall in the background estimate uncertainty, were taken to have a 50% uncertainty. All of these uncertainties follow the general prescriptions laid out in previous Super-Kamiokande studies [4, 57].

### 9.5.2 Detector Related Uncertainties

There were two main systematic uncertainties related to detector knowledge: the uncertainty in the fiducial volume and the energy scale.

A 4.4% uncertainty in the fiducial volume was taken for signal and background, based on comparisons between the data and atmospheric Monte Carlo, which corresponded with a shift in the fiducial volume boundary cut of 200 cm (+22.2 cm or -21.5 cm) from the inner wall of the detector.

The energy scale uncertainty was also estimated based on comparisons between data and atmospheric neutrino Monte Carlo, and was estimated to be at the 1.1% level. A corresponding 1.1% shift in the *POTOT* precut (Section 9.3) was used to estimate the overall uncertainty in the signal and background based on the energy

scale uncertainty.

### 9.5.3 Reconstruction Uncertainties

Six major sources of uncertainty were identified from the event reconstruction process: showering likelihood, ring counting, Cherenkov angle, vertex position, decay electron counting, and ring momentum reconstruction. The estimated size of the uncertainties for each of these sources is summarized in Table 9.16. The same values were used for both signal and background uncertainty estimates.

Systematic Source	Uncertainty
showering likelihood	5.8% (0.2)
ring counting	< 1%
Cherenkov angle	0.7°
vertex position	30 cm
decay-e counting	~ 1%
ring momentum	1.2%

**Table 9.16:** Systematic uncertainties in event reconstruction variables.

Each of the respective variables was shifted by its corresponding uncertainty, and the entire search process was re-run on the shifted Monte Carlo, from the ring classification to the boosted decision tree. The boosted decision tree was not re-trained for each shifted sample; the original boosted decision tree trained on the unshifted Monte Carlo was used to estimate all uncertainties.

### 9.5.4 Search Method Uncertainties

Finally, to attempt to estimate the systematic uncertainties introduced by the boosted decision tree, several techniques were used, and the results of each were averaged independently for the signal and background. The first technique was to

simply shift the final cut placement up and down by an increment of 0.01. This was the granularity used when choosing the original cut placement, as described in Section 9.4.3.

The second technique was to assess the final signal efficiency and expected background after applying the trained boosted decision tree to the testing Monte Carlo sample (see Section 9.4.2), and then the combined testing and analysis samples, simultaneously.

The results of these tests are summarized in Table 9.17. The average uncertainty of the two techniques was taken as the final uncertainty of the boosted decision tree performance.

	Cut Variation	Sample Variation	Average
$pp \rightarrow K^+ K^+$	8.1%	1.4%	4.7%
Atm. $\nu$	33.9%	26.8%	30.4%

**Table 9.17:** Systematic uncertainty of boosted decision tree performance.

### 9.5.5 Total Systematic Uncertainty

The final systematic uncertainties are listed in Table 9.18. The total uncertainty on the signal detection efficiency was calculated to be 25.2%. The total uncertainty on the expected background was calculated to be 68.1%. The leading sources of uncertainty for both the signal efficiency and the expected background came from the respective Monte Carlo simulations. For the signal, the uncertainty in the simulation of the Fermi momentum of the original nucleons dominated. For the background, the uncertainty in the simulation of the propagation of pions was the dominant source.

Systematic Source	$\sigma[\epsilon_{\text{sig}}]$	$\sigma[N_{\text{bkg}}]$
<b><math>pp \rightarrow K^+ K^+</math> Monte Carlo</b>		
hadronic interactions	1.3%	
correlated decay	2.5%	
Fermi momentum	24.1%	
$K^+$ decay B.R.	< 1%	
<b>Atm. <math>\nu</math> Monte Carlo</b>		
$\nu$ flux		8.0%
$\nu$ cross-section		15.0%
$\pi$ nuclear effect		20.0%
pion propagation		50.0%
<b>Detector Knowledge</b>		
fiducial volume	2.2%	5.4%
energy scale	< 1%	< 1%
<b>Event Reconstruction</b>		
showering likelihood	2.4%	14.3%
ring counting	< 1%	< 1%
Cherenkov angle	1.0%	3.6%
vertex position	3.9%	16.1%
decay-e counting	< 1%	< 1%
ring momentum	0.7%	5.4%
<b>Boosted Decision tree</b>		
sample bias	4.7%	30.4%
<b>total</b>	<b>25.2%</b>	<b>68.1%</b>

**Table 9.18:** Systematic uncertainties in event reconstruction variables.

## Chapter 10

# Results and Conclusions

The 1489.2 days of fully contained SK-I data, corresponding to 91.7 kiloton · years of exposure, were searched for evidence of  $^{16}\text{O}(pp) \rightarrow ^{14}\text{C} K^+ K^+$ . Twenty-seven events in the data passed the precuts described in Section 9.3. Figure 10.1 shows the final results of the search. No signal candidate events were found in the data, defined by the final cut on the boosted decision tree output at 0.12. The distribution of the boosted decision tree output for the SK-I data was found to be consistent with the atmospheric neutrino Monte Carlo, representing the background of the search.

The amount of background expected to pass the final cut was  $0.28 \pm 0.19$  events after normalizing to the 1489.2 days of SK-I livetime. The  $pp \rightarrow K^+ K^+$  signal detection efficiency was estimated to be  $12.6\% \pm 3.2\%$ .

Following the conventions described in Appendix C.1, the results of the search were used to calculate a lower limit on the partial lifetime of the dinucleon decay channel  $pp \rightarrow K^+ K^+$ :

$$\frac{\tau}{B.R._{pp \rightarrow K^+ K^+}} \geq 1.7 \times 10^{32} \text{ years.} \quad (10.1)$$

This number represents the lifetime limit per  $^{16}\text{O}$  nucleus at a 90% confidence level.

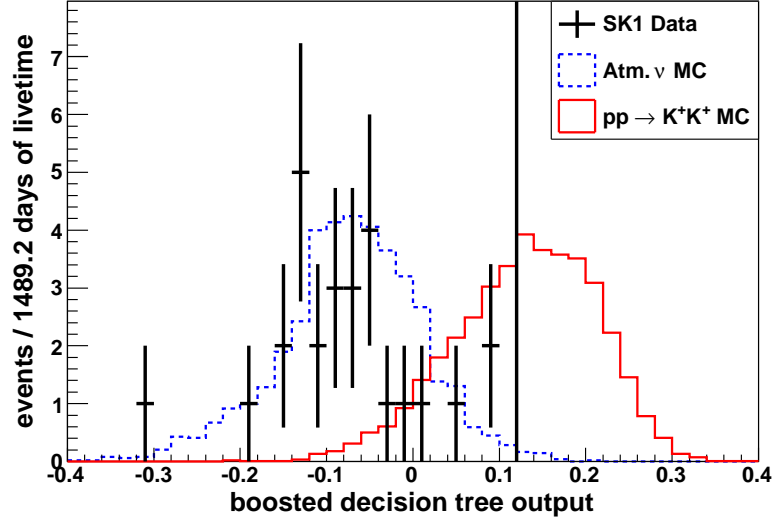


**Figure 10.1:** Final output of boosted decision tree. SK-I data is overlaid on analysis Monte Carlo samples of the dinucleon decay signal and the atmospheric neutrino background. The final cut placement is at 0.12; events with an output above this threshold are considered signal candidates. No signal candidate events were found in the data.

The limit presented in this dissertation is the result of the first direct experimental search for dinucleon decay into kaons. This limit is two orders of magnitude better than the dinucleon decay limits for pion and lepton modes set by the Frejus experiment [12, 15], and seven orders of magnitude better than the limits for neutrino modes and invisible modes set by Frejus, DAMA, and the BOREXINO CTF [12–15].

Using the lower lifetime limit from the search, one can then calculate the corresponding upper limit on the magnitude of the  $\Delta B = 1$   $R$ -Parity violating SUSY parameter,  $\lambda''_{uds}$ . The details of the calculation are described in Appendix C.2. The upper limit on the  $\lambda''_{uds}$  parameter based on the first experimental lower lifetime limit for the dinucleon decay channel  $pp \rightarrow K^+ K^+$  was calculated to be:

$$|\lambda''_{uds}| < \left( \frac{0.64}{\tau [\text{years}]} \right)^{1/4} = 7.8 \times 10^{-9}. \quad (10.2)$$

This new result is more restrictive than the limit of  $\sim 10^{-7}$  estimated by Goity and Sher [22] based on a typical nuclear matter lifetime limit of  $\sim 10^{30}$  years taken from the limits observed in searches for single nucleon decay and the searches for dinucleon decay into pions or leptons performed by the Frejus collaboration.

According to the literature [20–22], a search for dinucleon decay into kaons should provide the best currently accessible experimental limit on  $\lambda''_{uds}$ . Because  $\lambda''_{uds}$  scales with  $\tau^{-1/4}$ , and  $\tau \propto \epsilon \cdot A$ , where  $\epsilon$  is the signal detection efficiency and  $A$  is the exposure in kiloton  $\cdot$  years, one would need to increase  $\epsilon \cdot A$  by a factor of 10,000 to improve the limit calculated in this analysis by a single order of magnitude. Thus, adding the SK-II and SK-III datasets to the search would do little to improve the limit obtained here from the SK-I dataset alone.

In regard to the ability of future experiments to improve the  $\lambda''_{uds}$  limit presented here by an order of magnitude, it seems that it would be very difficult to accomplish using conventional nucleon decay detection methods, though perhaps not strictly impossible. Certainly, the target mass of the detector (or set of detectors) would have to be in the range of megatons. Until such a detector exists, however, the new limit on  $\lambda''_{uds}$  presented in this dissertation is expected to remain the best limit on record.

## Appendix A

# MVFIT Resolutions

The resolution for each reconstructed variable was obtained separately for the  $pp \rightarrow K^+ K^+$  Monte Carlo and the atmospheric  $\nu$  Monte Carlo. Three of the precuts listed in Section 9.3 were applied to both Monte Carlo samples before calculating the resolutions:

- $1000 < potot < 11000$ , where  $potot$  is the total amount of light seen in the ID in units of p.e.
- $3 \leq nring \leq 5$ , where  $nring$  is the number of found rings in the event
- $wall > 200$  cm, where  $wall$  is the distance from the event vertex to the nearest wall; this is the fiducial volume (FV) cut

A correction of +4.5%, +0.5%, and +5.0% was applied to the kaon-like, muon-like, and gamma-like reconstructed momenta, respectively. These corrections compensate for the bias arising from the RTOT-to-momentum look-up tables used in the momentum reconstruction process (see Section 7.1.4), which were generated for RTOT values corresponding to a  $70^\circ$  half-opening angle. The RTOT value used in MVFIT

is instead calculated using the unmasked window, defined as the ring's Cherenkov angle  $+10^\circ$  (see Section 7.2).

A correction of -5 cm and -40 cm was also applied to the reconstructed vertex along the ring direction for muon-like and gamma-like vertices, respectively. This was again to compensate for bias introduced by using reconstruction algorithms that were not originally developed to perform with the light masking techniques used by MVFIT.

The momentum and vertex correction were both applied before generating the resolution tables and plots in this appendix (but were themselves based on the same tables calculated before the corrections were applied). The directional, vertex, and perpendicular ( $\perp$ ) vertex resolutions all represent the minimal point that includes 68% of the entries. The mean and variance for the momentum and parallel ( $\parallel$ ) vertex resolutions were calculated using Gaussian fits.

In all of the plots in this chapter, the solid lines represent the  $pp \rightarrow K^+ K^+$  Monte Carlo and the dashed lines represent the atmospheric neutrino Monte Carlo. The vertical lines represent the 68% resolution point. In all plots, " $\Delta$  *variable name*" indicates the reconstructed value of the variable minus the true value of the variable.  $\Delta$  *vertex*  $\parallel$  indicates the difference between the reconstructed and true vertex along the direction parallel to the true direction of the particle. Likewise,  $\Delta$  *vertex*  $\perp$  indicates the difference between the reconstructed and true vertex in the plane perpendicular to the true direction of the particle.

## A.1 Charged Kaon Ring Resolutions

The MVFIT reconstructed variable resolutions for rings created by charged kaons are listed in Table A.1, and shown in Fig. A.1. 409 kaon rings from the atmospheric neutrino Monte Carlo and 46,097 kaon rings from the  $pp \rightarrow K^+ K^+$  Monte Carlo were analyzed.

$K^\pm$ rings	Atm. $\nu$	$pp \rightarrow K^+ K^+$
<b>direction</b>		
resolution	4°	4°
<b>momentum</b>		
mean	-12%	0%
variance	11%	6%
<b>vertex</b>		
resolution	160 cm	130 cm
$\perp$ resolution	20 cm	40 cm
$\parallel$ mean	-68 cm	-27 cm
$\parallel$ variance	114 cm	88 cm

**Table A.1:** MVFIT reconstructed resolutions for true charged kaon rings.  $\perp$  indicates the direction perpendicular to the ring direction, and  $\parallel$  indicates the direction parallel to the ring direction.

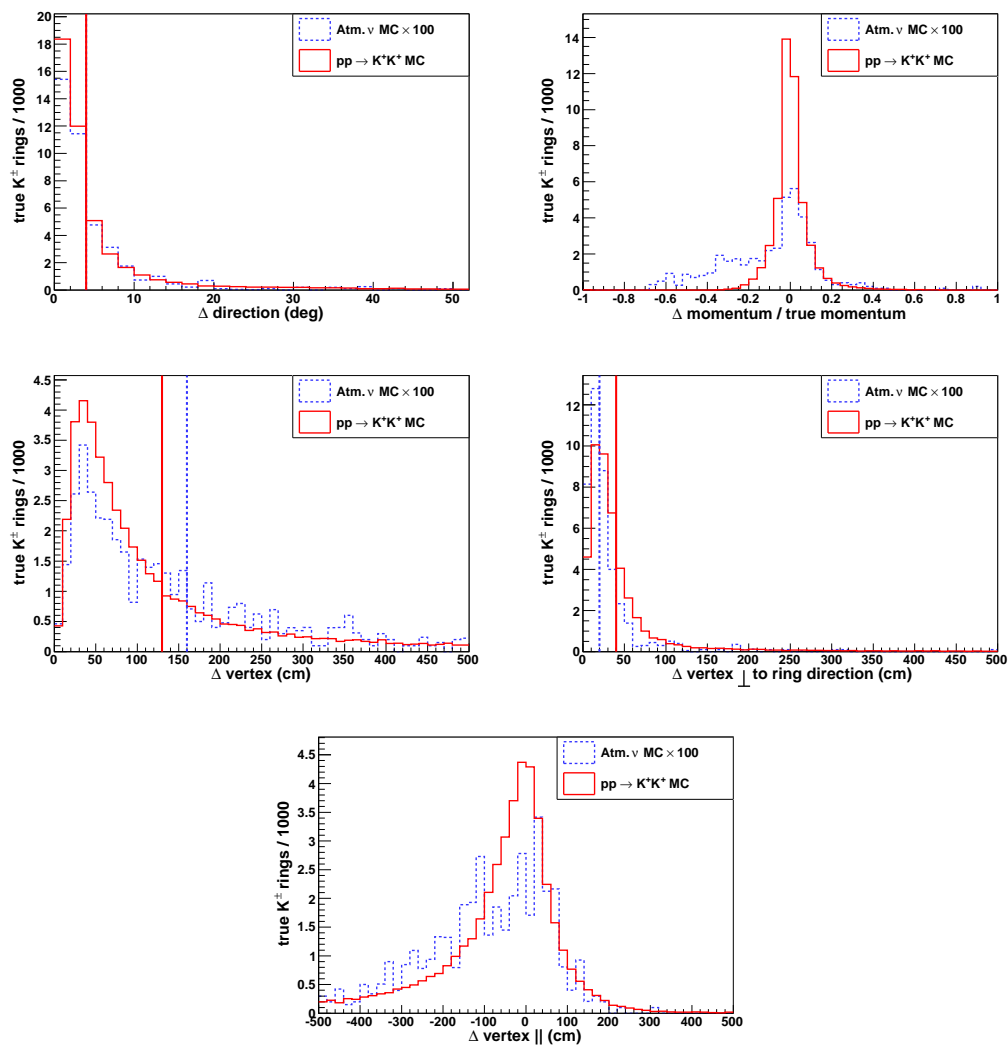


**Figure A.1:** MVFIT reconstructed variable resolutions for charged kaons. In order from left to right, top to bottom: direction, momentum, vertex, vertex perpendicular to ring direction, vertex parallel to ring direction.

## A.2 Muon Ring Resolutions

The MVFIT reconstructed variable resolutions for rings created by muons are listed in Table A.2, and shown in Fig. A.2. 25,357 muon rings from the atmospheric neutrino Monte Carlo and 33,775 muon rings from the  $pp \rightarrow K^+ K^+$  Monte Carlo were analyzed.

$\mu^\pm$ rings	Atm. $\nu$	$pp \rightarrow K^+ K^+$
<b>direction</b>		
resolution	3°	6°
<b>momentum</b>		
mean	+2%	-1%
variance	2%	9%
<b>vertex</b>		
resolution	35 cm	140 cm
$\perp$ resolution	15 cm	65 cm
mean	+4 cm	0 cm
variance	23 cm	45 cm

**Table A.2:** MVFIT reconstructed resolutions for true muon rings.  $\perp$  indicates the direction perpendicular to the ring direction, and  $||$  indicates the direction parallel to the ring direction.

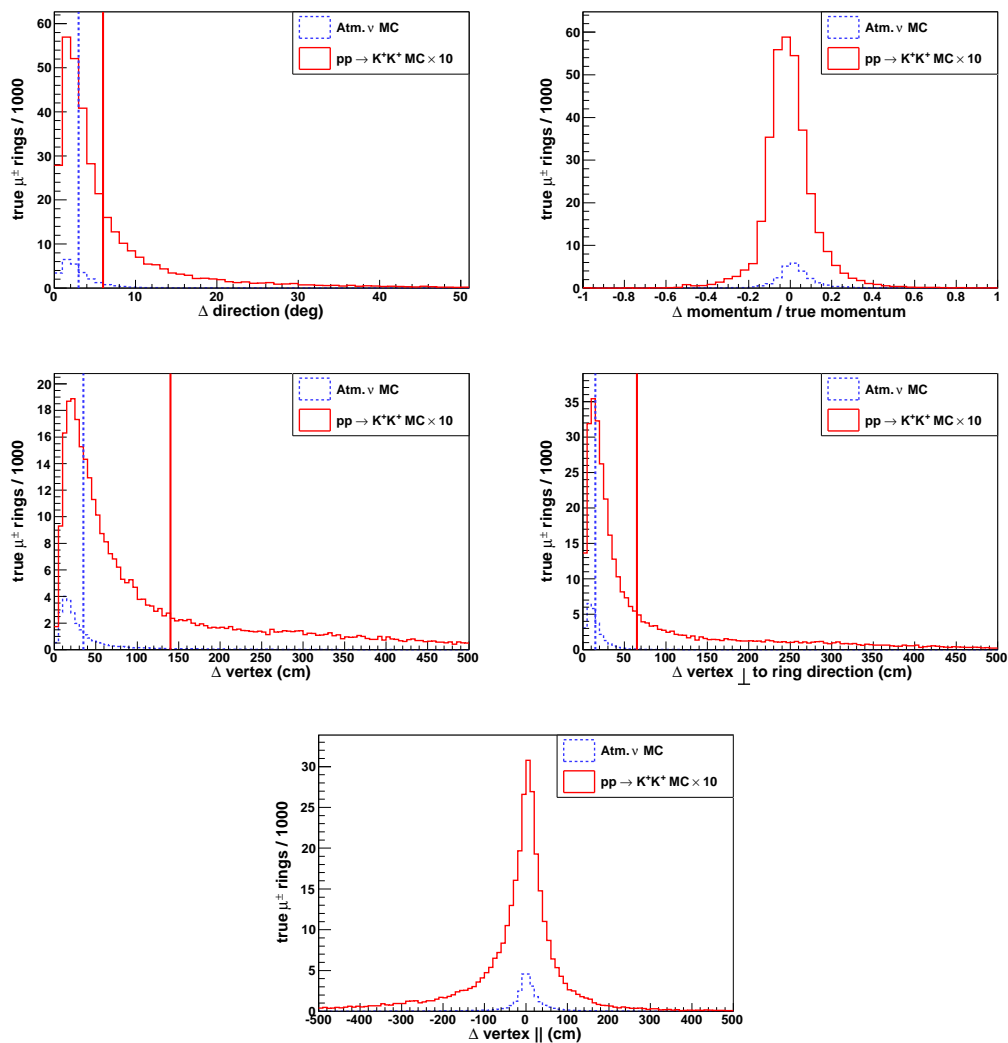


**Figure A.2:** MVFIT reconstructed variable resolutions for muons. In order from left to right, top to bottom: direction, momentum, vertex, vertex perpendicular to ring direction, vertex parallel to ring direction.

### A.3 Gamma Ring Resolutions

The MVFIT reconstructed variable resolutions for rings created by gammas or electrons are listed in Table A.3, and shown in Fig. A.3. 168,935 gamma and electron rings from the atmospheric neutrino Monte Carlo and 56,972 gamma and electron rings from the  $pp \rightarrow K^+ K^+$  Monte Carlo were analyzed.

$\gamma, e^\pm$ rings	Atm. $\nu$	$pp \rightarrow K^+ K^+$
<b>direction</b>		
resolution	6°	8°
<b>momentum</b>		
mean	-5%	+5%
variance	25%	29%
<b>vertex</b>		
resolution	110 cm	140 cm
$\perp$ resolution	20 cm	40 cm
mean	+67 cm	+63 cm
variance	68 cm	79 cm

**Table A.3:** MVFIT reconstructed resolutions for true gamma and electron rings.  $\perp$  indicates the direction perpendicular to the ring direction, and  $||$  indicates the direction parallel to the ring direction.

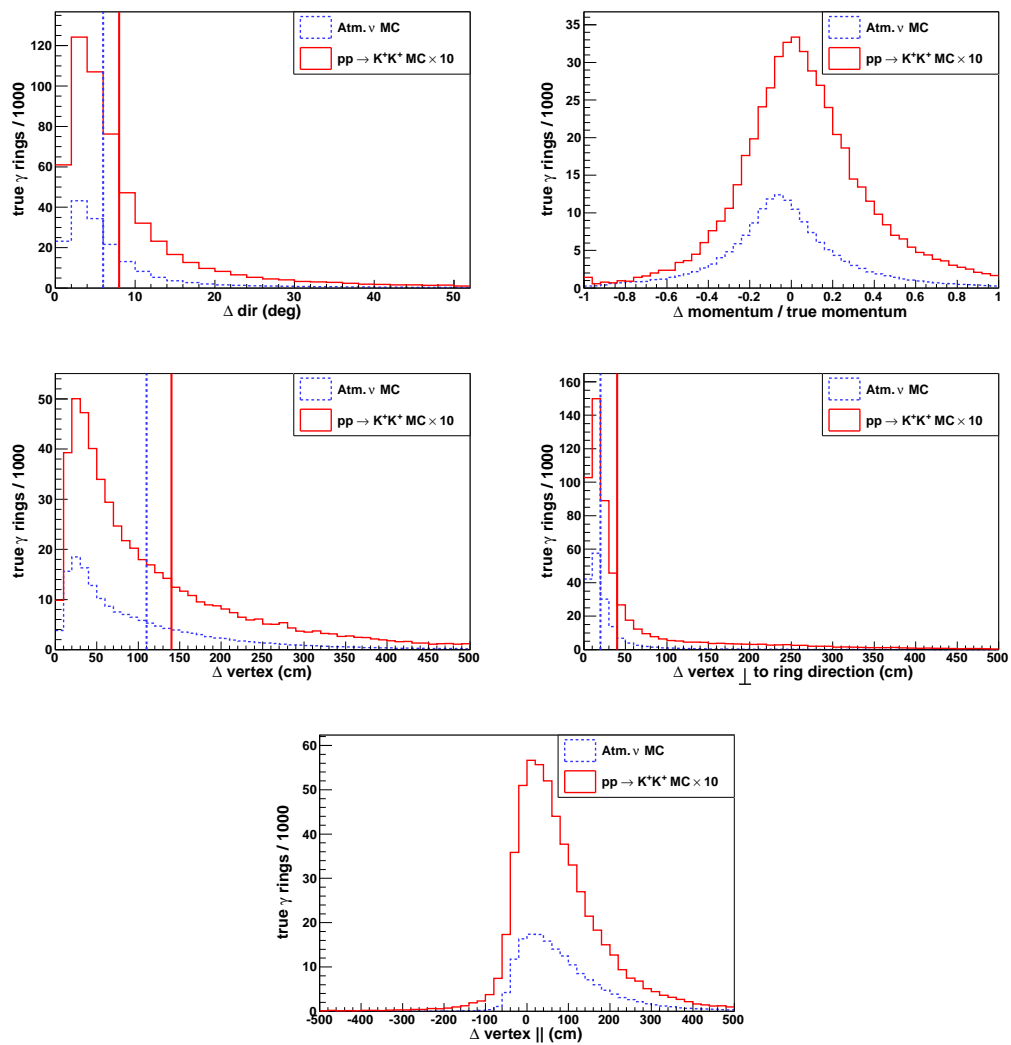


**Figure A.3:** MVFIT reconstructed variable resolutions for gammas and electrons. In order from left to right, top to bottom: direction, momentum, vertex, vertex perpendicular to ring direction, vertex parallel to ring direction.

## Appendix B

# Boosted Decision Tree

The ROOT-based TMVA [74] multivariate analysis software package was used to implement the boosted decision tree in this analysis.

A decision tree is a classifier with a top-down binary tree structure. Starting with the first node in the tree, all variables are scanned and a one-dimensional cut is placed on the variable which allows for the maximal separation of signal and background. The events are then split into two groups, one passing the cut and traveling down the “signal-like” branch to one node, and the other failing the cut and traveling down the “background-like” branch to another node. The same process is then repeated for each of the two new daughter nodes. This pattern is repeated until a certain stopping criterion is reached, at which point a node is no longer split into two branches, but is instead declared either a signal-like or background-like terminal leaf node, depending on the makeup of the events which it contains. The process of creating of a tree is synonymous with training a tree.

Boosting refers to the process of training a classifier using a reweighted, or “boosted,” training event sample that was the output of a previously trained classifier. In the case of a boosted decision tree, the output of tree  $n$  is reweighted based on the per-

formance of that tree. Then, those boosted events are used to create tree  $n + 1$ . Note that the output of tree  $n$  includes all of the original training events; no events are thrown out or go unused in any tree created during the training process.

The forest is the name given to the full collection of decision trees that are created during the training process. The forest itself is simply referred to as the boosted decision tree, and its output is a weighted majority of the decision trees from which it is comprised.

## B.1 Final Output

The calculation for the final boosted decision tree output,  $y_{\text{BDT}}(x)$ , is shown below:

$$y_{\text{BDT}}(x) = \sum_{i \in \text{forest}} \ln(\alpha_i) \cdot h_i(x) \quad (\text{B.1})$$

where  $x$  is the tuple of input variables, and  $h_i(x)$  and  $\alpha_i$  are the output and weight of the individual trees, respectively. The calculation of the weight for a given tree is described in Section B.3.

## B.2 Separation Index

The branch node splitting is a one-dimensional cut on a single variable from the tuple of input variables. The binning for the variables is specified in the boosted decision tree tuning parameters, and the trial locations for the branching cut lie between the bins. All options are considered, and the variable and cut position which maximize the separation index between the current node and those of the hypothetical daughter nodes are chosen. The hypothetical daughter nodes are weighted by their relative fraction of events in this calculation.

The separation index, or Gini index, is defined below, where  $P$  is the purity of the node,  $N$  is the number of training events in the node, and  $W_i$  is the weight of the individual events:

$$P = \frac{\sum_S W_S}{\sum_S W_S + \sum_B W_B} \quad (\text{B.2})$$

$$Gini = \left( \sum_{i=1}^N W_i \right) P \cdot (1 - P) \quad (\text{B.3})$$

The quality of separation,  $Q_{\text{sep}}$ , is maximized at each branching node, and is given by:

$$Q_{\text{sep}} = G_{\text{parent}} - (G_{\text{bkg}} + G_{\text{sig}}) \quad (\text{B.4})$$

where  $G_{\text{parent}}$  is the Gini index of the parent node, and  $G_{\text{bkg}}$  and  $G_{\text{sig}}$  are the Gini indices of the background-like and signal-like daughter nodes, respectively.

### B.3 Adaptive Boost Method

The boosting method that was used in this analysis is the adaptive boost method (“Ada-Boost”). In this method, misclassified events (*i.e.*, signal events which end up in a background leaf, or vice versa) are given a larger event weight in the training of the next tree. All of the misclassified events in a single tree are multiplied by a common boost weight,  $\alpha$ , where  $err$  is the mis-classification rate of the tree.

$$\alpha = \frac{1 - err}{err} \quad (\text{B.5})$$

## B.4 Pruning

Pruning is a process by which statistically insignificant nodes are removed from a tree after it has been grown to maximum size (*i.e.*, all branches have ended in terminal leaf nodes). In this analysis, the expected error pruning method was used, which removes all daughter nodes for which the statistical error estimate of the parent node is smaller than the combined statistical error estimates of the daughter nodes. Thus a branching node may become a leaf node.

The statistical error estimate of each node,  $\epsilon_{\text{node}}$ , is calculated using the binomial error, as shown below:

$$\epsilon_{\text{node}} = F \cdot \sqrt{\frac{P \cdot (1 - P)}{N}} \quad (\text{B.6})$$

where  $P$  is the purity of the node,  $N$  is the number of training events in the node, and  $F$  is the pruning strength factor. The pruning criterion is then given by:

$$\epsilon_{\text{parent}} < \epsilon_{\text{bkg}} + \epsilon_{\text{sig}} \quad (\text{B.7})$$

where  $\epsilon_{\text{parent}}$  is the statistical error of the parent node, and  $\epsilon_{\text{bkg}}$  and  $\epsilon_{\text{rmsig}}$  are the statistical errors of the background-like and signal-like daughter nodes, respectively.

## B.5 Training Distributions

The distributions of each of the input variables used in the training of the boosted decision tree can be seen in Fig. B.1. See Section 9.4.1 for a complete description of each of the input variables.

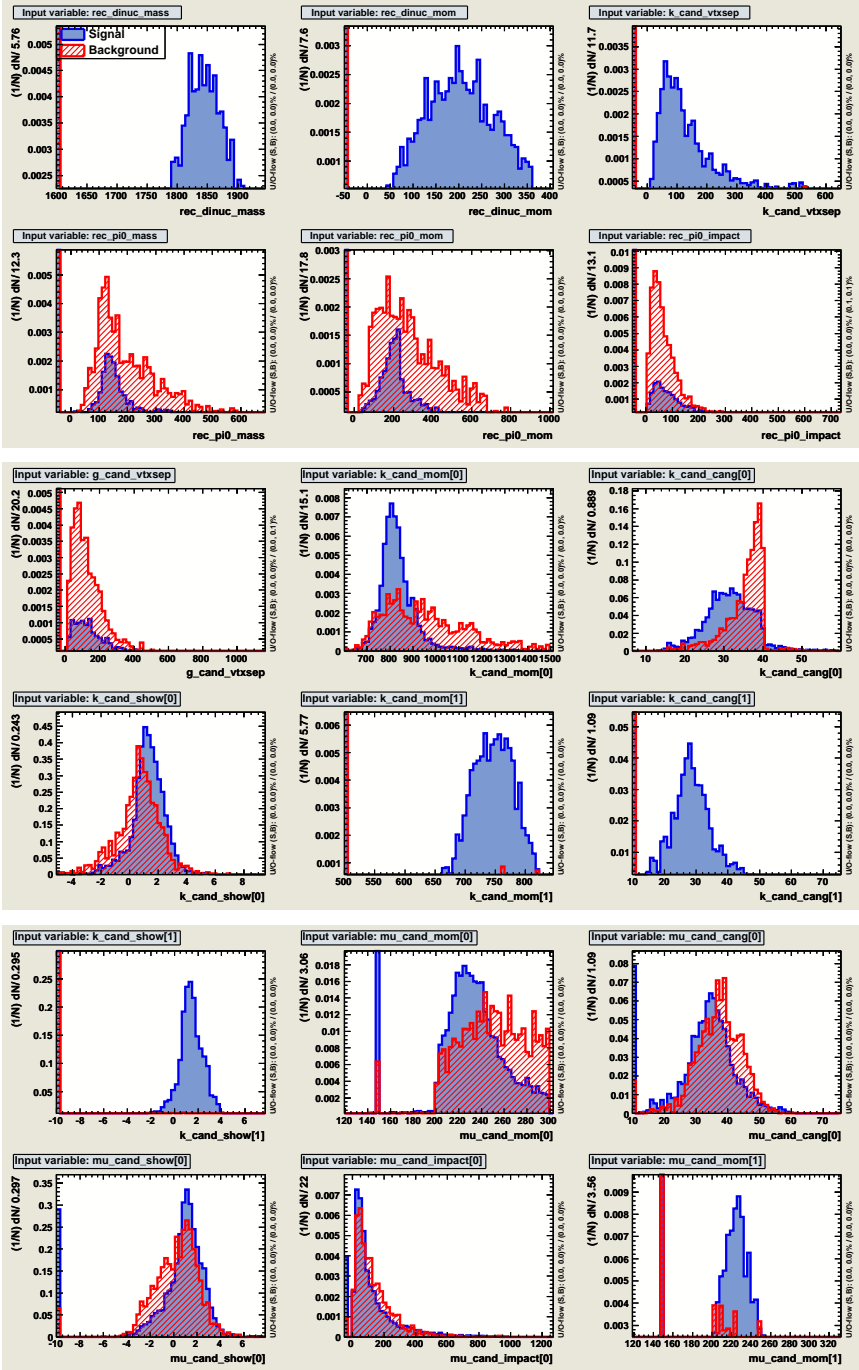


**Figure B.1:** Distributions of the input variables used to train the boosted decision tree. Trivial bins have been truncated to emphasize shape difference in the non-trivial range. Filled blue histograms indicate the  $pp \rightarrow K^+ K^+$  signal Monte Carlo. Hatched red histograms indicate the atmospheric neutrino background Monte Carlo.



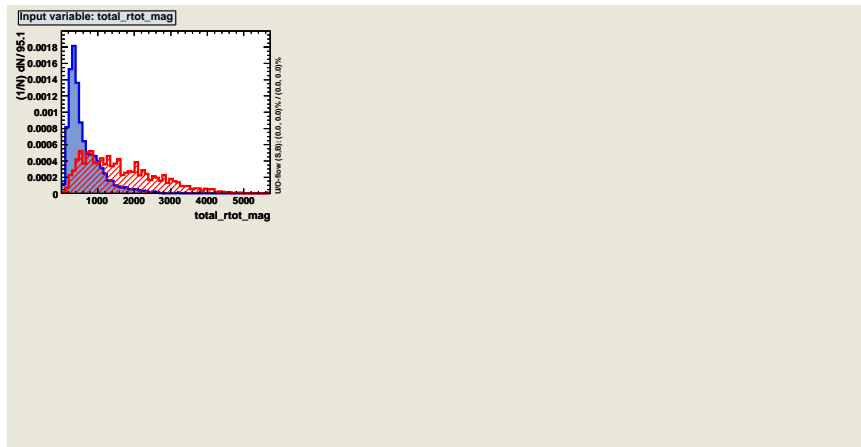


**Figure B.1:** (Continued...) Distributions of the input variables used to train the boosted decision tree. Trivial bins have been truncated to emphasize shape difference in the non-trivial range. Filled blue histograms indicate the  $pp \rightarrow K^+ K^+$  signal Monte Carlo. Hatched red histograms indicate the atmospheric neutrino background Monte Carlo.

## B.6 Variable Ranking

A ranking of the input variables used to train the boosted decision tree can be estimated by counting how often each is used. Each time a variable is used at a branching node, it is weighted by the square of the separation gain achieved by the splitting, as well as the number of events in the node. The variable ranking for this analysis is shown in Table B.1.

The most important variables, **total\_rtot\_mag** and **total\_rtot\_dot\_k**, are measures of the symmetry of the overall light pattern of the event. The dinucleon decay events have a very high degree of symmetry, largely due to the back-to-back kaons. The atmospheric neutrino interactions are less likely to create very symmetric distributions of light due to the initial momentum of the incoming neutrino.

The least important variables, **rec\_pi0\_mom** (the reconstructed  $\pi^0$  momentum) and **k\_cand\_cang[1]** (the reconstructed Cherenkov angle of the second kaon candidate), are both members of collections of variables that describe a pair of clas-

sified kaon candidates or gamma candidates, respectively. Thus, after the other variables in their respective collections have already been exploited, there is little discrimination power left in these two. **k\_cand\_cang[0]** is much more powerful than **k\_cand\_cang[1]** because every event that enters the boosted decision tree is required to have at least one kaon candidate, as dictated by the precuts in Section 9.3, whereas not every event has a second kaon candidate. In fact, very few background events have two kaon candidates.

Rank	Variable Name	Importance $\times 10^2$
1	total_rtot_mag	7.0
2	total_rtot_dot_k	5.4
3	g_cand_impact[0]	5.0
4	rec_pi0_mass	4.7
5	mu_cand_mom[1]	4.7
6	off_vtx_sep	4.6
7	dcy_e_vtxsep	4.6
8	k_cand_mom[0]	4.7
9	k_cand_cang[0]	4.5
10	mu_cand_mom[0]	4.1
11	k_cand_mom[1]	3.9
12	g_cand_cang[0]	3.6
13	mu_cand_cang[0]	3.5
14	g_cand_vtxsep	3.3
15	g_cand_totmom	2.7
16	decay_vtxsep	2.6
17	g_cand_show[1]	2.5
18	rec_dinuc_mass	2.4
19	k_cand_vtxsep	2.4
20	k_cand_show[1]	2.3
21	agood	2.2
22	k_cand_show[0]	2.1
23	g_cand_cang[1]	2.0
24	g_cand_mom[0]	1.8
25	mu_cand_impact[0]	1.7
26	rec_pi0_impact	1.5
27	g_cand_show[0]	1.4
28	mu_cand_show[0]	1.3
29	mu_cand_cang[1]	1.1
30	g_cand_impact[1]	1.1
31	rec_dinuc_mom	1.1
32	mu_cand_impact[1]	0.9
33	mu_cand_show[1]	0.9
34	g_cand_mom[1]	0.8
35	n_dcy_e	0.7
36	rec_pi0_mom	0.6
37	k_cand_cang[1]	0.1

**Table B.1:** Input variables for the boosted decision tree.

## Appendix C

# Limit Calculations

### C.1 Lower Lifetime Limit on Decay Mode

The following expression for the probability of detecting  $n$  signal events is obtained by simple Poisson statistics:

$$\mathbf{P}(n|\Gamma\lambda\epsilon b) = \frac{e^{-(\Gamma\lambda\epsilon+b)} (\Gamma\lambda\epsilon + b)^n}{n!}, \quad (\text{C.1})$$

where  $\Gamma$  is the decay rate,  $\lambda$  is the exposure,  $\epsilon$  is the detection efficiency,  $b$  is the amount of background, and  $\mathbf{P}(A|B)$  is the conditional probability of A, given that proposition B is true.

To be able to take into account the systematic errors in the limit calculation, Bayes' Theorem is used. Applying Bayes' Theorem to the Poisson function gives the following:

$$\mathbf{P}(\Gamma\lambda\epsilon b|n) = \frac{1}{A} \mathbf{P}(n|\Gamma\lambda\epsilon b) \mathbf{P}(\Gamma\lambda\epsilon b), \quad (\text{C.2})$$

where  $A$  is a normalization factor.

As the decay rate, detection efficiency, exposure, and background are all indepen-

dent variables, the above expression can be rewritten to give:

$$\mathbf{P}(\Gamma\lambda\epsilon b|n) = \frac{1}{A}\mathbf{P}(n|\Gamma\lambda\epsilon b)\mathbf{P}(\Gamma)\mathbf{P}(\epsilon)\mathbf{P}(\lambda)\mathbf{P}(b). \quad (\text{C.3})$$

Now the probability density function of  $\Gamma$  can be defined as:

$$\mathbf{P}(\Gamma|n) = \int \int \int \mathbf{P}(\Gamma\lambda\epsilon b|n)d\epsilon d\lambda db, \quad (\text{C.4})$$

which can be re-expressed as:

$$\mathbf{P}(\Gamma|n) = \frac{1}{A} \int \int \int \frac{e^{-(\Gamma\lambda\epsilon+b)} (\Gamma\lambda\epsilon + b)^n}{n!} \mathbf{P}(\Gamma)\mathbf{P}(\epsilon)\mathbf{P}(\lambda)\mathbf{P}(b)d\epsilon d\lambda db. \quad (\text{C.5})$$

The normalization factor  $A$  is given by:

$$A = \int_0^\infty \mathbf{P}(\Gamma|n)d\Gamma. \quad (\text{C.6})$$

The systematic uncertainties on the detection efficiency, exposure, and background can now be incorporated into the prior distributions,  $\mathbf{P}(\lambda)$ ,  $\mathbf{P}(\epsilon)$  and  $\mathbf{P}(b)$ , the shapes of which are assumed to be truncated Gaussian distributions:

$$\mathbf{P}(\lambda) \propto \begin{cases} \exp\left(-\frac{(\lambda-\lambda_0)^2}{2\sigma_\lambda^2}\right) & (\lambda > 0) \\ 0 & (\lambda \leq 0) \end{cases}, \quad (\text{C.7})$$

$$\mathbf{P}(\epsilon) \propto \begin{cases} \exp\left(-\frac{(\epsilon-\epsilon_0)^2}{2\sigma_\epsilon^2}\right) & (\epsilon > 0) \\ 0 & (\epsilon \leq 0) \end{cases}, \quad (\text{C.8})$$

$$\mathbf{P}(b) \propto \begin{cases} \exp\left(-\frac{(b-b_0)^2}{2\sigma_b^2}\right) & (b > 0) \\ 0 & (b \leq 0) \end{cases}. \quad (\text{C.9})$$

where  $\lambda_0$ ,  $\epsilon_0$ , and  $b_0$  are the estimations of the efficiency, exposure, and background, and  $\sigma_\lambda$ ,  $\sigma_\epsilon$ , and  $\sigma_b$  are their respective systematic uncertainties.

For asymmetric systematic errors, the prior distribution is defined as:

$$\mathbf{P}(\alpha) \propto \begin{cases} \exp\left(-\frac{(\alpha-\alpha_0)^2}{2\sigma_{\alpha+}^2}\right) & (\alpha > \alpha_0) \\ \exp\left(-\frac{(\alpha-\alpha_0)^2}{2\sigma_{\alpha-}^2}\right) & (0 < \alpha \leq \alpha_0) \\ 0 & (\alpha \leq 0) \end{cases}, \quad (\text{C.10})$$

where  $\alpha$  is the quantity described by the prior, and  $\sigma_{\alpha+}$  and  $\sigma_{\alpha-}$  are its corresponding positive and negative systematic uncertainties.

Because the expected background in this study is near zero, the statistical error of the background estimation is taken into account by treating the prior as a convolution of a Poisson and a Gaussian distribution:

$$\mathbf{P}(b) = \int_0^\infty \frac{e^{-b_{\text{MC}}} (b_{\text{MC}})^{n_b}}}{n_b!} \exp\left(-\frac{(bC - b_{\text{MC}})^2}{2\sigma_b^2}\right) db_{\text{MC}}, \quad (\text{C.11})$$

where  $n_b$  is the number of background events in the unnormalized Monte Carlo,  $b_{\text{MC}}$  is the number of true background events in the livetime normalized Monte Carlo, and  $C$  is the oversampling factor of the Monte Carlo.

The prior distribution of the decay rate,  $\Gamma$ , is taken to be uniform from 0 to a cutoff value:

$$\mathbf{P}(\Gamma) = \begin{cases} 1 & (0 < \Gamma < \Gamma_{\text{cut}}) \\ 0 & (\Gamma \leq 0 \text{ or } \Gamma \geq \Gamma_{\text{cut}}) \end{cases}, \quad (\text{C.12})$$

where the cutoff value,  $\Gamma_{\text{cut}}$ , is the upper limit of the decay rate for the calculation of the normalization factor  $A$  needed to avoid divergence.  $\Gamma_{\text{cut}}$  is set to  $10^{-31}\text{years}^{-1}$ , which should be sufficiently large for this study.

The confidence level (CL) can be calculated by integrating the probability density function:

$$CL = \int_0^{\Gamma_{\text{limit}}} \mathbf{P}(\Gamma|n) d\Gamma. \quad (\text{C.13})$$

And finally, after setting the confidence level to the desired value and solving the above equation for  $\Gamma_{\text{limit}}$ , one can obtain an expression for the lower lifetime limit:

$$\tau_{\text{limit}} = 1/\Gamma_{\text{limit}}. \quad (\text{C.14})$$

## C.2 Upper Limit on $R$ -Parity Violating Parameter

Fermi's Golden Rule gives the expression for the average rate of dinucleon decay  $\bar{\Gamma}$  as:

$$\bar{\Gamma} = \frac{1}{2\pi^3\rho_N} \int d^3k_1 d^3k_2 \rho(k_1)\rho(k_2)v_{\text{rel}}(1 - \mathbf{v}_1 \cdot \mathbf{v}_2)\sigma_{\text{tot}}(\text{NN} \rightarrow \text{X}), \quad (\text{C.15})$$

where  $\rho_N$  is the average nucleon density,  $k_i$  is the momentum of the  $i$ th nucleon,  $\rho(k_i)$

is the density in momentum space of the  $i$ th nucleon,  $v_{\text{rel}}$  is the relative velocity of the nucleons,  $\mathbf{v}_i$  is the velocity vector of the  $i$ th nucleon (taken to be small), and  $\sigma_{\text{tot}}$  is the total cross-section for the decay. The cross-section can be approximated by:

$$\sigma_{\text{tot}}(\text{NN} \rightarrow \text{X}) \sim \rho_{\text{N}} \frac{128\pi\alpha_s^2 |\lambda''_{uds}|^4 R^{10}}{v_{\text{rel}} M_{\text{N}}^2}, \quad (\text{C.16})$$

where  $\alpha_s$  is the strong coupling,  $\lambda''_{uds}$  is the  $R$ -Parity prohibited SUSY coupling constant,  $M_{\text{N}}$  is the nucleon mass, and  $R$  is the ratio between the hadronic and SUSY scales, given by:

$$R = \frac{\tilde{\Lambda}}{(M_{\tilde{g}} M_{\tilde{q}}^4)^{1/5}}, \quad (\text{C.17})$$

where  $\tilde{\Lambda}$  is the QCD scale,  $M_{\tilde{g}}$  is the gluino mass,  $M_{\tilde{q}}$  is the squark mass.

The partial lifetime  $\tau$  is simply the inverse of the decay rate:

$$\tau = \frac{1}{\tilde{\Gamma}} \sim \frac{M_{\text{N}}^2}{\rho_{\text{N}} 128\pi\alpha_s^2 |\lambda''_{uds}|^4} R^{-10}. \quad (\text{C.18})$$

Here it clearly shown that the lifetime scales with  $|\lambda''_{uds}|^{-4}$ .

Taking  $\rho_{\text{N}} = 0.25 \text{ fm}^{-3}$ ,  $\alpha_s \sim 0.12$ , and  $M_{\text{N}} = 0.94 \text{ GeV}/c^2$ , and assuming that  $\tau$  represents an upper limit on the decay process lifetime gives the upper limit on  $\lambda''_{uds}$  as:

$$|\lambda''_{uds}| < \left( \frac{1.65 \times 10^{-30}}{\tau [\text{years}]} R^{-10} \right)^{1/4}. \quad (\text{C.19})$$

If  $R$  is taken to be  $\sim 1.1 \times 10^{-3}$ , as per Goity and Sher [22], then the upper limit on  $\lambda''_{uds}$  as a function of the lower lifetime limit on dinucleon decay into kaons is given by:

$$|\lambda''_{uds}| < \left( \frac{0.64}{\tau [\text{years}]} \right)^{1/4}. \quad (\text{C.20})$$

# Bibliography

- [1] S. Fukuda, *et al.* Nuclear Inst. and Methods in Physics Research, A **501**, 2-3 418 (2003)
- [2] K. Hirata, *et al.* Physics Letters B **220**, 1 (1989)
- [3] C. McGrew, *et al.* Physical Review D **59** 052004 (1999)
- [4] Nishino, *et al.* Physical Review Letters **102**, 141801 (2009)
- [5] K. Kobayashi, *et al.* Physical Review D **72** 052007 (2005)
- [6] M. Shiozawa, *et al.* Physical Review Letters **81**, 16 (1998)
- [7] Y. Hayato, *et al.* Physical Review Letters **83** 1529 (1999)
- [8] H. Georgi, S. L. Glashow. Physical Review Letters **32** 438 (1974)
- [9] P. Langacker. Physics Reports **72C** (1981)
- [10] P. Langacker. Arxiv preprint hep-ph **hep-ph/9411247** (1994)
- [11] Super-Kamiokande. <http://www-sk.icrr.u-tokyo.ac.jp/whatsnew/new-20091125-e.html> (2010)
- [12] C. Amsler, *et al.* Physics Letters B **667**, 1 (2008)

- [13] R. Bernabei, *et al.* Physics Letters B **493**, 12 (2000)
- [14] H. Back, *et al.* Physics Letters B **563**, 23 (2003)
- [15] C. Berger, *et al.* Physics Letters B **269** 227 (1991)
- [16] T. Lee, C. Yang. Physical Review **104** 254 (1956)
- [17] C. Wu, *et al.* Physical Review **105** 1413 (1957)
- [18] A. Sakharov. Physics-Uspekhi **34**, 5 392 (1991)
- [19] L. Carpenter, D. Kaplan, E. Rhee. Arxiv preprint hep-ph/0607204 (2006)
- [20] A. Barbieri, A. Masiero. Nuclear Physics B **267** 679 (1986)
- [21] S. Dimopoulos, L. Hall. Physics Letters B **196**, 2 (1987)
- [22] J. Goity, M. Sher. Physics Letters B **346**, 1-2 69 (1995)
- [23] K. Abe, *et al.* ArXiv preprint hep-ex/0607059v2 (2006)
- [24] G. 't Hooft. Physical Review Letters **37**, 8 (1976)
- [25] S. Martin. Arxiv preprint hep-ph/9709356 (1997)
- [26] J. Rosiek. Physical Review D **41**, 11 3464 (1990)
- [27] M. Chemtob. Progress in Particle and Nuclear Physics **54**, 1 71 (2005)
- [28] R. Barbier, *et al.* Arxiv preprint hep-ph/0406039 (2004)
- [29] H. Nishino. Ph.D. Thesis, University of Tokyo (2009)
- [30] M. Honda, *et al.* Physical Review D **70**, 4 (2004)
- [31] W. G. Webber, S. Stephens. Proc. 20th ICRC (Moscow, 1987) (1987)

- [32] E. Seo, J. Ormes, R. Streitmatter. *The Astrophysical Journal* **378** 7365 (1991)
- [33] P. Papini, C. Grimani. *International Cosmic Ray Conference* (1993)
- [34] M. Boezio, *et al.* *Physical Review Letters* **82** 4757 (1999)
- [35] M. Hof, *et al.* *Nuclear Instruments and Methods in Physics Research A* **454**, 1 180 (2000)
- [36] T. Sanuki, *et al.* Arxiv preprint astro-ph/0002481 (2000)
- [37] A. Alcaraz, *et al.* *Physics Letters B* **490** 27 (2000)
- [38] M. Ryan, J. Ormes, V. Balasubrahmanyam. *Physical Review Letters* **28** 985 (1972)
- [39] K. Asakimori, *et al.* *The Astrophysical Journal* **28** 985 (1998)
- [40] I. Ivanenko, V. Shestoporov. *International Cosmic Ray Conference* **2** (1993)
- [41] Y. Kawamura, *et al.* *Physical Review D* **40** 729 (1989)
- [42] A. V. Apanasenko, *et al.* *Astroparticle Physics Journal* **16** 13 (2001)
- [43] K. Hänssgen, J. Ranft. *Computational Physics Communications* **39**, 11 53 (1986)
- [44] S. Roesler, R. Engel, J. Ranft. *Physical Review D* **57** 2889 (1998)
- [45] G. D. Barr, *et al.* *Physical Review D* **D70** 023006 (2004)
- [46] G. Battistoni, *et al.* Arxiv preprint hep-ph/0305208v1 (2003)
- [47] Y. Hayato. *Nuclear Physics Proceedings Supplements* **112** 171 (2002)
- [48] C. H. L. Smith. *Physics Reports* **3** 261 (1972)

- [49] S. Barish, *et al.* Physical Review D **16** 3103 (1977)
- [50] S. Bonetti, *et al.* Il Nuovo Cimento A (1977)
- [51] M. Pohl, *et al.* Il Nuovo Cimento A **26**, 11 (1979)
- [52] N. Armenise, *et al.* Nuclear Physics B **152** 365 (1979)
- [53] A. Vovenko, A. Volkov, V. Zhigunov. Soviet Journal of Nuclear Physics (1979)
- [54] S. Belikov, A. Bygorsky, L. Klimenko. Zeitschrift für Physik A (1985)
- [55] J. Brunner, H. Grabosch, H. Kaufmann. Zeitschrift für Physik C (1990)
- [56] D. Rein, L. M. Sehgal. Annual Physics **133** 79 (1981)
- [57] Y. Ashie, *et al.* Physical Review D **71**, 11 112005 (2005)
- [58] M. Nakahata, *et al.* Journal of the Physical Society of Japan **55** 3786 (1986)
- [59] T. Sjostrand. Computer Physics Communications **82** 74 (1994)
- [60] M. Glück, E. Reya, A. Vogt. The European Physical Journal C-Particles **5** 461 (1998)
- [61] A. Bodek, U. K. Yang. Arxiv preprint hep-ex/0301036 (2003)
- [62] M. Derrick, *et al.* Physical Review **D17** 1 (1978)
- [63] S. Barlag, *et al.* Zeitschrift für Physik **C11** 283 (1982)
- [64] P. Musset, J. P. Vialle. Physics Reports **39** 1 (1978)
- [65] J. E. Kim, *et al.* Reviews of Modern Physics **53** 211 (1981)
- [66] G. Rowe, M. Salomon, R. H. Landau. Physical Review **C18** 584 (1978)

- [67] M. Goossens, C. Geneva. cdsweb.cern.ch (1993)
- [68] T. A. Gabriel, J. E. Brau, B. L. Bishop. IEEE Transactions on Nuclear Science **36** 14 (1989)
- [69] C. Zeitnitz, T. A. Gabriel. Nuclear Instruments and Methods in Physics Research **A349** 106 (1994)
- [70] . H.-E. R. A. Group, E. Bracci. cdsweb.cern.ch (1972)
- [71] K. Nakamura, S. Hiramatsu, T. Kamae. Nuclear Physics A **268**, 3 381 (1976)
- [72] H. Ejiri. Physical Review C **48**, 3 1442 (1993)
- [73] L. Salcedo, *et al.* Nuclear Physics A **484**, 3-4 557 (1988)
- [74] A. Hocker, *et al.* Arxiv preprint physics/0703039 (2007)
- [75] V. Abazov, *et al.* Physical review letters **98**, 18 181802 (2007)
- [76] H. Yang, B. Roe, J. Zhu. Nuclear Instruments and Methods in Physics Research A **555** 370 (2005)
- [77] H. Yang, B. Roe, J. Zhu. Nuclear Instruments and Methods in Physics Research A **574** 342 (2007)

# Curriculum Vitae

## Michael D. Litos

590 Commonwealth Avenue  
Department of Physics, Boston University  
Boston, MA 02215, U.S.A.

**Mobile:** (617)224-7377

**Office:** (617)353-6040

**E-mail:** mlitos@bu.edu

## EDUCATION

- Boston University, Boston, Massachusetts
  - **PhD** in Experimental Particle Physics, expected in May 2010
- Michigan State University, East Lansing, Michigan
  - **Bachelor of Science** in Physics, June 2003
  - **Additional Major** in East Asian Languages & Culture (Japanese), June 2003

## RESEARCH EXPERIENCE

- Super-Kamiokande / T2K
  - Hardware:
    - \* Design, construction, installation and interfacing software for slow control and monitor system for front end electronics
    - \* Installation of PMTs, wavelength shifter plates, reflective Tyvek wall coverings
    - \* Testing of ethernet communication daughter cards for front end electronics upgrade
    - \* Testing of prototype Hamamatsu PMTs in a water Cherenkov detector
  - Simulation:
    - \* Creation of detector simulation in Geant4, including ROOT-based event display
    - \* Detector design optimization through MC modeling and testing
    - \* PMT configuration optimization through MC modeling and testing
    - \* Creation of custom MC input vector generator for dinucleon decay
    - \* Update and maintenance of MC generator functionality validation tool
  - Analysis:

- \* First ever search for dinucleon decay into kaons
- \* First ever multiple vertex fitting algorithm for a water Cherenkov detector
- \* First Super-K analysis using a Boosted Decision Tree
- \* First Super-K analysis incorporating event topology for PID
- \* Upgrade of Cherenkov ring fitting software to fit rings produced by charged kaons

## TEACHING EXPERIENCE

- Boston University
  - Discussion session teaching assistant for college physics, Summer 2005
- Michigan State University
  - Help room teaching assistant for college physics, academic year 2002-2003

## PRESENTATIONS

- **A Search for Dinucleon Decay into Charged Kaons**  
 Michael Litos  
*APS April Meeting, Parallel Talk*  
 St. Louis, MO, April 2008
- **A Search for Dinucleon Decay into Kaons Using a Large Water Cherenkov Detector**  
 Michael Litos  
*Boston University, Departmental Seminar*  
 Boston University, Boston, MA, November 2009
- **Search For Dinucleon Decay Into Kaon Modes Using Multivariate Techniques**  
 Michael Litos  
*APS April Meeting, Parallel Talk*  
 Washington D.C., February 2010
- **Looking for Double Proton Decay at Super-Kamiokande**  
 Michael Litos  
*Fermilab, Special Seminar*  
 Fermi National Accelerator Laboratory, Batavia, IL, March 2010
- **Looking for Double Proton Decay at Super-Kamiokande**  
 Michael Litos  
*SLAC, Special Seminar*  
 SLAC National Accelerator Laboratory, Menlo Park, CA, March 2010

- **Looking for Double Proton Decay at Super-Kamiokande**

Michael Litos

*LBNL, Special Seminar*

Lawrence Berkeley National Laboratory, Berkeley, CA, March 2010

## SELECTED PUBLICATIONS

- **Search for Dinucleon Decay into Kaons via  $^{16}O(pp) \rightarrow ^{14}CK^+K^+$  in a Large Water Cherenkov Detector**  
M. Litos *et al.* [Super-Kamiokande Collaboration]  
*In progress*
- **A Proposal for a Detector 2 km Away From the T2K Neutrino Source**  
E. Kearns *et al.* [T2K Collaboration]  
Proposed to the T2K Collaboration (2005)

## OTHER PUBLICATIONS

- **Search for Proton Decay via  $p \rightarrow e^+\pi^0$  and  $p \rightarrow \mu^+\pi^0$  in a Large Water Cherenkov Detector**  
H. Nishino *et al.* [Super-Kamiokande Collaboration]  
Phys. Rev. Lett. **102**:141801 (2009)
- **Kinematic reconstruction of atmospheric neutrino events in a large water Cherenkov detector with proton identification**  
M. Fechner *et al.* [Super-Kamiokande Collaboration]  
Phys. Rev. D **79**:112010 (2009)
- **First Study of Neutron Tagging with a Water Cherenkov Detector**  
H. Watanabe *et al.* [Super-Kamiokande Collaboration]  
arXiv [hep-ex] **0811**:0735 (2008)
- **Solar neutrino measurements in Super-Kamiokande-II**  
P. Cravens *et al.* [Super-Kamiokande Collaboration]  
arXiv [hep-ex] **0803**:4312 (2008)
- **Search for Matter-Dependent Atmospheric Neutrino Oscillations in Super-Kamiokande**  
K. Abe *et al.* [Super-Kamiokande Collaboration]  
Phys. Rev. D **77**:052001 (2008)
- **Search for Supernova Neutrino Bursts at Super-Kamiokande**  
M. Ikeda *et al.* [Super-Kamiokande Collaboration]  
Astrophys. J. **669**:519-524 (2007)

- **Search for neutral Q-balls in Super-Kamiokande II**  
Y. Takenaga *et al.* [Super-Kamiokande Collaboration]  
Phys. Rev. Lett. B. **647**:18-22 (2006)
- **A Measurement of atmospheric neutrino flux consistent with tau neutrino appearance**  
K. Abe *et al.* [Super-Kamiokande Collaboration]  
Phys. Rev. Lett. **97**:171801 (2006)
- **High energy neutrino astronomy using upward-going muons in Super-Kamiokande-I**  
K. Abe *et al.* [Super-Kamiokande Collaboration]  
Astrophys. J. **652**:198 (2006)
- **Search for Diffuse Astrophysical Neutrino Flux Using Ultrahigh Energy Upward-Going Muons in Super-Kamiokande I**  
Molly E. C. Swanson *et al.* [Super-Kamiokande Collaboration]  
Astrophys. J. **652**:206-215 (2006)

## REFERENCES

- Prof. Edward Kearns  
Boston University  
Department of Physics  
590 Commonwealth Avenue  
Boston, MA 02215  
Office Phone: (617)353-3425  
E-mail: kearns@bu.edu
- Prof. Christopher Walter  
Duke University  
Department of Physics  
Physics Bldg., Science Dr.  
Box 90305, Duke University  
Durham, NC 27708  
Office Phone: (919)660-2535  
E-mail: chris.walter@duke.edu
- Prof. Henry Sobel  
University of California, Irvine  
Department of Physics & Astronomy  
4129 Frederick Reines Hall  
Irvine, CA 92697-4575  
Office Phone: (949)824-6431  
E-mail: hsobel@uci.edu

- Prof. Takaaki Kajita  
Institute for Cosmic Ray Research  
University of Tokyo  
5-1-5 Kashiwa-no-Ha, Kashiwa City  
Chiba, 277-8582, Japan  
Office Phone: (81)471-36-3102  
E-mail: kajita@icrr.u-tokyo.ac.jp